The tracking detector of the MEG II experiment.

Gianluigi Chiarello

July, 2017

UNIVERSITÀ
DEL SALENTO

University of Salento

Department of Matematica e Fisica "E. De Giorgi"
Dottorato di ricerca in Fisica e Nanoscienze XXIX° Ciclo

Phd Thesis

The tracking detector of the MEG II experiment.

Phd Student: Gianluigi Chiarello

Supervisors Marco Panareo
University of Salento
Franco Grancagnolo
INFN Lecce

1. Reviewer Alessandro Baldini
Sezione di Pisa
Istituto Nazionale di Fisica Nucleare

2. Reviewer Giovanni Maria Piacentino
Department of Physics
University of Molise

July, 2017

Gianluigi Chiarello
The tracking detector of the MEG II experiment.
Phd Thesis, July, 2017
Supervisors: Marco Panareo and Franco Grancagnolo
Reviewers: Alessandro Baldini and Giovanni Maria Piacentino

University of Salento

Dottorato di ricerca in Fisica e Nanoscienze XXIX° Ciclo
Department of Matematica e Fisica "E. De Giorgi"
Via Arnesano,sn
73100 and Lecce

I dedicate this work to my family who offered unconditional support. Thanks

"The future belongs to those who believe in
the beauty of their dreams."
Eleanor Roosevelt
"We never fail when we try to do our duty, we always fail when we neglect to do it."
Robert Baden-Powell

Abstract

The MEG experiment, designed to search for $\mu^+ \rightarrow e^+\gamma$ decay, is located at the Paul Scherrer Institute (PSI) in Switzerland. It started the physics data taking in 2008 and an upgraded MEG detector was approved in year 2013.

The analysis of the 2009-2013 data set, which corresponds to 7.5×10^{14} muons stopped in the target, provided an upper limit on the BR of 4.2×10^{-13}@90%CL.

The MEG detector is a dedicated apparatus for a two body back to back decay. It consists in a detector for the photon and a detector for the positron. The photon detector consists in a liquid xenon calorimeter, the positron detector consists in a drift chamber system immersed in an intense magnetic field for positron track detection and in a timing counter for the positron impact time measurement.

The upgrade takes over the basic concept of MEG experiment, while almost all major detectors are upgraded. The sensitivity improvement will be achieved by a 10 times larger data collection, and detector resolutions improved by a factor of two.

The MEG II positron tracker will be replaced by a new tracker consisting of a unique volume low-mass Cylindrical Drift CHamber (CDCH) with a high granularity and a stereo wires configuration.

This thesis describes the MEG II tracker, focusing the attention on the design of the CDCH on its construction using a technique without feed-through and with a wiring robot. The robot has been completely designed and manufactured in Lecce.

This work is structured in six chapters. An introduction about the charged lepton flavor violation searches is presented in the first chapter, focused in particular on the muon sector. In the second chapter, the phenomenological treatment of the decay $\mu^+ \rightarrow e^+\gamma$ is presented. The MEG detector and its upgrade are presented in the third chapter.

In the last three chapters, the CDCH is described. Particularly, in the fourth chapter, the choices on the geometry, mechanics, gas and materials of the CDCH are presented. The semi-automatic system (wiring robot) used for the realization of multi-wire planes is explained in the fifth chapter. Finally, in the sixth chapter, the assembly of the CDCH is described.

Publications

Articles written using content in the thesis:

- “A new cylindrical drift chamber for the MEG II experiment”. In: Nucl. Instrum. Meth. A 824 (2016).
- “The full stereo drift chamber for the MEG II experiment”. In: JINST 12 C03062 (2017).
- “A new construction technique of high granularity and high transparency Drift Chambers for modern High Energy Physics experiments”. In: Nucl. Instrum. Meth. A 824 (2016).
- "A new assembly technique of full stereo Drift Chamber for high energy physics experiments". In:Advances in Sensors and Interfaces (IWASI).
- “Search for the Lepton Flavour Violating Decay$\mu^+ \rightarrow e^+\gamma$ with the Full Dataset of the MEG Experiment”. In: The European Physical Journal C 76.434 (2016).
- “Muon polarization in the MEG experiment:predictions and measurements”. In: The European Physical Journal C 76.3 (2016).
- “A high performance front end for MEG II tracker”. In: Advances in Sensors and Interfaces (IWASI).
- “A high performance Front End Electronics for drift chamber readout in MEG experiment upgrade”. In: Nucl. Instrum. Meth. A 824 (2016).
- " Single-hit resolution measurement with MEG II drift chamber prototypes". In: JINST 11 C03062 (2016).

- "The CluTim algorithm: an improvement on the impact parameter estimates". In: JINST 12 P07011 (2017).

Contents

List of Figures

List of Tables

Abbreviations

SM	Standard Model
BSM	Beyond the Standard Model
cLFV	charged Lepton Flavour Violation
QCD	charged Lepton Flavour Violation
DM	Dark Matter
NP	New Physic
GUT	Grand Unified Theory
SUSY	Supersymmetric Theory
MSSM	Minimal Supersymmetric Standard Mode
B.R.	Branching Ratio
GIM	Glashow Iliopoulos Maiani
DIO	Decay In Orbit
RMD	Radiative Muon Decay
AIF	Annihilation In Flight
SES	Single Event Sensitivity
LXe	Liquid Xenon
HIPA	High Intensity Proton Accelerators
BTS	Beam Transport Solenoid;
COBRA	COnstant Bending RAdius;
DCH	Drift Chamber;
TC	Timing counter;
VUV	Vacuum ultraviolet;
APD	avalanche photo-diodes;
PCB	Printed Circuit Board;
DRS	Domino Ring Sampler;

DAQ	Data AcQuisition system;
MIDAS	Maximum Integrated Data Acquisition System;
MPPC	Multi-Pixel Photon Counters ;
SiPM	Silicon PhotoMultipliers;
CDCH	Cylindrical Drift Chamber;
RDC	Radiative Decay Counter;
US	Upstream;
DS	Downstream;
WDB	Wavw Dream Board;
SNR	Signal-to-Noise Ratio;
CDCH	Cylindrical Drift CHamber;
FE	Front-end Electronics;
DB	Data Base;
SEM	Scanning Electronic Microscope;
MCS	Multiple Columb Scattering;

Part I

Theory and Phenomenology

1

Lepton Flavor Violation

The Standard Model (SM) is the fundamental theory which describes the interactions among the particles. It has been confirmed by many experimental measurements, although it does not explain some phenomena such as the reason why three generations of quarks and leptons exist, and how flavors are mixed together or because the gravitation is not taken into account. In order to explain these phenomena and others, some theories, called theories beyond the Standard Model (BSM), have been developed. Nowadays some experiments have been searching for hints of new theories. This chapter discusses the theory of the SM and some BSM theories. After wards, the bases of the SM and some scenarios of Flavor Violation in charged Leptons (cLFV) sector are described and finally some cLFV experiments are introduced.

1.1 The standard model

The Standard Model [53, 85] of fundamental particles and their interactions is one of the most successful theories in physics. It provides an astonishingly accurate description of phenomena in a wide range of scales. It is a theory based on the gauge symmetry group SU(3)$_C$× SU(2)$_L$×U(1)$_Y$, which describes the strong, weak and electromagnetic interactions. This symmetry is spontaneously broken at low energy (∼100 GeV), reducing to SU(3)$_C$× U(1)$_{em}$. The SU(3)$_C$ corresponds to the symmetry group of Quantum Chromo Dynamics (QCD), the gauge field theory which describes the strong interactions of colored quarks and gluons. The unified electromagnetic and weak interactions are incorporated in the SM by interpreting SU(2)$_L$× U(1)$_Y$ as a group of gauge transformations under which the Lagrangian is invariant [25]. The SM is formed from 6 quarks (*u, d, c, s, t, b*) and another 6 leptons (*e*, $\nu_e, \mu, \nu_\mu, \tau, \nu_\tau$), see Table 1.1. Both leptons and quarks are fermions, having spin 1/2. Particles are subject to three types of interactions: the electromagnetic and the weak interaction, which affects all matter particles, and the strong interaction which only affects the quarks. Interactions take place among particles that carry a certain charge, through the exchange of particles called gauge bosons. The charges associated to the electromagnetic, weak and strong interactions are respectively the electric charge, the weak isospin charge and the color charge.

The gauge sector is formed of: 8 bosons (gluons) generators for SU(3)$_C$, 3 bosons (W$_i$,i=1,2,3) generators for SU(2)$_L$, 1 abelian boson (B) generator for $U(1)_Y$ and Higgs boson, the bosons W$_i$ and B are not the physical boson that mediate the interactions but they are the intermediate bosons [53, 85]. The gluons are massless, electrically neutral and carry color quantum number. The weak bosons W$^\pm$ (they are a linear combination of W$_1$ and W$_2$) and Z are massive particles and the photon γ is massless, chargeless (Z and γ are obtained as a linear combination of W$_3$ and B) and finally the Higgs boson, see Table 1.2. Its mass was recently measured by the experiments CMS [37] and ATLAS [2].

Table 1.1: The particles of the Standard Model.

Fermions(spin -1\2)					
Leptons			Quarks		
Flavor	Charge	Mass (MeV)	Flavor	Charge	Mass (MeV)
ν_e	0	$< 3 \times 10^{-6}$	up	$+2/3$	$1.5 - 4.5$
e	-1	0.511	down	$-1/3$	$5 - 8.5$
ν_μ	0	< 0.19	charm	$+2/3$	$1000 - 1400$
μ	-1	106	strange	$-1/3$	$80 - 155$
ν_τ	0	< 18.2	top	$+2/3$	174300 ± 5100
τ	-1	1777	bottom	$-1/3$	$4000 - 4500$

Table 1.2: Bosons in the SM.

Force	Bosons		Mass [GeV/c^2]
electromagnetic	photon	γ	0
charged weak	W boson	$W^\pm$	80.425 ± 0.038
neutral weak	Z boson	Z^0	91.1876 ± 0.0021
strong	gluon	g	0

1.2 Beyond the Standard Model

Despite its success in describing the particle phenomenology, the SM is unsatisfactory since it is founded on many assumptions and leaves a certain number of puzzling questions still unsolved [86]. For this reason it is assumed that SM is not a definitive theory but an approximation at low energy (that is, the energy currently accessible for particle physics experiments) of a more fundamental theory. Some problems the SM still leaves without an answer:

- *Gauge coupling unification.* The existence of three gauge groups for the SM means having three different coupling constants.

- *Fermion related issues.* The commonly agreed choice of fermion representation under a certain group (such as organizing left fermions into doublets) is due only to fit experimental observations. Moreover, it is not clear why there exist exactly three quark families and if there could be more of them.

- *Introduction of the Higgs boson.* There is no symmetry constraint that justifies an insertion of the Higgs boson into the SM: its existence was postulated ad hoc and the same was for its vacuum expectation value.

- *Unification with gravity.* The force of gravity is not described by the SM, because general relativity was non conceived to be a renormalizable theory.

- *Dark Matter.* The SM can not explain the Dark Matter (DM) of non-baryonic nature and the barion (matter-antimatter) asymmetry in the universe;

- *Cosmology.* The SM does not give an answer to some cosmology observations as inflation.

These facts lead to the conclusion that SM is valid only at low energy. It is indeed clear that the SM cannot describe physics above the so called Planck scale. This hypothesis leads us to supersymmetry and Grand Unification. Various models of New Physics (NP) beyond the SM have been proposed in the last years in order to explain

Table 1.3: MSSM Particle.

SM particles		particles	
Particle	Spin	Particle	Spin
quark (q)	$\frac{1}{2}$	squark ($\tilde{q}$)	0
lepton (l)	$\frac{1}{2}$	slepton ($\tilde{l}$)	0
gluon (G)	1	gluino ($\tilde{G}$)	$\frac{1}{2}$
$W^{\pm}$, Z^0, γ	1	chargino ($\tilde{\chi}_i^{\pm} i = 1, 2$)	$\frac{1}{2}$
Higgs boson ($h,\ H,\ A,\ H^{\pm}$)	0	neutralino ($\tilde{\chi}_i^0 i = 1, 2, 3, 4$)	$\frac{1}{2}$

the problems listed above. Among them, the most important are those involving the so called Supersymmetric Theory (SUSY) and the Grand Unified Theory (GUT).

1.2.1 Supersymmetric Theory

Phenomenological applications of SUSY theories have been considered since the late 1970 in connection with the hierarchy problem in the SM. The fundamental idea of the Supersymmetic theory is the existence of a symmetry between fermions and bosons. The symmetry can be realized in nature if one assumes that for each particle of the SM exists a supersymmetric partner, which has the same internal quantum number and an intrinsic angular momentum which differs by half a unit from the partner of the SM. These symmetry between bosons and fermions have the fundamental property of producing cancellations, at each order, of divergent diagrams of the Higgs boson mass, solving the hierarchy problems. If supersymmetry is manifestly broken in nature then Supersymmetry-breaking terms can be included in the theory; the simplest model is called the Minimal Supersymmetric Standard Model (MSSM). In this model the scale of SUSY breaking is around the TeV [44]. The particles of the MSSM are given in Table 1.3.

1.2.2 Grand Unified Theory

The SM unifies electromagnetic and weak interactions based on the $SU(2)_L \times U(1)_Y$, but does not unify the strong interaction, this because the magnitudes of coupling constants are different and independent. These three coupling constants are named running because they are functions of energy: while the electromagnetic coupling rise up with energy, the strong and weak couplings decrease, so it is very attractive to think about if these three constants will converge at some energy scale.

The GUT is a theory which tries to unify electroweak interaction and strong interaction, assuming the existence of a group which can embed SU(3)$_C\times$ SU(2)$_L\times$U(1)$_Y$. In one of GUT theory, called SU(5), it is expected that all the interactions are unified at the m_{GUT} scale ($\approx10^{16}$ Gev). Another possible GUT theory is the SO(10) group [46, 50]. It contains SU(5) as a sub algebra. The advantage of this group is that can accommodate also a right handed neutrino.

1.3 The muon decay

Muons are unstable particles and in the SM they decay through the weak interaction into other leptons. In most cases the muons decay through the charged weak current interaction mediated by $W^{\pm}_{\mu}$ gauge bosons. The dominant muon decay (known as Michel decay) mode is:

$$\mu^- \to e^- \bar{\nu}_e \nu_\mu \; (\mu^+ \to e^+ \nu_e \bar{\nu}_\mu)$$

moreover it may decay, with smaller branching ratios, in:

- Radiative muon decay (RMD): $\mu^- \to e^- \bar{\nu}_e \nu_\mu \gamma$ ($\mu^+ \to e^+ \nu_e \bar{\nu}_\mu \gamma$);
- Associated e^+e^- pair: $\mu^- \to e^- \bar{\nu}_e \nu_\mu e^+ e^-$ ($\mu^+ \to e^+ \nu_e \bar{\nu}_\mu e^+ e^-$);

In these decays, the lepton flavor quantum number is conserved at each decay vertex and the principle of Lepton Flavor Conservation is therefore fulfilled. The upper limit of some "rare" decay modes at 90% confidence level are summarized in Table 1.4:

1.3.1 The $\mu \to e\gamma$ decay in the SM

In the Standard Model, lepton flavour is conserved thanks to the symmetry of the Lagrangian. However, in order to describe the neutrino oscillation one has to introduce mass terms for the neutrinos. When the neutrino mixing is considered,

Table 1.4: Decay modes and branching fractions of muon

Decay mode	Branching Ratio	Confidence Level	Reference
$\mu^- \to e^- \bar{\nu}_e \nu_\mu$	$\simeq 100\%$		
$\mu^- \to e^- \bar{\nu}_e \nu_\mu \gamma$	$(1.4 \pm 0.4) \times 10^{-5}$		[22]
$\mu^- \to e^- \bar{\nu}_e \nu_\mu e^+ e^-$	$(3.4 \pm 0.4) \times 10^{-5}$		[29]
$\mu^- \to e^- \nu_e \bar{\nu}_\mu$	$< 1.2\%$	90%	[23]
$\mu^- \to e^- \gamma$	$< 4.2 \times 10^{-13}$	90%	[74]
$\mu^- \to e^- e^- e^+$	$< 1.0 \times 10^{-12}$	90%	[27]
$\mu^- \to e^- 2\gamma$	$< 7.2 \times 10^{-11}$	90%	[9]

cLFV process is possible and it opens to the possibility for the existence of $\mu \to e\gamma$ decay as shown in Figure 1.1. The SM allows to evaluated:

$$\Gamma(\mu \to e\bar{\nu}\nu) = \frac{G_F^2 m_\mu^5}{192\pi^3} F\left(\frac{m_e^2}{m_\mu^2}\right) \tag{1.1}$$

and considering the SM with neutrino oscillation the $\mu \to e\gamma$ decay width can be evaluated:

$$\Gamma(\mu \to e\gamma) = \underbrace{\frac{G_F^2 m_\mu^5}{192\pi^3}}_{\mu-decay} \underbrace{\frac{\alpha}{2\pi} \sin^2(2\theta_{12})}_{\gamma-vertex} \underbrace{\left(\frac{\Delta m_{12}^2}{m_W^2}\right)^2}_{\nu-mixing} \tag{1.2}$$

where $G_F = (1.166 \cdot 10^{-5}) GeV^{-2}$ is the Fermi coupling constant, m$_\mu$, m$_e$ and m$_w$ are the mass of μ, e and W vector boson, θ_{12} is the mixing angle , Δm_{12} is the neutrino eigenstates mass differences and α is the fine-structure constant.

Hence the resulting Branching Ratio (B.R.), normalized to the muon decay, with the measured values for neutrino oscillations parameters, is:

$$\mathcal{B.R.}(\mu \to e\gamma) = \frac{\Gamma(\mu \to e\gamma)}{\Gamma(\mu \to e\bar{\nu}\nu)} = \frac{3\alpha}{32\pi} \left| \sum_{i=2,3} U_{\mu i}^* U_{ei} \frac{\Delta m_{i1}^2}{m_W^2} \right|^2 \approx 10^{-55} \tag{1.3}$$

where U_{xi} are the elements of the neutrino mixing matrix.

It is clear that such a value is too small to be measured experimentally. Therefore one can conclude that the cLFV process are severely suppressed in the SM alone, even by taking into account neutrino oscillation.

1.3.2 The $\mu \to e\gamma$ decay in the BSM

The $\mu \to e\gamma$ decay in the SM has a small probability, whereas, in the NP theories this decay may be allowed with a $\mathcal{B.R.}$ value measurable with current experiments.

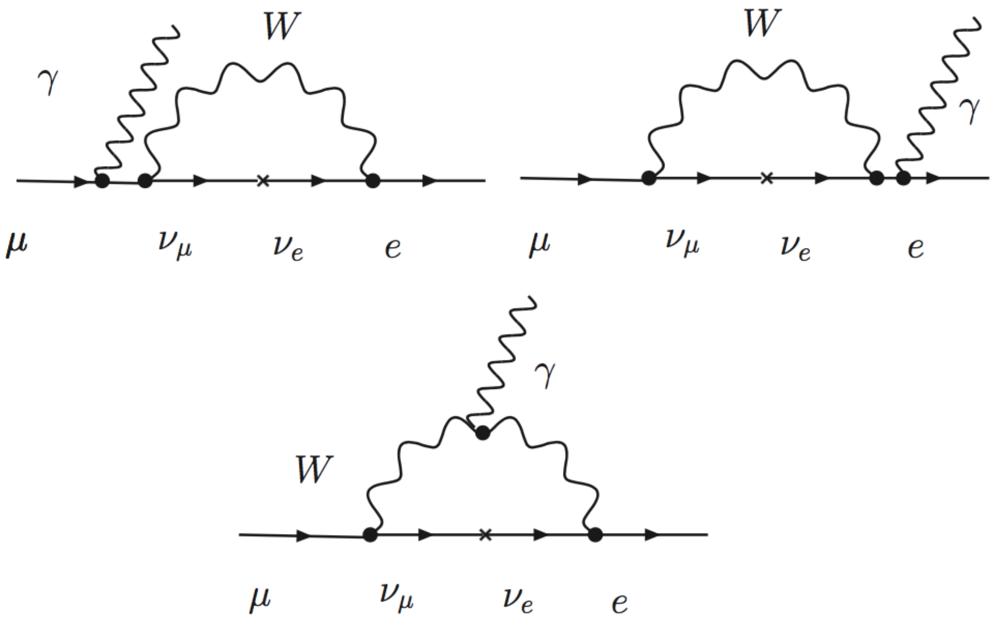

Figure 1.1: Feynman diagrams for $\mu \to e\gamma$ decay via neutrino oscillation.

In particular, in the SUSY theories, the $\mu \to e\gamma$ decay branching ratio can be represented as:

$$\mathcal{B}.\mathcal{R}.(\mu \to e\gamma) = \frac{\alpha^3 \pi \theta_{\tilde{e}\tilde{\mu}}}{G_F^2 \tilde{m}^4} \tan^2\beta \tag{1.4}$$

where $\tan\beta$ is the ratio of the expectation values of two Higgs fields. From Equation 1.4, the BR ranges from 10^{-15} to 10^{-13} in SU(5) (Figure 1.2) and from 10^{-13} to 10^{-11} in SO(10). In the SU(5), LFV appears only in the right-handed slepton sector for moderate values of $\tan\beta$, instead in the $SO(10)$ LFV processes are mediated by both the left and the right handed sleptons and a unique loop integral, with dimensions of the inverse of a squared mass [44, 79, 14]. In the Figure 1.3 and Figure 1.4 the Feynman diagrams for $\mu \to e\gamma$ are represented.

In non-GUT SUSY models, as the SUSY seesaw model, right-handed heavy Majorana neutrinos are introduced to explain the tiny masses of neutrinos by the seesaw mechanism. Hence the branching ratio of cLFV processes are expected to be enhanced. Figure 1.5 shows the scatter plot of the correlation between $\mathcal{B}.\mathcal{R}.(\mu \to e\gamma)$ and $\mathcal{B}.\mathcal{R}.(\tau \to \mu\gamma)$ in one example of the SUSY seesaw model.

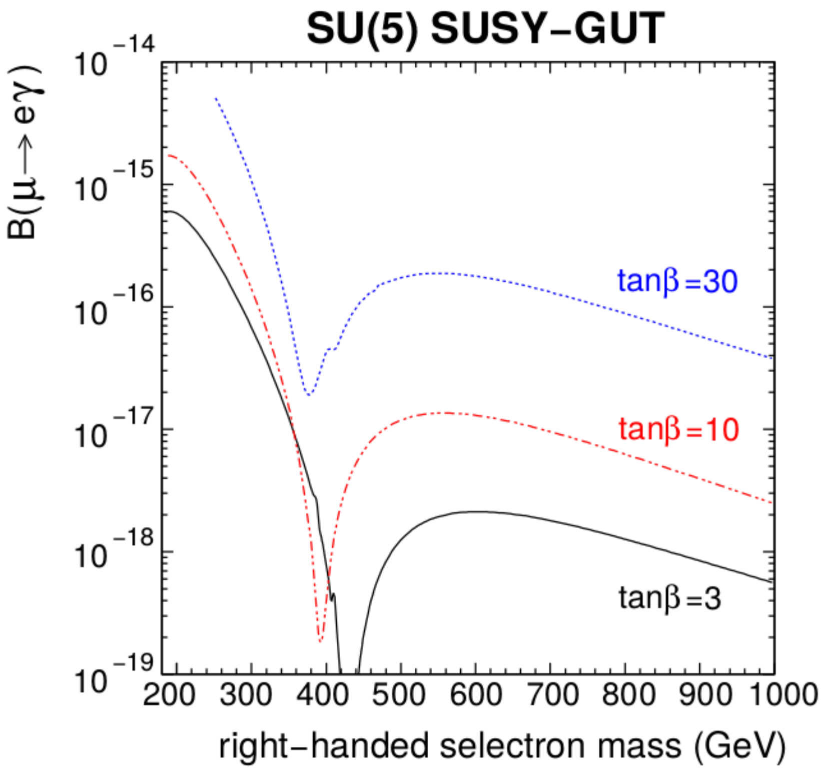

Figure 1.2: B.R.($\mu \to e\gamma$) as a function of the right-handed selectron mass in SU(5)model.

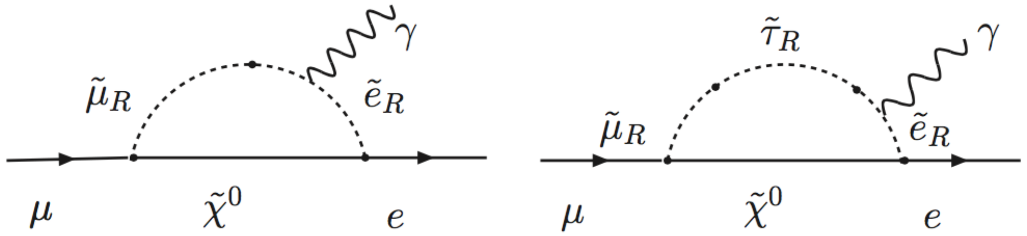

Figure 1.3: Feynman diagrams for $\mu \to e\gamma$ in SUSY-GUT $SU(5)$ model. The closed blobs represent the flavour transitions due to the off-diagonal terms of the slepton mass matrices.

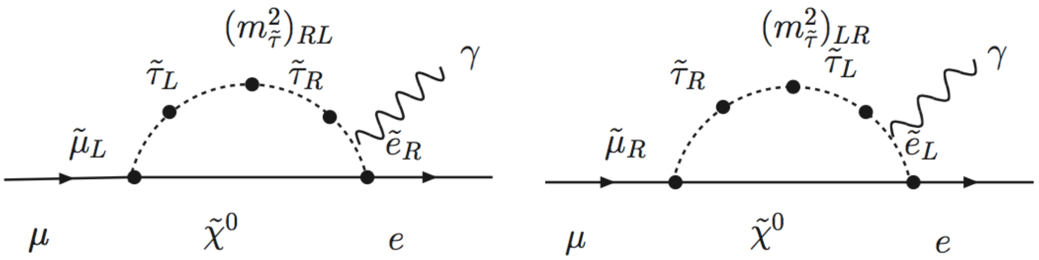

Figure 1.4: Feynman diagrams for $\mu \to e\gamma$ in SUSY-GUT $SO(10)$ model.

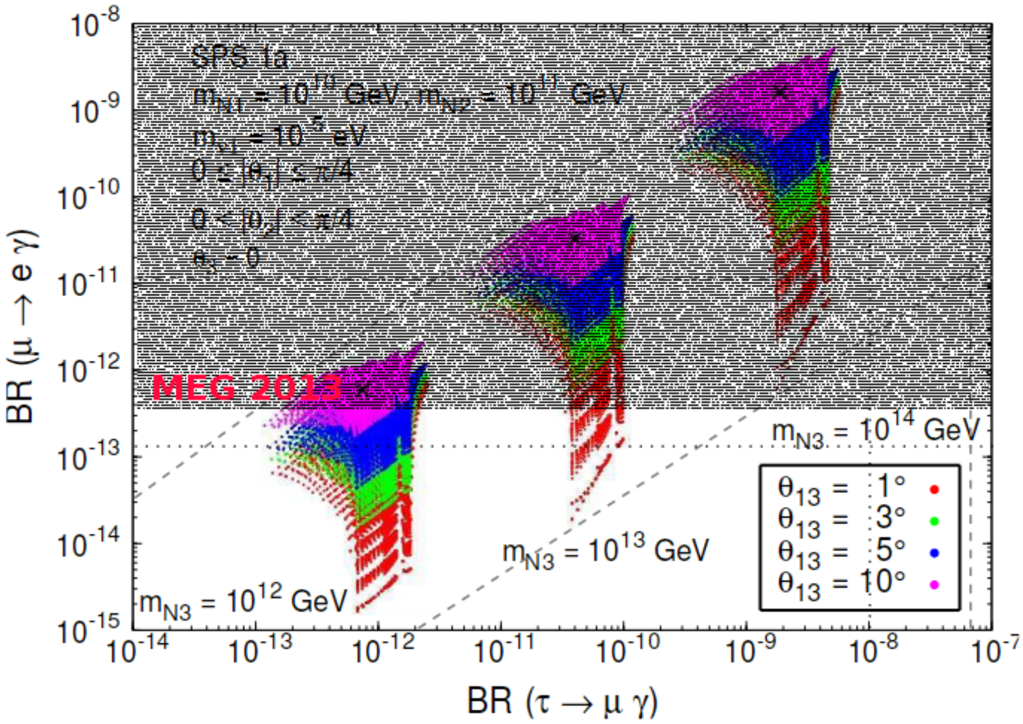

Figure 1.5: SUSY seesaw model predictions for $\mu \to e\gamma$ versus for $\tau \to \mu\gamma$ as a function of θ_{13} [92]

1.4 History and status of cLFV searches experimental

The lepton μ was discovered in the 1937 by Neddermeyer and Anderson while studying cosmic ray flux with a cloud chamber. The particle could have both positive and negative charge and a mass approximately 200 times the mass of the electron. Initially this particle was thought to coincide with the short-range strong force mediator predicted by Yukawa. Conversi, Pancini and Piccioni later proved this to be untrue.

The muon is a useful tool to probe the SM and to search for physics BSM in the cFLV sector. The advantages of using muons is the absence of strong interactions and an almost-macroscopic mean life ($\tau_\mu = (2.1969811 \pm 0.0000022) \times 10^{-6}$ s). Further, a low energy muon produces only electron, positron, gamma ray and neutrinos with only a very limited number of decay channels.

Nowdays, the muon decay channels, called *golden channels*, used for the study of the cLFV processes [51, 36], suppressed in the SM, are:

- $\mu^+ \rightarrow e^+\gamma$ ($\mathcal{B.R.}$ <4.2×10^{-13}@90%C.L., MEG [74])
- $\mu^+ \rightarrow e^+e^-e^+$ ($\mathcal{B.R.}$ <1.0×10^{-12}@90%C.L., SINDRUM [28])
- $\mu N - eN$ conversion in nuclei, ($\mathcal{C.R.}$ <7.0×10^{-13}@90%C.L., SINDRUM II [26])

In order to compare the *golden channels*, a model-independent effective Lagrangian can be used:

$$\mathcal{L} = \underbrace{\frac{m_\mu}{(\kappa+1)\Lambda^2}\bar{\mu}_R\sigma_{\mu\nu}e_L F^{\mu\nu}}_{magnetic-moment\ type\ operator} + \underbrace{\frac{\kappa}{(\kappa+1)\Lambda^2}\bar{\mu}_L\gamma_\mu e_L(\bar{e}\gamma^\mu e)}_{four-fermion\ operator} + h.c. \tag{1.5}$$

where L and R indicate the chirality and $F^{\mu\nu}$ is the photon field strength. The two independent constants Λ and κ represent respectively the mass scale of the new physics and a dimensionless parameter that determines whether the dipole-like or the four-fermion interaction is dominant. For $\kappa \ll 1$, the dipole-type operator dominates CLFV phenomena, while for $\kappa \gg 1$ the four-fermion operators are dominant. Figure 1.6 shows the sensitivity of the cLFV processes to the scale of New Physics (NP). From the Figure 1.6, it can be noticed that the $\mu \rightarrow e\gamma$ decay can probe only the dipole-dominating region, while the $\mu N - eN$ conversion and the $\mu \rightarrow 3e$ decay can also explore the four-fermion region (one-loop level). The search of cLFV processes in the muon sector is important in order to understand the mechanisms of NP and of cLFV. There are several experiments looking for these mechanisms, the MEG experiment, described in the next chapters, searches for $\mu \rightarrow e\gamma$, while other experiments to search for $\mu^+ \rightarrow 3e$ (Mu3e at PSI [1]) and $\mu N - eN$ conversion (Mu2e at Fermilab [80], Comet at J-Park [40]), these are described in the following. Figure 1.7 shows the cLFV searches improvements in the muon sector [101].

1.4.1 The $\mu^+ \rightarrow e^+\gamma$

Experimental searches for $\mu^+ \rightarrow e^+\gamma$ have a history longer than 50 years. The first search for the $\mu^+ \rightarrow e^+\gamma$ decay starts in 1947 and a first upper limit was reached: $\mathcal{B.R.}$<10%. The experiment used Geiger-Muller counters to detect the meson and

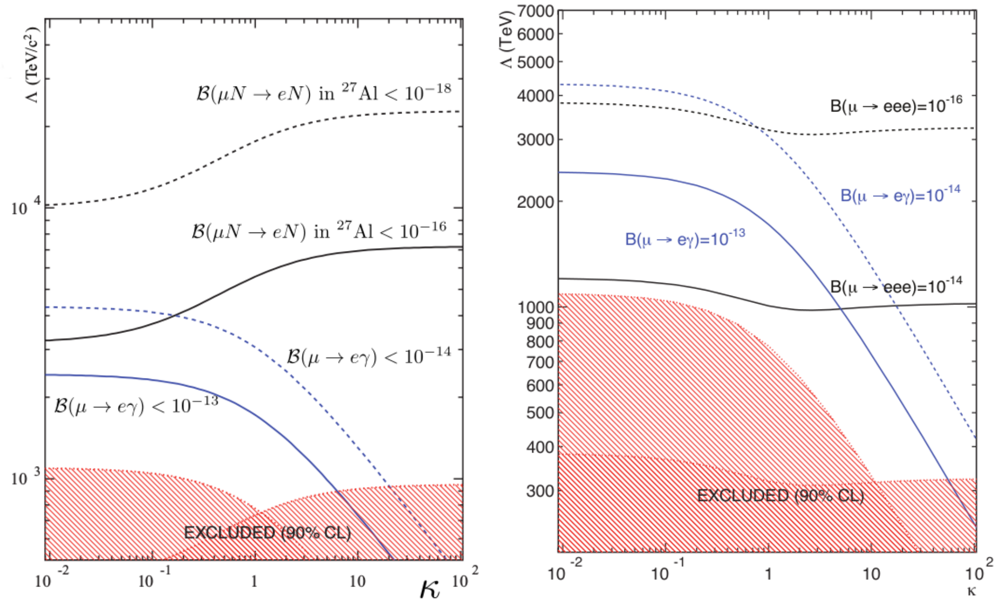

Figure 1.6: The sensitivity to Λ as a function of κ for $\mu \to e\gamma$ and $\mu N - eN$ conversion (left), $\mu^+ \to 3e$ (right)

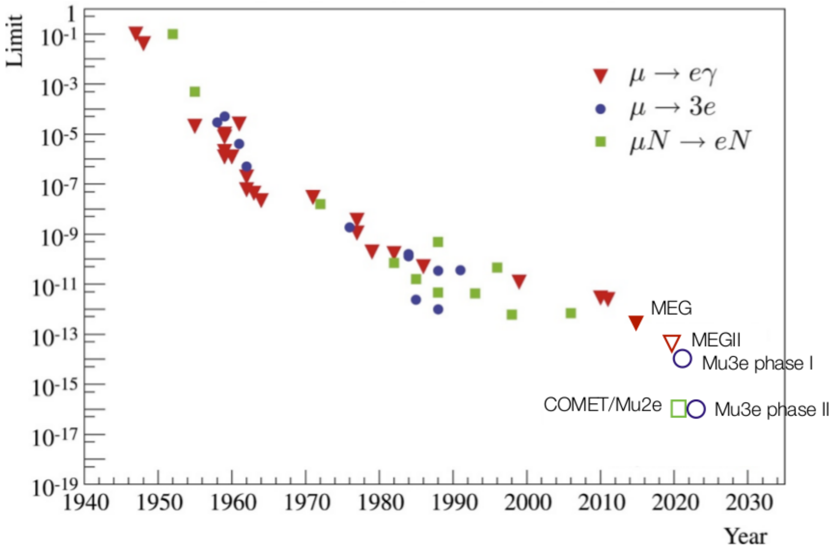

Figure 1.7: Experimental upper limit for cLFV processes as a function of the years.

Table 1.5: Historical progress of search for $\mu \longrightarrow e\gamma$

Year	90%CL on B.R.	Collaboration/Lab	Reference
1947	1.0×10^{-1}	Chalk River	Hincks and Pontecorvo (1948)
1955	2.0×10^{-5}	Nevis	Steinberger and Lokanathan (1955)
1959	7.5×10^{-6}	Liverpool	O'Keefe et al. (1959)
1959	2.0×10^{-6}	Nevis	Berley et al. (1959)
1959	1.0×10^{-5}	Rochester	Devis et al. (1959)
1959	1.2×10^{-6}	CERN	Ashkin et al. (1959)
1960	1.2×10^{-6}	LBL	Frankel et al. (1960)
1961	2.5×10^{-5}	Carnegie	Crittenden et al. (1961)
1962	1.9×10^{-7}	LBL	Frankel et al. (1962)
1962	6.0×10^{-8}	Nevis	Bartlett et al. (1962)
1963	4.3×10^{-8}	LBL	Frankel et al. (1962)
1964	2.2×10^{-8}	Chicago	Parker et al. (1964)
1971	2.9×10^{-8}	Dubna	Korenchenko et al. (1961)
1977	3.6×10^{-9}	TRIUMF	Depommier et al. (1977)
1977	1.1×10^{-9}	SIN	Povel et al. (1977)
1979	1.9×10^{-10}	LAMPF	Bowman et al. (1979)
1982	1.7×10^{-10}	LAMPF	Kinnison et al. (1982)
1986	4.9×10^{-11}	LAMPF/Crystal Box	Bolton et al. (1986, 1988)
1999	1.2×10^{-11}	LAMPF/MEGA	Brooks et al. (1999)
2010	2.8×10^{-11}	PSI/MEG	Adam et al. (2010)
2011	2.4×10^{-12}	PSI/MEG	Adam et al. (2011)
2013	5.7×10^{-13}	PSI/MEG	Adam et al. (2013)
2016	4.2×10^{-13}	PSI/MEG	Baldini et al. (2016)

the decay particles. In 1955 a new upper limit of $\mathcal{B}.\mathcal{R}.<2\times10^{-5}$@90%C.L. was set using the Nevis cyclotron at the Columbia University, where π^+ beams were stopped on a carbon target and two detectors, one for the 50 MeV electrons and the other for the γ rays were used to detect the decay.

From the middle of 1970s a new generation of $\mu^+ \rightarrow e^+\gamma$ decay experiments started, using high-intensity muon beams instead of pion beams. In particular in 1982 an upper limit of $\mathcal{B}.\mathcal{R}.<1.7\times10^{-10}$@90%C.L. was obtained at LAMPF, where for the first time the "surface muon beam" was used. Owing to this technique, high-intensity μ^+ beam can be stopped in a very thin target. As the muon rate increases, the rate of background also increases. Table 1.5 illustrates the chronological improvement of the $\mu^+ \rightarrow e^+\gamma$ search experiments. The best pre-MEG upper limit of $\mathcal{B}.\mathcal{R}.<1.2\times10^{-11}$@90%C.L. comes from MEGA experiment at the LAMPF [17]. Since 2008, the MEG experiment has set new upper limit, the last one ($\mathcal{B}.\mathcal{R}.$ $<4.2\times10^{-13}$@90%C.L.) in 2016.

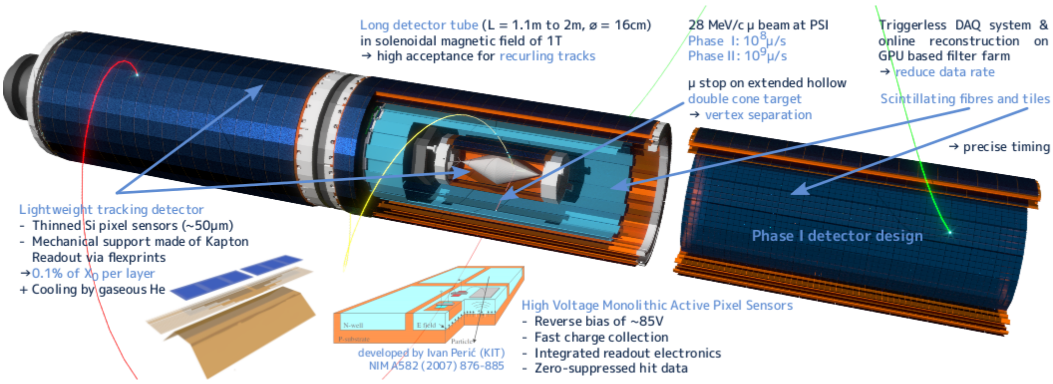

Figure 1.8: Mu3e detector

1.4.2 The $\mu^+ \to e^+e^-e^+$

The present experimental limit on branching ratio for $\mu^+ \to e^+e^-e^+$ decay is $\mathcal{B.R.} < 1.0 \times 10^{-12} @ 90\% C.L.$, obtained by SINDRUM in 1988 [28]. The detector was a solenoid spectrometer equipped with a MWPCs system coaxial with the beam. In this case, the event background was subdivided into two classes, the correlated and the uncorrelated backgrounds. The first one is a prompt background; $\mu^+ \to e^+e^-e^+\nu_e\bar{\nu}_\mu$, which is allowed in the SM and can fake a signal when two neutrinos have low energies. The uncorrelated background is produced by the accidental coincidence of a normal Michel positron with an e^+e^- pair, for example, produced by the Bhabha scattering in the target of another Michel positron, or from a radiative γ.

One experiment, Mu3e [1] (In Figure 1.8 the detector layout), for the search of this decay with a sensitivity 10^4 times higher than the present upper limit, has been proposed and approved at PSI.

1.4.3 The $\mu N - eN$ conversion in nuclei

One of the *golden channels* for searching of cLFV is $\mu N - eN$ conversion in nuclei [41]. A negative muon is stopped in a material and it is quickly captured by an atom into a high orbital momentum state, forming a muonic atom. Then it rapidly cascades to the lowest quantum state $1S$ and it can either decay in an orbit with the

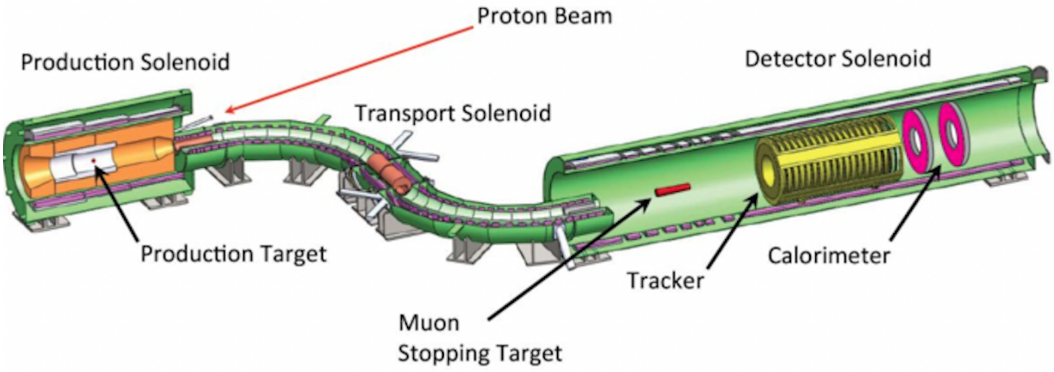

Figure 1.9: Mu2e detector

Michel process or be captured by the nucleus. In the context of the NP, the exotic process of $\mu - e$ conversion in nuclei such as

$$\mu^- + (A, Z) \rightarrow e^- + (A, Z) \tag{1.6}$$

is expected, which violates the conservation of the lepton flavor numbers. The signal of $\mu^- - e^-$ conversion in nuclei is a monochromatic electron emitted with energy:

$$E_e \approx m_\mu - B_\mu \tag{1.7}$$

where B_μ is the binding energy of the $1S$ muonic atom, and it depends on the nucleus. This process is not affected by any accidental background. The background comes from the normal muon decay in orbit (DIO). Other backgrounds could be caused by the decay in flight or interactions of particles (muon, pion, (anti)proton) generated by the primary proton beam. Since the muonic atoms have lifetimes of the order of 1 μs, the beam originated backgrounds can be suppressed by using high-intensity pulsed beam and collecting data only outside the beam window. The current upper limit has been set by the SINDRUM-II experiment at 7.0×10^{-13}@90%C.L. [26]. In the near future, two different experiments are being prepared to search for the $\mu^- - e^-$ conversion. One is the Mu2e [80](In Figure 1.9 a detector layout) experiment at Fermilab (USA) and the other is the COMET experiment [40] at J-PARC (Japan). The sensitivities goal for both experiments are similar, at the level 10^{-17}.

1.4.4 The τ decay

The experimental searches for cLFV processes of tau lepton channel are carried out by B-factory experiments such as Belle, BaBar and LHCb. Many different cLFV decays modes are possible for the τ lepton. Here only some decay modes are listed. Current upper bounds are:

- $\tau \to \mu\gamma$ $\mathcal{B}.\mathcal{R}. < 4.4 \times 10^{-8} @ 90\% C.L.$ (BABAR [34])
- $\tau \to e\gamma$ $\mathcal{B}.\mathcal{R}. < 3.3 \times 10^{-8} @ 90\% C.L.$ (BABAR [34])
- $\tau \to \mu\mu\mu$ $\mathcal{B}.\mathcal{R}. < 2.1 \times 10^{-8} @ 90\% C.L.$ (BELLE [15])
- $\tau \to eee$ $\mathcal{B}.\mathcal{R}. < 2.7 \times 10^{-8} @ 90\% C.L.$ (BELLE [15])

In the near future, SuperKEKB electron positron collider in Japan is in construction with high luminosity and Belle II experiment will collect data with a 50 times more statistics than Belle. The LHCb experiment is currently taking data at the LHC.

Kinematics and Background

2

Recent theoretical developments calculate rates for some cLFV processes involving muon decays that are close to the present experimental limit. In the present Chapter we will review a phenomenological treatment of the $\mu^+ \to e^+\gamma$ *decay and the two main sources of background for the decay.*

2.1 Decay Kinematics

The event signature of $\mu^+ \to e^+\gamma$ decay is very simple kinematically. It is a two-body decay. Positive muons are stopped in a thin target and their decay occurs at rest. The thin target minimizes multiple scattering effects that could spoil the measurements of the daughter positron kinematic variables. A μ^- is not suitable to be used, since it would be captured by a nucleus when it is stopped in a material and the captured muons by the nucleus typically cause the nucleus to eject protons, neutrons and photons, which produce accidental rates in the detector. The event is an e^+ and a γ emitted in coincidence, moving collinearly back-to-back with their energies equal to half the muon mass ($m_\mu/2$ = 52.8 MeV), as depicted in Figure 2.1.

Each event is described by five observables: the photon and positron energy (E_γ, E_e), their relative angles ($\theta_{e\gamma}$, $\varphi_{e\gamma}$) and the relative emission time ($t_{e\gamma}$). To identify experimentally the process, one should look for a photon and a positron:

1. moving collinearly back-to-back, e.g. $\theta_{e\gamma} = \pi$;
2. produced simultaneously and detected in coincidence e.g. $\Delta t_{e\gamma}$=0;
3. having exactly an energy $E = m_\mu/2$ both.

In order to precisely identify the event, good angular, timing and energy resolutions and efficient algorithm for signal/background discrimination are required.

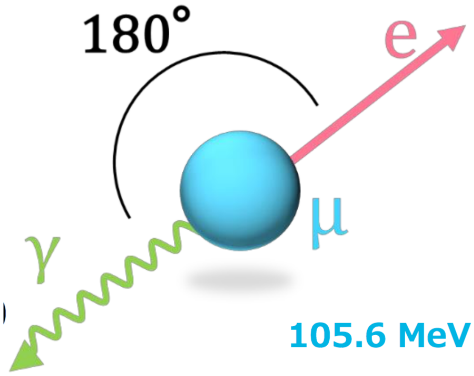

Figure 2.1: $\mu^+ \to e^+\gamma$ decay event signature.

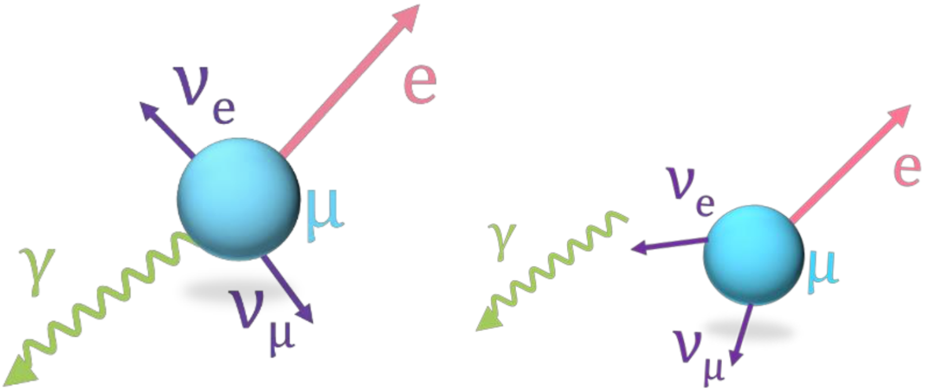

Figure 2.2: Left:Physic background. Right:Accidental background.

2.2 Background

There are two major background sources [64] that can mimic a $\mu^+ \to e^+\gamma$ event signature. One is the physics background (Figure 2.1: left) from radiative muon decay (RMD, [102]), $\mu^+ \to e^+\bar{\nu}_e\nu_\mu\gamma$, the other is an accidental background (Figure 2.1: right) from a coincidence of uncorrelated events, e.g. an e^+ of a Michel muon decay, with a photon from positron-electron annihilation-in-flight (AIF) or bremsstrahlung . In the following section will explain the characteristics and the contributions of each kind of background.

2.2.1 The physics background

The physics background is given by the RDM $\mu^+ \rightarrow e^+\bar{\nu}_e\nu_\mu\gamma$ where the e^+ and γ are emitted with an angle close to 180° and two neutrinos carrying off a negligible amount of energy. Moreover, the e^+ and γ have approximately the same energy as in the signal event. The spectrum of photons from radiative decay is shown in (Figure 2.3: left). The differential RMD width is tipically expressed as a function of x=2E_e/m$_\mu$, y=2E_γ/m$_\mu$ and z=$\pi - \theta_{e\gamma}$. For x=y=1 and z=0, corresponding to the region of signal, the width of decay vanishes but the finite experimental resolutions introduce background events that ultimately limit the achievable sensitivity [64]. The probability of a background event to fall in the signal region is easily computed given the experimental resolutions x, y and z and integrating the differential RMD width in the signal region. From Figure 2.3(right) can be seen that with detector resolutions on the $\sim$ 1% scale, sensitivities of 10^{-15} can be achieved.

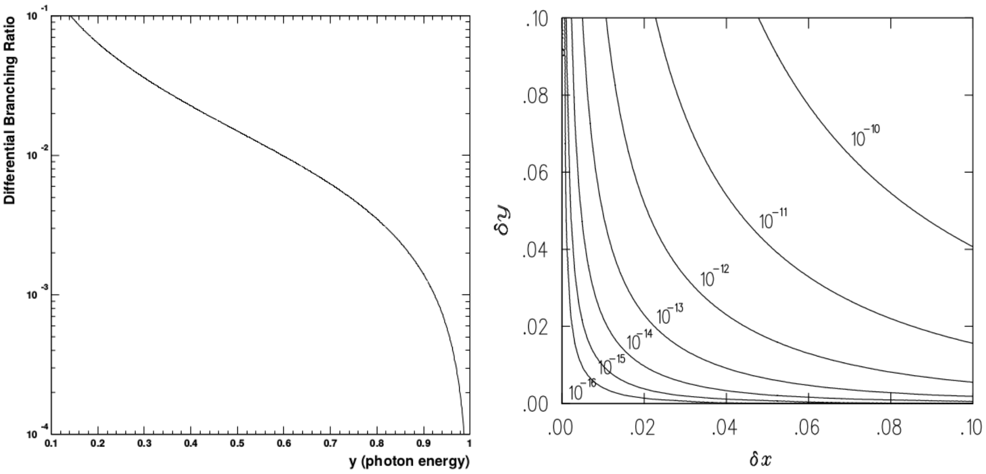

Figure 2.3: Left: Differential branching ratio of the RMD as a function of the photon energy. Right: Effective branching ratio of the physics background from the RMD as a function of the e^+ energy resolution (δx) and photon energy resolution (δy)[64]

2.2.2 The accidental background

Accidental background originates from two distinct events producing a positron and a photon in accidental temporal coincidence and spatial collinearity that closely match the event signature. The positrons can only originate from Michel decay and hence from the pure muon beam exploited by the experiment. The photons can originate from multiple sources, such as RMD, positron AIF and bremsstrahlung. All those sources are dependent from the beam muon flux on the stopping target (R_μ). The contribution of photons coming from RDM can be estimated by integrating the RMD spectrum over the E_γ signal, while the contribution from AIF depends on the amount of material traversed. Figure 2.4 shows the integrated rates of backgrounds as a function of the photon energy [64]. The accidental background is dominant and it is determined by the detector resolutions of the MEG experiment. The expected number of accidental background events (N_{acc}) in a time window T can be expressed as:

$$N_{acc} \propto R_\mu^2 \times \Delta E_\gamma^2 \times \Delta P_e \times \Delta\theta_{e\gamma}^2 \times T \times \Delta t_{e\gamma} \tag{2.1}$$

The accidental background rate scales quadratically with R_μ. Therefore this is the most important background in present and future experiments. The MEG experiment background is mainly affected by accidental events, so keeping their rate as low as possible is essential.

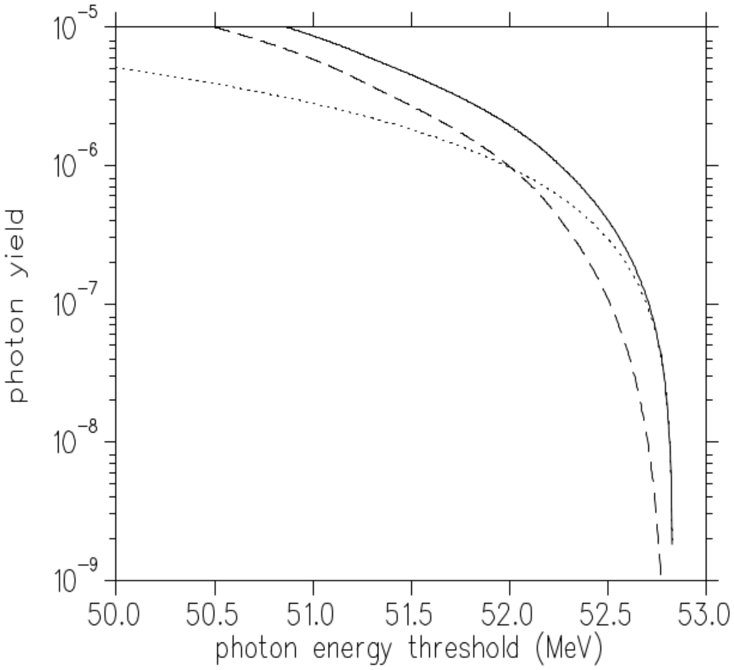

Figure 2.4: Integrated rates from annihilation-in-flight taking a mass-thickness of 50 mg/cm^2 for the muon stopping target (a dotted line) and radiative muon decay (a dashed line) as a function of the photon energy.[64]

2.3 Single Event Sensitivity (SES)

The number of expected signal events N_{sig} depends on the solid angle Ω subtended by the detectors (the acceptance of the apparatus), on the efficiencies of the detectors (ϵ_γ, ϵ_e) and of the selection criteria (ϵ_s). In a measurement time T, for a given branching ratio B.R., it yields:

$$N_{sig} = R_\mu \times T \times \mathcal{B}.\mathcal{R}. \times \Omega \times \epsilon_\gamma \times \epsilon_e \times \epsilon_s \tag{2.2}$$

In those experiments where the expected decay is not observed it is possible to define the SES and set an upper limit on B.R. with a certain confidence level (normally 90%). The strategy adopted by the MEG collaboration to extract a limit on the B.R. from the number of detected signal events is based on the Feldman and Cousins approach[45]. The SES is defined as the B.R. for which the average number of expected signal events is equal to 1 in absence of background:

$$SES = \mathcal{B}.\mathcal{R}.(\mu \to e\gamma) = \frac{1}{R_\mu T \Omega} \frac{1}{\varepsilon_e \varepsilon_\gamma \varepsilon_s} \tag{2.3}$$

Therefore SES parameter summaries the performances of the detector: a low SES implies acceptance, hence efficiencies, should be maximized. In addition, background rejection (see Equation 2.1) requires good resolutions on the kinematic parameters, with special attention on photon energy and emission angle, whose contribution is squared.

2.4 Final Remark

A search for a rare decay of muons requires an intense muon beam and an excellent performance of detectors for both a gamma and a positron in order to avoid pileup and to reach the interesting region. The MEG apparatus is a result of a trade-off among several requirements of the various detectors in order to obtain:

- a high intensity continuous muon beam (the use of a continuos source instead of a pulsed one is necessary in order to minimize the background);

- an excellent background rejection;
- a positron tracker which can measure high-rate momentum and angles positrons precisely;
- a gamma-ray detector with excellent energy resolution;
- a timing counter with excellent time resolution;

Part II

MEG Apparatus

3

MEG I Apparatus

The MEG experiment, designed to search for $\mu^+ \to e^+\gamma$ *decay, is located at the Paul Scherrer Institute (PSI) in Switzerland. It started the physics data taking in 2008 and an upgraded MEG detector was approved in 2013.*

Dedicated detectors were constructed in order to achieve the sensitivity goal for the decay search [75] but the MEG detector had some limitation. For this reason, the need of an upgraded MEG is due to the fact that the experiment sensitivity is strongly limited by the accidental background, which can be reduced by improving the single detectors resolutions. The upgrade takes over the basic concept of MEG experiment, while almost all major detectors are upgraded. The sensitivity improvement will be achieved by 10 times larger collection data, and detector resolutions improved by a factor of two. In this chapter, first we will describe all sub-detectors of the MEG detector and the obtained results and then we will introduce the sub-detectors of MEG II experiment and their improvements.

3.1 The muon beam line

Searching for the rare muon decay requires as much statistics as possible (intensity). At the same time, a low rate of the accidental background is necessary, which, however, increases as the instantaneous intensity of the beam. So, a direct current (DC) muon beam is preferable to a pulsed beam. The MEG experiment is being conducted at the πE5 beamline where the most intense DC μ^+ beam, provided by the 590 MeV proton ring cyclotron facility of PSI, is available.

3.1.1 PSI accelerator facility

The MEG experiment uses a secondary beam produced by the High Intensity Proton Accelerators (HIPA). HIPA consists of three accelerators, Cockcroft-Walton accelerator, Injector 2 cyclotron and main ring cyclotron [32]. At first, the proton beam is pre-accelerated to an energy of 870 keV with Cockcroft-Walton Pre-Injector from a source made up of hydrogen atoms. Then the PSI Injector 2 cyclotron with 4 spectromagnets provides 72 MeV protons with 0.2% FWHM spread, 50.63 MHz frequency (19.75 ns interval) and 0.3 ns width of a bunch from the 870 keV injector.

Final acceleration of the main beam to 590 MeV occurs in the Proton Ring Cyclotron (Figure 3.1) with a diameter of approximately 15 meters, which consists of eight magnets sector and four accelerator cavities. The accelerator normally delivers a proton beam of 590 MeV energy at a current up to 2.2 mA. The main characteristics of the cyclotron accelerator are summarized in Table 3.1. The proton beam impinges on two rotating[1] graphite targets, in sequence, the M target (Mince, thin, 7 mm) and the E-target (Epais, thick, 40-60 mm). The two targets feed seven different pion and muon beam lines, simultaneously available.

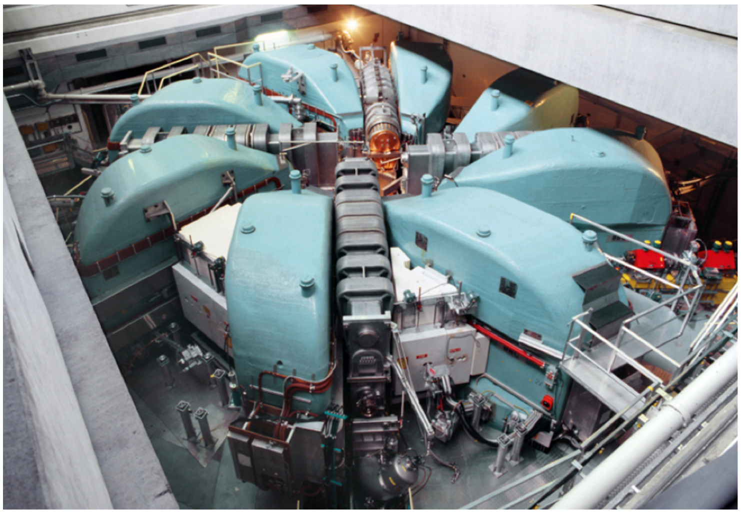

Figure 3.1: Paul Scherrer Institute Proton Ring Cyclotron $590 MeV$

The MEG experiment uses πE5 beam line (Figure 3.2), one of five branches from target E, because its magnetic channel has the highest acceptance for surface muons. It is placed at 175° from the proton beam and it collects low-energy (10-120 MeV/c) muons as daughter particles of the pions. The main properties of πE5 beam line are

---

[1] the target keeps on rotating during the operation for cooling and to avoid thermal stresses.

Table 3.1: Main characteristics of PSI cyclotron proton beam [91]

Characteristics	Value
Injection energy	72 MeV
Extraction energy	590 MeV
Extraction momentum	1.3 GeV/c
Relative energy spread (FWHM)	1.2%
Beam emittance	2 mm $\times\pi$ mrad
Beam current	>1.8 mA DC
Accelerator frequency	50.63 MHz
Time between pulses	19.75 ns
Bunch width	0.3 ns

Table 3.2: $\pi E5$ beam line properties.

Characteristics	Value
Beam line length	10.4 m
Solid angle acceptance	150 msr
Momentum range	$20 \div 120$ MeV/c
Relative momentum resolution (FWHM)	2%
Relative momentum band (FWHM)	10%
Beam spot (FWHM)	15×20 mm^2
Horizontal emittance	>15.3 cm·rad
Vertical emittance	3.6 cm·rad

summarized in Table 3.2.

Charged pions produced inside the graphite target decay, $\pi^\pm \to \mu^\pm\nu_\mu$, with the lifetime about 26 ns, emitting polarized muons and neutrinos. This generates a quasi-continuous muon beam, by smearing the 19.75 ns cycle of the initial proton pulses. The momentum of muons from pion decay at rest is 29.8 MeV/c. Therefore, the muons, originated from the pions stopped near the surface of the production target, have a regulated momentum of approximately 29.8 MeV/c. This is called surface muon, which has a low energy loss and a low depolarization during a short pass length in a target [5, 12]. Muons from pions flying outside the target have higher momenta, and are called cloud muon. Figure 3.3 shows the pion and muon beam flux available at πE5 Beam line. With a proper choice of the extraction parameters, it is possible to select only the surface muons and they can be easily stopped in a thin target (like the MEG I), in order to reduce the multiple scattering phenomena. The surface muon beam is contaminated with positrons, which need to be removed before they reach the MEG detector.

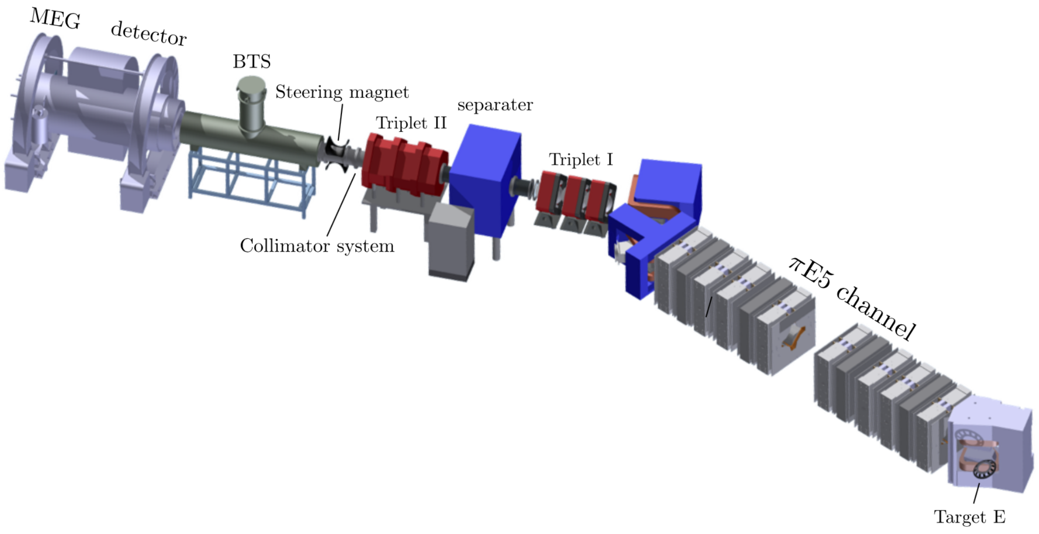

Figure 3.2: Schematic of the $\pi E5$ channel and MEG beam transport system.

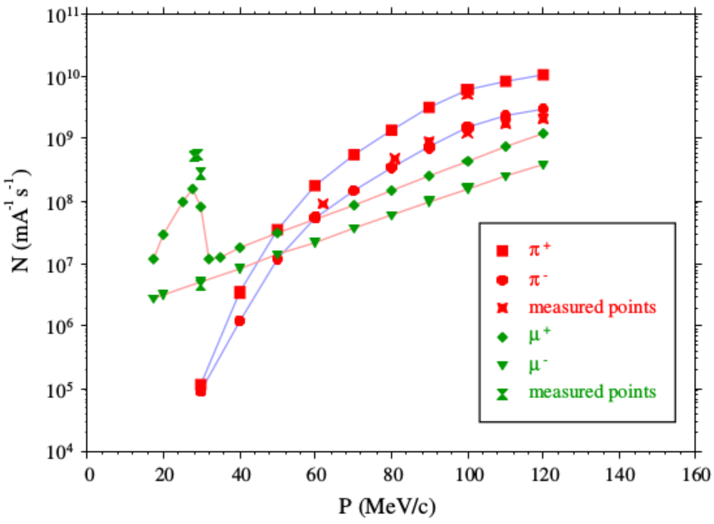

Figure 3.3: Pion and muon beam intensity at $\pi E5$ beamline

3.1.2 Beam Transport System

The muon beam from the πE5 beam channel is transported to the stopping target through a beam transport system which is shown in Figure 3.2. It is composed of a quadrupole triplet (Triplet I) an electrostatic separator (Wien filter), a second quadrupole triplet (Triplet II), and a beam transport solenoid (BTS) with a superconducting magnet.

Upstream of the transport system, the quantity of the positron contamination is eight times larger than that of positive muons. The Wien filter filters out the positron contamination with its horizontal magnetic field of 133 G and a vertical electric field of 195 kV in 19 cm gap of electrodes. Triplet I, II refocus the beam after a bending magnet and the Wien filter. Next, the beam is focused by a superconducting beam transport solenoid magnet (BTS, Figure 3.4). The main component of the BTS is a liquid helium cooled superconducting solenoid with 380 mm bore diameter and 2.63 m of length. A thin Mylar film degrader is placed at the center of BTS to maximize the stopping efficiency at the target. The thickness of the film is 300 μm. The degrader further reduces the muon momentum, thus optimizing the fraction of muons stopped in the thin target with less backgrounds. The resulting muon beam has an intensity of $3\times10^7\mu^+$/sec and is focused in an ellipsoidal spot on the target with transverse dimensions σ_x =9.5 mm and σ_y =10.2 mm at the COBRA center. At the stopping target, the beam has a round Gaussian profile and the polarization of muon is consistent with the expectation [73].

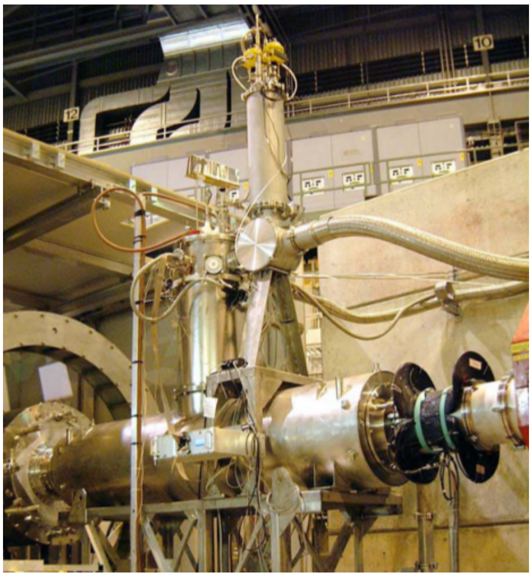

Figure 3.4: Beam Transport Solenoid

3.2 The MEG Apparatus

3.2.1 The target

The target purpose is to obtain high stopping power for muons and to reduce the background. Therefore, the target material and thickness are optimized to minimize scattering of positrons in the target and Annihilation In Flight (AIF). It is made of a layered film of polyethylene and polyester supported by a Rohacell frame of density 0.895 g/cm^3 (Figure 3.5:Left). The target dimension is 79.8 mm along the vertical axis and 200.5 mm along the longitudinal axis, with a thickness of 205 μm. The target is put at a slant angle of 20.5° with respect to the beam direction (Figure 3.5:Right). The angle has been optimized to increase the target thickness crossed by the muons (to obtained a stopping efficiency of $\sim$80%) and to reduce the thickness traversed by the decay positron by minimizing the multiple scattering and AIF of positron. The target has six holes, 1 cm diameter, and seven crosses (Figure 3.5: Left), used, respectively, to estimate the resolution of the vertex position reconstruction and to align the target.

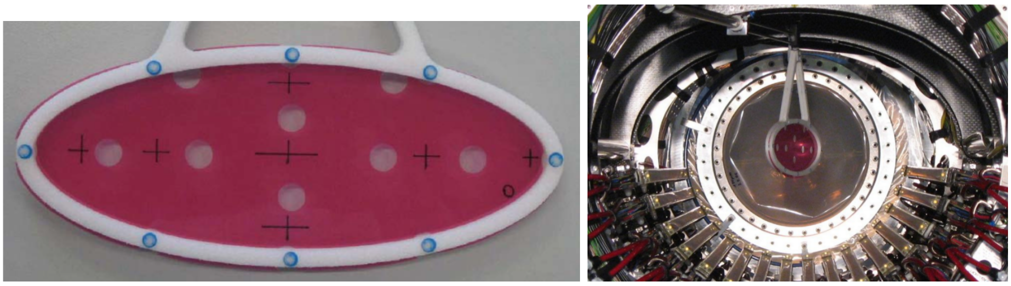

Figure 3.5: Left: Muon target. Right: The target at the center of the MEG apparatus.

3.2.2 MEG Detector

The MEG etectors [75] are a positron spectrometer and a photon detector. The positron spectrometer consists of a superconducting solenoid magnet called the COBRA (COnstant Bending RAdius) magnet, a system of 16 low-mass Drift CHamber (DCH), and a system of fast scintillating timing counters (TC). The DCH determines the positron position and the positron trajectory; the positron timing is determined by the TC. The photon detector consists of a LXe calorimeter. It is used to measure the photon energy, direction and time. A schematic layout of the MEG detector is shown in Figure 3.6. In this section, we describe the concept and design of each sub-detector. The global MEG coordinate system (x, y, z) is also drawn in Figure 3.6. The positive z direction is along the beam direction; the y-axis is the vertical axis pointing upward and the x-axis is the third axis that, together with y- and z-axes, forms a right-handed coordinate system. In terms of a spherical description, θ is the polar angle from the positive z direction and φ is the azimuthal angle from the positive x direction.

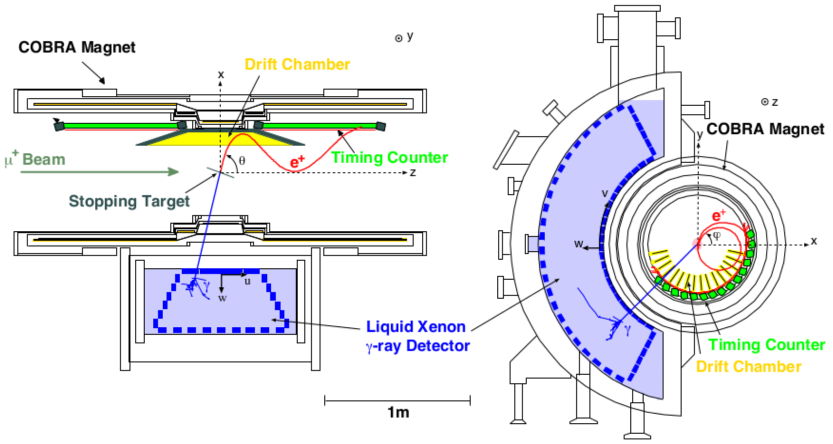

Figure 3.6: A schematic view of MEG detector with the coordinate system.

Photon detector

The MEG experiment requires an excellent determination of position, time and energy resolutions to minimize the number of accidental coincidences, which constitute the dominant background process. A LXe calorimeter [35] [94] is adopted as photon detector to fulfill those requirements. It is a scintillation detector filled with a 900 liter of liquid xenon. The LXe detector is shown in Figure 3.7: Right, with its C-shape structure fitting the outer radius of COBRA. The angular acceptance ranges, for photons from the target, are -60° $< \varphi <$60° and 60° $< \theta <$120° corresponding to a solide angle of 11%.

The photons interact with the LXe and generate scintillation light which is collected by 846 2-inch PMTs (Figure 3.7: Right) surrounding the calorimeter active volume. The detector measures the total energy released by the incident photon as well as the position and time of its first interaction point simultaneously. A cryostat (Figure 3.7: Left) was constructed with a vacuum layer to keep xenon in liquid phase. LXe has a fast response (45 ns), which enables precise timing resolution [6]. It also has a high light yield which is crucial for precise energy measurement. The absorption length for the scintillation photon (>100 cm) is much larger than the depth of the active LXe volume (38.5 cm, corresponding to 14 X_0[2], which enables high energy resolution with a large-sized detector.

The PMTs are immersed in the LXe to observe scintillation photons directly and they

---

[2] the radiation length X_0 is a characteristic of a material, and it is defined as the length over which the electron has left over 1/e of its original energy.

are installed on all six faces of the detector, with a different density for each face. Normal PMT windows made of glass are not transparent to the scintillation light of LXe (vacuum ultraviolet (VUV) light with a peak at 178 nm). Therefore the PMT model R9288 [54], developed by Hamamatsu Photonics for MEG, is equipped with a quartz window and a bialkalin photo-cathode sensitive to VUV photons.

The detector performance has a 1.7% energy resolution, ~5 mm position resolution and 67 ps timing resolution for a 55 MeV photon [78].

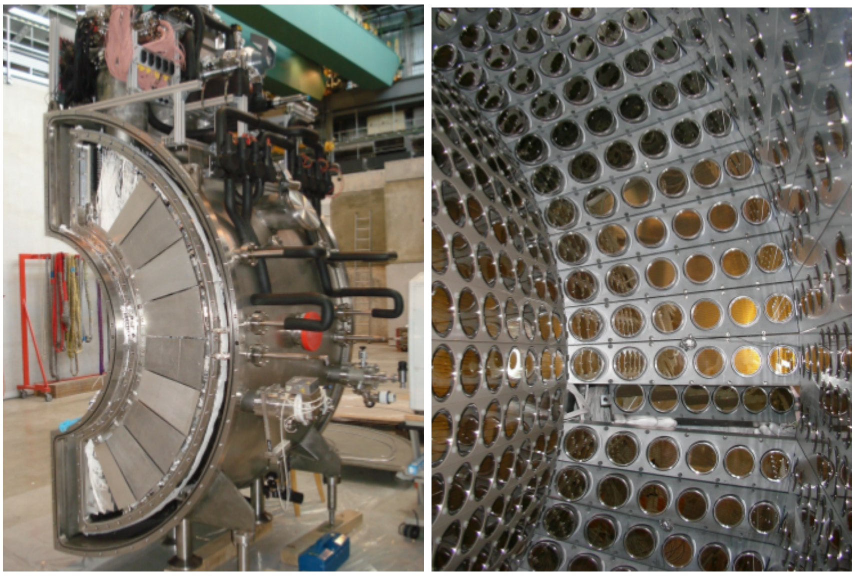

Figure 3.7: Left: The LXe detector. Right: Internal view of the LXe detector, showing the 846 PMTs mounted on the inside walls.

Positron spectrometer

Positrons are detected and measured in a spectrometer that is designed to be very light:

1. to avoid undesirable gamma ray generation from bremsstrahlung or AIF of positron;
2. to minimize the probability that a gamma ray interacts with some material before reaching gamma ray detector;
3. to minimize multiple scattering of positron.

The last point is crucial for the precise measurement of low-energy positron. In order to satisfy these requirements, the positron spectrometer is constituted by a superconducting magnet with a graded magnetic field, 16 drift chamber modules made up of low mass materials, to be used for the positron track reconstruction, and a timing counter for the impact time measurement of positrons. In this section, the details of each part are described.

Cobra magnet The COBRA magnet [30] consists of a main superconducting magnet and a pair of compensation coils; in Figure 3.8: Right is shown a picture of the magnet and in Figure 3.8: Left is shown a drawing with the different parts.

The compensations coils are necessary to minimize the residual magnetic field produced by the COBRA magnet near the LXe detector, because it can deteriorate the PMT performance. The main magnet is designed to provide a gradient field stronger at the center (z=0) $\sim$1.27 T, slowly decreasing as $|z|$ increases, to get a $\sim$0.49 T field at both ends as depicted in Figure 3.9. It is manufactured with 5 coils with different radii: a central coil, 2 gradient coils and 2 end coils. The coils are obtained by a multi filament Nb-Ti cable embedded in an aluminum matrix. This structure provides the necessary mechanical strength to the system reducing the need of external support. In this way it is possible to minimize the quantity of material the photons have to pass through, thus reducing the interaction probability of gamma rays before entering the calorimeter, indeed the central part of the magnet

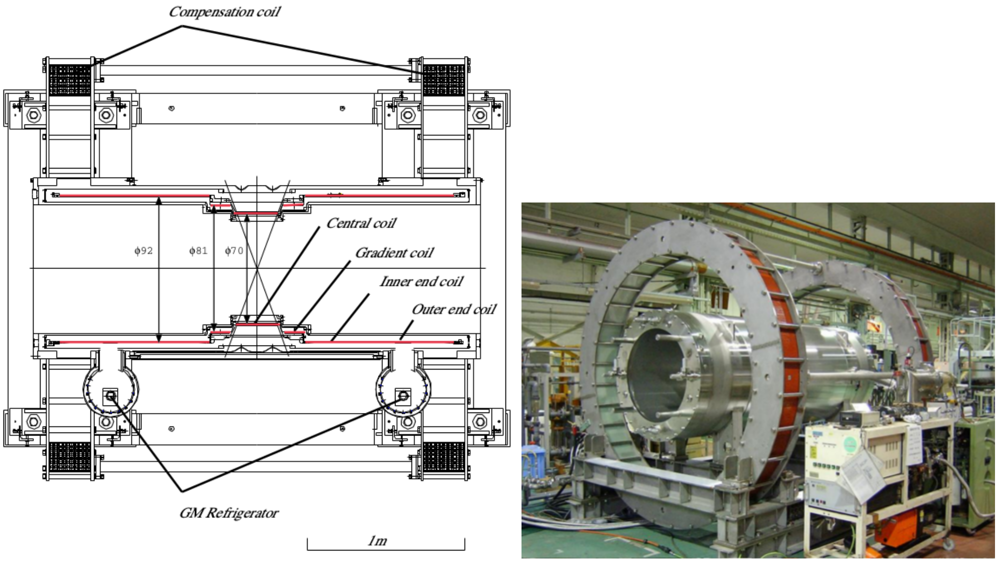

Figure 3.8: Left: Schematic of COBRA. Right: COBRA magnet.

wall is as thin as 0.197 X_0.

A magnetic solenoidal spectrometer of this kind has the advantage of radial momentum selection, therefore it is possible to set a detection momentum threshold for the tracking chamber (DCH) simply by placing them at a suitable chosen radius to cut out the low energy part of the positron from Michel decays. Pure solenoidal field does not match the MEG requirements in terms of tracking efficiency and momentum reconstruction, because:

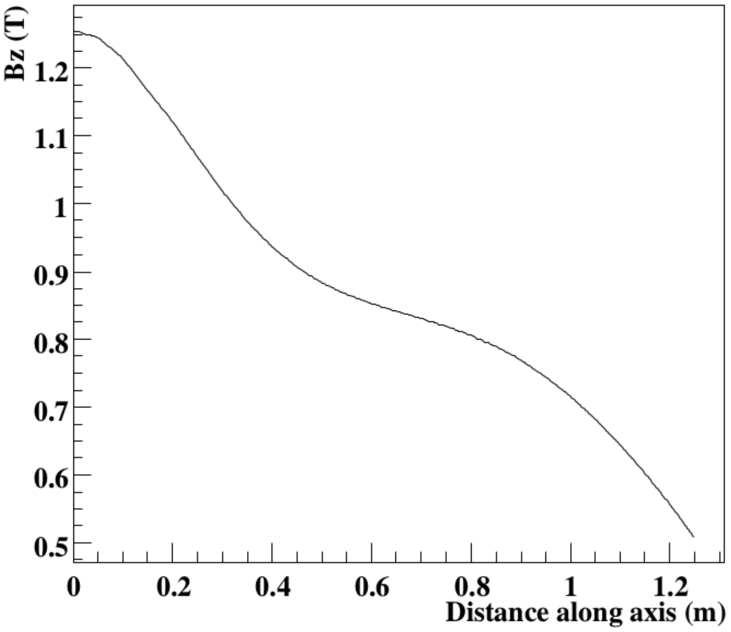

Figure 3.9: Profile of the magnetic field along the axis of the magnet.

- positrons emitted with an angle of about 90° with respect to beam axis presents a very small pitch of the helicoidal trajectory, thus jamming the detector with multiple turns with a consequent loss of efficiency (Figure 3.10:a);

- for a fixed value of outcoming momentum, the bending radius of the curved trajectory depends from the emission angle, resulting in a complication in track selection and momentum measurement (Figure 3.10:b).

Such complications can be avoided using a quasi-solenoidal field, with a proper gradient; in the case of COBRA magnet, the gradient is in the direction of the beam axis and also in the radial direction. This particular field map allows positrons emitted nearly perpendicular to the beam axis to make only 1-2 turns inside the chambers

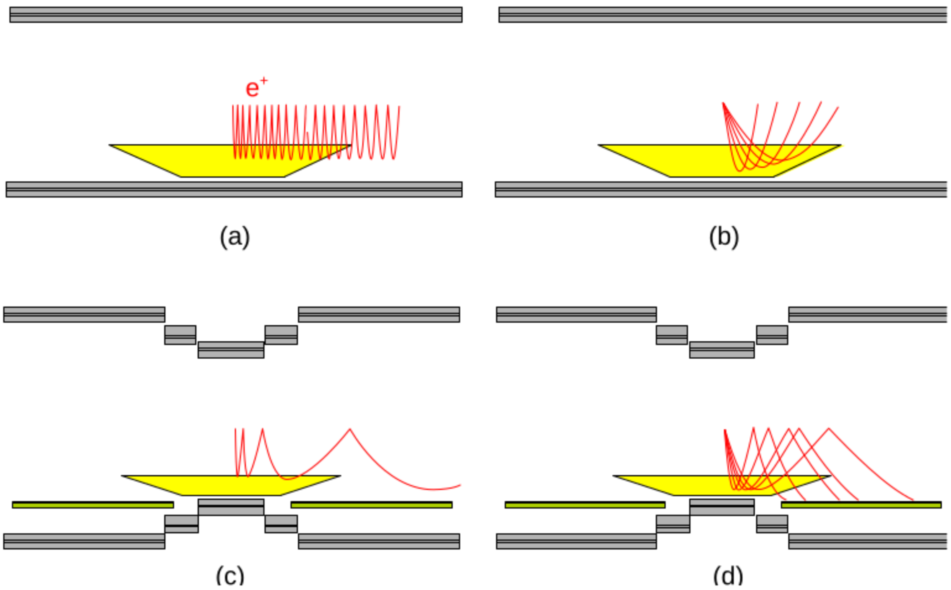

Figure 3.10: Conceptual illustrations of the COBRA spectrometer compared with one with a uniform magnetic field. (a) and (c) show trajectories of positrons emitted at 88°. The uniform field makes many turns inside the detector, whereas the gradient field sweeps the positron out of the detector much more quickly. (b) and (d) show trajectories of mono-energetic positrons emitted at various angles. In the uniform field, the bending radius depends on the emission angle, whereas it is independent in the gradient field.

(Figure 3.10:c). In addition, the gradient field is designed so that positrons with the same momentum follow trajectories with a constant bending radius independent of their emission angles (Figure 3.10:d); thus it is possible to tune the field intensity in such way that only positrons with energy near 52.8 MeV (signal positrons) can cross the DCH.

Timing counter The positron timing is measured by the TC detector [20, 98]. It consists of two sub-detectors; the outer layer counter and the inner layer one. The inner layer is stacked on top of the outer one. Each sub-detector is optimized for each specific task. The outer layer counter, called $\varphi-$counter, is designed to obtain a precise timing of the incident positron as well as a fast estimation of the positron emission angle φ. On the other hand, the inner layer counter, called z-counter, is optimized to give a reliable first level trigger, along with the determination of the impact point in z on the timing counter, which is related to the initial positron emission angle. The preliminary determination of the positron trajectory, provided by the timing counter, allows for the fast rejection of more than 95% of events with unmatched kinematic parameters.

The outer layer counter (Figure 3.11:Left), consists of 15 plastic scintillation bars at each end. A 2-inch fine-mesh Hamamatsu R5924[54] PMT is attached at both ends of each bar. The primary task for TC bars is to precisely measure the positron impact time and φ angle, though the z coordinate of a TC hit can be deduced by comparing the PMT timings at two ends of a bar. The timing resolution of the detector is determined through tracks hitting on multiple bars. The measured time resolutions of the bars is 60 ps, in accordance with expectations.

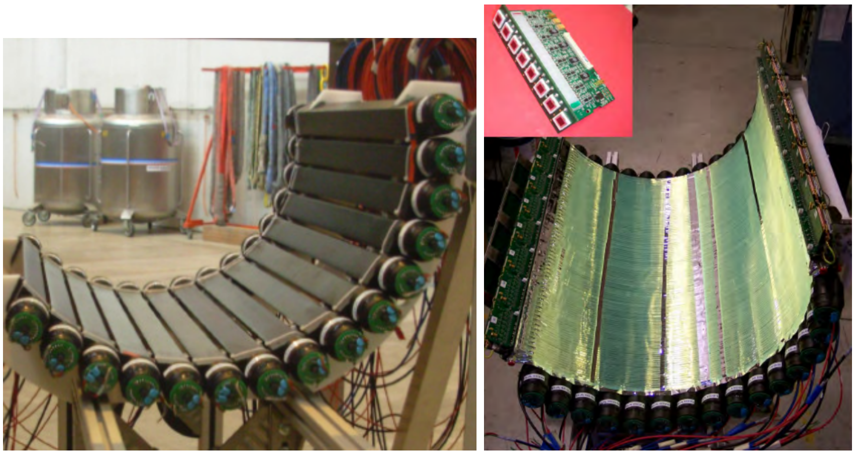

Figure 3.11: Left: a picture of the $\varphi-$counter before installation into the COBRA magnet volume. Right: the z-counter placed on top of the $\varphi-$counter before installation into the COBRA magnet.

The inner layer counter (Figure 3.11: Right) consists of 128 plastic curved scintillation fibers, each fiber is read out by HAMAMATSU S8664-55[54] silicon avalanche photo-diodes (APD). The primary task of the z-counter is to obtain a precise and fast measurement of the z position of the impact point, which is designed to be used in the trigger.

Drift chamber Positron tracks are measured by the DCH detector (Schematic of DCH in Figure 3.12 and picture Figure 3.5: Right) located inside of the COBRA magnet. It detects the ionization charge by the positron and it allows reconstruction of the trajectory, the emission angle and the vertex position. In order to reduce multiple scattering and background $\gamma-$ray generation, a low mass drift chamber system has been developed for the MEG experiment.

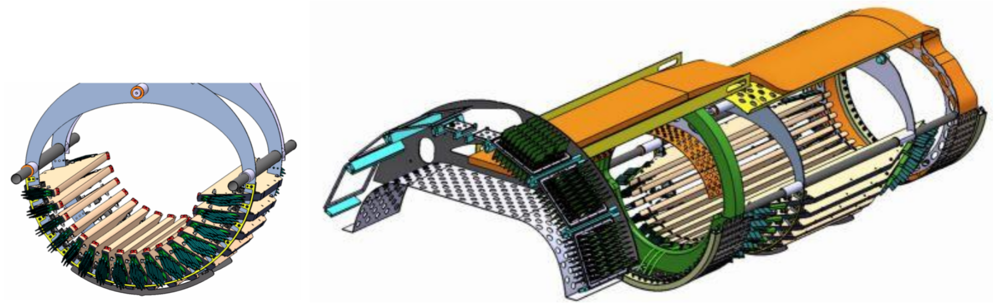

Figure 3.12: 3D design of Drift Chamber Mounting

The DCH system is installed in the center of the COBRA magnet. The COBRA magnet volume is filled with helium gas to reduce the amount of material in the spectrometer. The active gas inside the DCH modules is a mixture of 50% helium and 50% ethane (C_2H_6). It is adopted to reduce the multiple scattering [24, 95] and the energy loss of the positrons. Another advantage is fast drift velocity, which is important for the operation in the high-rate environment. At the nominal voltage (1850 V), the velocity is $\sim$4 cm/μs. DCH [55, 82] consists of 16 identical modules arranged radially in φ direction with a separation of 10.5° . The DCH modules cover the azimuthal region from 191.25° to 348.75° and the radial region from 19.3 cm to 27.9 cm, to have acceptance only for high momentum positrons (>40 MeV).
MEG signal positrons emitted from the target with $|\cos(\theta_e)|$ <0.35 and $|\phi_e|$ <60° are covered by the DCH geometry. A schematic layout of a single DCH module with geometrical information is shown in Figure 3.13. Each DCH module has two independent layers of anode wires sharing the same gas. The gap between layers is 3.0 mm (Figure 3.13). The layers, containing 9 drift cells each, are shifted by one-half cell to resolve left-right ambiguity. The drift cell consists of an anode wire, two cathode wires and two cathode pads. The cathodes pads are made of 12.5 μm thick ultra-thin polyimide (UPILEX) foil deposited with 250 nm aluminum, they are designed to be very thin to reduce the probability of positron multiple scattering.

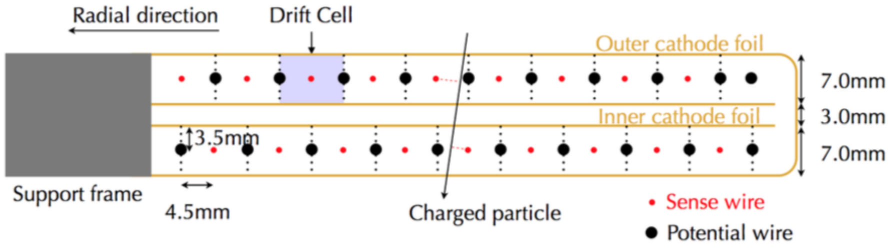

Figure 3.13: Intersectional view of DCH module

Table 3.3: Details of drift chamber design.

Part	Item	Value
Sense wire	material	Ni/Cr (80 : 20)
	diameter	$25\mu m$
	tension	$50g$
Potential wire	material	Be/Cu (2 : 98)
	diameter	$50\mu m$
	tension	$120g$
Cathode	foil	$12.5\mu m$ polyimide
	pad	$250nm$aluminum deposition
GAS	mixture	$He : C_6H_6(50 : 50)$
	pressure	$\sim 1atm$
HV	anode	$+1850V$
	cathode	ground

Cathode foils have "zig-zag" shaped 5.0 cm periodical pattern called "Vernier pattern" (the principle is depicted in Figure 3.14 and more details of the vernier method are described in [7, 8, 13]) to improve the z resolution.

The design information is summarized in the Table 3.3. The average radiation length of a module is 2.6×10^{-4} X_0, and total amount in a positron track is 2×10^{-3} X_0. The DCH reaches a resolution of σ_z =550 μm. The accuracy in the determination of the impact parameter on a wire, defined as single-hit resolution, is σ_r =210 μm in the core and σ_r =780 μm in the tail. The resolutions on the positron angle are: σ_{θ_e} ~9.4 mrad and σ_{φ_e} ~8.7 mrad. The momentum resolution of the drift chamber at 52.8 MeV is measured through the determination of the Michel spectrum endpoint, see Figure 3.15. The measured Michel spectrum is fitted by a function which includes theoretical Michel spectrum, scaled by the acceptance of the detector and convolved with a Gaussian resolution. The value obtained is $\sigma_{E_e} = 330$ keV.

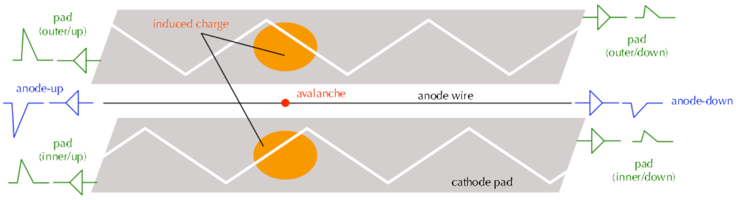

Figure 3.14: Schematic view and conceptual illustration of the Vernier pattern on the cathode pads

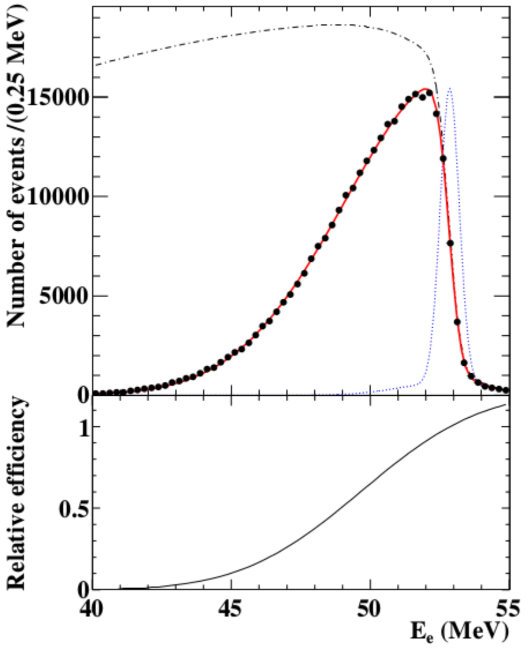

Figure 3.15: Michel positron energy spectrum used in the measurement of the drift chamber energy resolution.Dot-dashed line is the theoretical spectrum, blue dotted line is resolution function of the detector, and the acceptance function is drawn in bottom box (for all years). Figure from [62]

3.2.3 Trigger system

In order to collect the $\mu^+ \rightarrow e^+\gamma$ like events with high efficiency in a high background condition, the trigger system processes the signals coming from the fast detectors, namely the TC and the LXe calorimeter, keeping an acceptable acquisition rate. For physics data, the following observables are used in the online trigger selection:

- the E_γ and t_γ, reconstructed by the Xenon calorimeter;
- the t_{e+}, given by Timing Counter;
- the direction match between the reconstructed directions of the two particles.

The information on the positron momentum by the drift chambers is not used, being too slow because of the delay of the electrons drift time in the gas. The E_γ is estimated by summing all PMTs charges in LXe detector, each one weighted by its gain and quantum efficiency. The selected energy threshold for the MEG trigger is E_γ>45 MeV. The t_γ is extracted from the sampled waveform associated with the

PMT which shows the maximum signal, the t_{e^+} is evaluated using the mean of the times measured by the two PMTs of each TC bar. The position (angle) of γ ray is given as the position of the inner PMT which detected the largest number of photons. The e^+ reconstruction is done for first-hit TC bar. The combined informations about $\gamma - e^+$ direction is used to reject non collinear events.

The trigger system [47, 48, 49] is based on flash analog to digital converters (FADC) and FPGA. The input signals are sampled by FADCs and the digitized information is analyzed by FPGAs. The system is arranged in a tree structure on three layers with two different types of boards. The first layer consists of the Type1 boards compliant with the 6U VME standard. The two remaining trigger layers consist of a second type of boards (Type2) compliant with the 9U VME standard. The second layer determines trigger conditions of sub-systems, and finally the third layer makes a trigger decision. In addition, an ancillary system was developed to provide the clock and the synchronization signals to all other boards. A schematic view of the trigger system is shown in Figure 3.16.

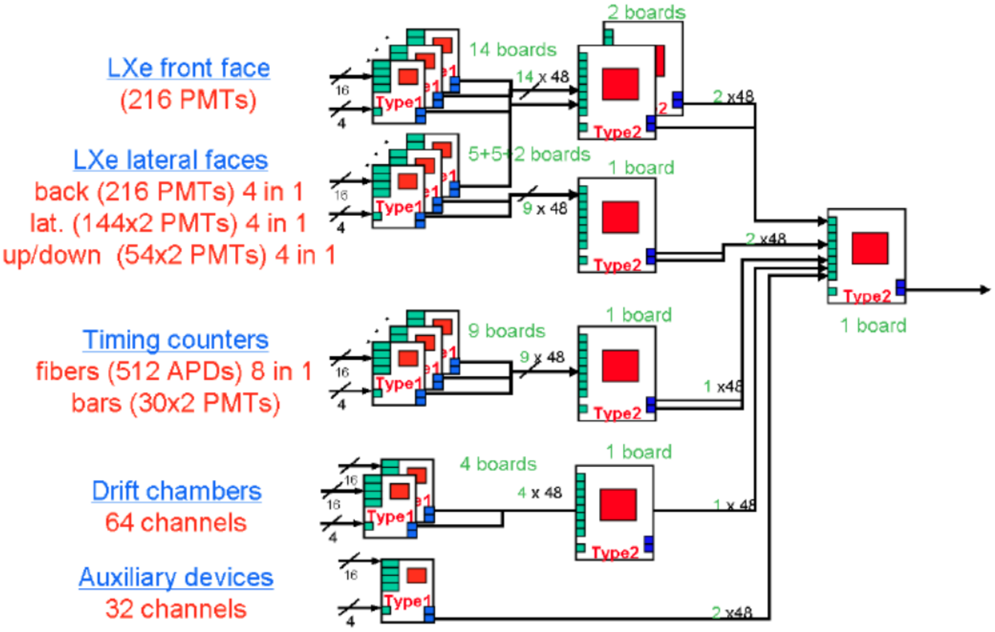

Figure 3.16: Layout of the trigger system.

3.2.4 The data acquisition system

The data acquisition system (DAQ) for the MEG experiment requires a high precision and high rate of operation. For this reason, the signals from all detectors are digitized by a sampling chip developed at the PSI and based on the DRS [93]. The chip is housed on a custom VME board and read out by a commercial 12 bit ADC and controlled by FPGAs, allowing for easy modification of the DAQ algorithms. Since the LXe and TC detectors require precise time measurements, 1.6 GHz sampling frequency was chosen. In the DCH, 0.8 GHz frequency was chosen because it needs less timing requirements than those for other detectors.

The crates containing the VME boards are read out by a cluster of dedicated PCs for online waveform processing. The Maximum Integrated Data Acquisition System (MIDAS) frameworks provides not only the control of front-end processes but also the logging system, the online database system for the parameters of DAQ and trigger, the slow control system, the alarm system, the history monitoring system, and web interfaces.

3.2.5 Calibration Apparatus

The stability of the working points of the detectors is periodically checked through calibrations, aiming at monitoring the resolution changes on the various kinematic variables, the absolute energy scales and the position of the zero for time and direction. For this purpose a rich set of calibration procedures has been developed [84]. The xenon detector is tested over a wide energy range with:

- $\alpha-$sources deposited on thin wires are placed inside the detector, and are used to probe the response at low energy (5.5 MeV). In addition they permit daily monitoring of the PMT quantum efficiencies and the liquid xenon optical properties.

- Intermediate energies are probed through nuclear reactions induced by 400-700 keV protons from a Cockcroft-Walton accelerator on a $Li_2B_4O_7$ target.

- The high energy range is probed through π^0 decays from π^- charge exchange of protons in a liquid H_2 target.

Drift chambers operation is monitored through coherent Mott scattering of positrons on the carbon atoms of the polyethylene target. A positron beam is easily obtained from the positron component of the MEG beam by changing the working point of the electrostatic separator. This method provides an additional measurement of the angular and momentum resolution, a measurement of the spectrometer acceptance and an independent check of the spectrometer alignment. Mott scattered positrons have an average momentum close to the incident momentum of 53 MeV/c, with a measured sigma of 450 keV/c that includes also the spread of the incident positron energy.

3.2.6 Data Analiysis

The MEG experiment sets the most stringent constrain on CLFV, having established the upper limit of $\mathcal{B}.\mathcal{R}.(\mu^+ \to e^+\gamma) = 4.2{\times}10^{-13}$@90%CL [74].
The five key observables to distinguish possible $\mu^+ \to e^+\gamma$ candidates from background are:

- the measured energy of the final state positron (E_{e^+}) and photon (E_γ);
- the measured relative time between the positron and the photon ($\mathrm{t}_{e^+\gamma}$);
- the relative polar ($\theta_{e^+\gamma}$) and azimuthal ($\phi_{e^+\gamma}$) angles between the measured emission directions of the outgoing positron and photon.

These five variables are aggregated in proper vectors for each event e_i, and the distribution of the collected events is studied in terms of this vector. The analysis is based on a “blind analysis” technique in order to avoid any possible bias in results, and it is made by means of a maximum likelihood fit performed on the spectra of the kinematic variables that define the $\mu^+ \longrightarrow e^+\gamma$ signal.

3.2.7 Data sets

Data were accumulated intermittently in the years 2008-2013 (see Figure 3.17). The data accumulated in 2008 were presented in [70], but the quality of those data was degraded and therefore they are not considered in the last full dataset analysis [74]. In total, $7.5{\times}10^{14}$ muons were stopped on target in 2009-2013. The analysis based on the 3.6×10^{14} muons stopped on target in 2009-2011 was published in [71]. The data from the remaining 2.3×10^{14} muons, stopped on target in 2012, and from 1.6×10^{14} muons, stopped on target in 2013, are included in last analysis [74], completing the full dataset.

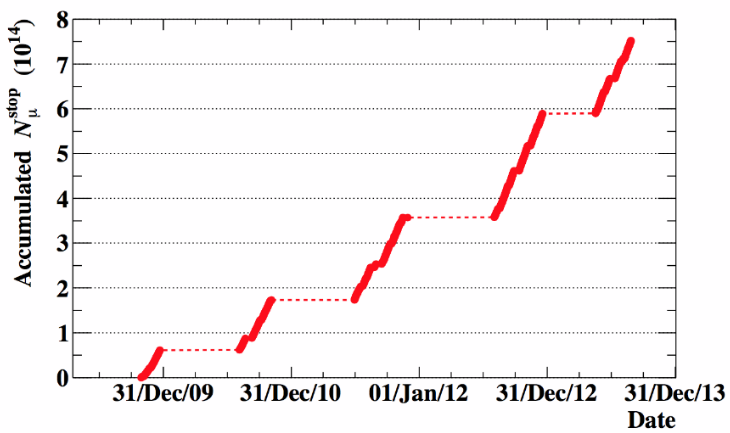

Figure 3.17: Accumulated number of stopped muons in the MEG polyethylene target as a function of the years.

3.2.8 Pre-selection and blinding box

At the first stage of the data processing, a data reduction (pre-selection) is performed by selecting events with conservative criteria that require the photon time detector signal to be close to that of a timing counter hit, and at least one track to be detected by the drift chamber system. The pre-selection definition is as follows.

- $-6.875n < t_\gamma - t_{TC}$ <4.4 ns
- $|t_{trackDC} - t_{TC}|$ <50 ns

The window is determined so wide that we do not lose good events. The events which satisfy both criteria for at least one positron track, remain in later analysis. The pre-selected events falling into a pre-defined window (blinding-box) of the plane defined by $|t_{\gamma e^+}|$ <1 ns and 48.0< E_γ <58.0 MeV, represented in figure 3.18, are hidden and written in a separate data stream. The use of a blind analysis is a consolidate technique in particle physics, especially when one has the need to estimate accurately systematic errors for the measurement, without biases induced by the researcher himself.

The regions out of the blind box are called sidebands (Figure 3.18), these are used to determine the parameters that are necessary for the physics analysis. In particular, one can identify two kinds of side-bands:

- the time side-bands, defined by $|\Delta t_{e^+\gamma}|$ ≥1 ns;
- the energy side bands, defined by 44.0<E_γ<48.0 MeV.

Both side-bands are used for background level estimation: the time side-bands are used to study the accidental events spectra, particularly for E_γ, while the energy side-band is used for evaluating time resolution and offsets between the the LXe calorimeter and the TC and for estimating the number of Radiative Muon Decay (RMD) in the analysis region. The RMD number [73] is used to determine the normalization.

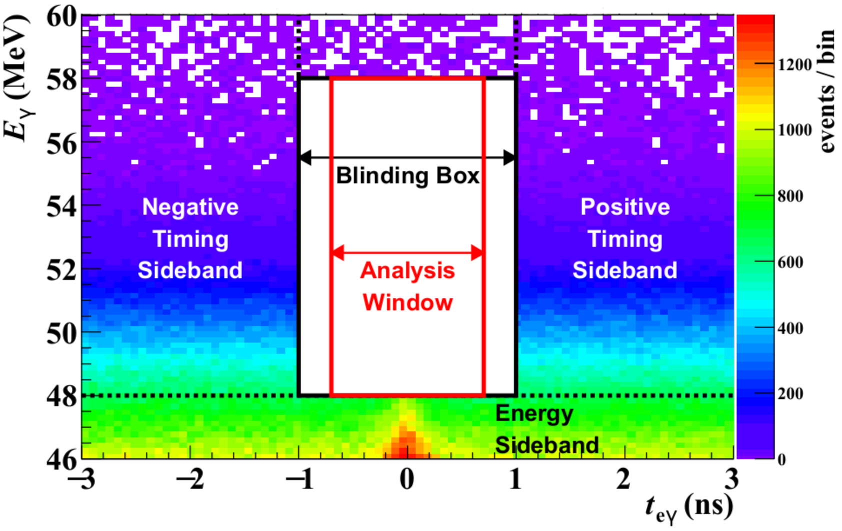

Figure 3.18: The MEG blinding box and side-band.

3.2.9 Probability density function

In order to extract the number of signals (N_{sig}) , radiative (N_{RMD}) and accidental background (N_{ACC}) a maximization of a likelihood function is performed. The likelihood function is built starting from the probability density function (PDF) that describes each kinematic observable. In the following section, we will briefly describe each PDF

Signal PDF The signal PDF S can be factorized as the product of the statistical independent PDFs evaluated for each observable:

$$S(E_{\gamma}, E_{e^+}, \theta_{e^+\gamma}, \phi_{e^+\gamma}, t_{e^+\gamma}) = S_1(E_{\gamma})S_2(E_{e^+})S_3(\theta_{e^+\gamma})S_4(\phi_{e^+\gamma})S_5(t_{e^+\gamma})$$

where:

- S_1(E$_{\gamma}$): The γ energy PDF is defined by the Lxe calorimeter response function for E_{γ} measured in dedicated π^0 runs (Charge EXchange reaction (CEX) calibration).

- S_2(E$_{e+}$): The positron energy PDF is evaluated by fitting the kinematical edge of the measured Michel positron energy spectrum at 52.8 MeV.

- $S_3(\theta_{e^+\gamma})$ and $S_4(\phi_{e^+\gamma})$:The angular PDFs are formed combining the contributions of positron emission angles, muon decay vertex reconstruction and photon position resolution in the LXe detector. The resolution of the angles between the two particles is evaluated by combining the angular resolution and the vertex position resolution in the positron detector and the position resolution in the photon detector.

- $S_5(t_{e^+\gamma})$: The time PDF depends on the e$^+$ and γ timing measured by the detector, it is evaluated with the RMD peak by fitting the distribution of the relative timing in E_{γ} sideband data with Gaussian functions and a constant.

RMD PDF The PDF for the RMD event is written as:

$$R(E_{\gamma}, E_{e^+}, \theta_{e^+\gamma}, \phi_{e^+\gamma}, t_{e^+\gamma}) = R_1(E_{\gamma}, E_{e^+}, \theta_{e^+\gamma}, \phi_{e^+\gamma})R_2(t_{e^+\gamma})$$

where $R_2(t_{e^+\gamma})$ is defined as the same function as for the $t_{e^+\gamma}$ signal PDF, while $R_1(E_{\gamma}, E_{e^+}, \theta_{e^+\gamma}, \phi_{e^+\gamma})$ is obtained from the theoretical RMD spectrum convoluted with the detectors resolutions.

Accidental background PDF The accidental background is given by a e^+ and γ in time and spatial coincidence, coming from uncorrelated events. Thus there are no correlations between each observables, and the PDF can be defined as the product of statistically independent PDFs for the five observables:

$$B(E_\gamma, E_{e^+}, \theta_{e^+\gamma}, \phi_{e^+\gamma}, t_{e^+\gamma}) = B_1(E_\gamma)B_2(E_{e^+})B_3(\theta_{e^+\gamma})B_4(\phi_{e^+\gamma})B_5(t_{e^+\gamma})$$

where:

- $B_1(E_\gamma)$ is obtained by fitting the background spectrum in the $t_{e^+\gamma}$ sidebands.
- $B_2(E_{e^+})$ is obtained by fitting the Michel spectrum, and it is common to all the events in the analysis window.
- $B_3(\theta_{e^+\gamma})$ and $B_4(\phi_{e^+\gamma})$ are extracted from all the side-bands data.
- $B_5(t_{e^+\gamma})$ is described by a flat distribution, because of the accidental nature of this kind of background.

3.2.10 Likelihood analysis

The blinding-box is opened after completing the optimization of the analysis algorithms and the background study. The number of $\mu^+ \to e^+\gamma$ (N_{sig}), RMD (N_{RMD}) and accidental background (N_{ACC}) events are extracted by means of a maximum likelihood fit in the window. It is slightly larger with respect to the signal box. The width of the windows is chosen from 5 to 20 times of the resolutions, in order not to lose signal events, and not to contain so many background events.

An extended likelihood function $\mathcal{L}$ is constructed as:

$$\mathcal{L}(N_{sig}, N_{RMD}, N_{ACC}) = \frac{N_{obs}^{N} e^{-N}}{N_{obs}!} e^{-\frac{(N_{RMD}-\mu_{RMD})^2}{2\sigma^2_{RMD}}} e^{-\frac{(N_{ACC}-\mu_{ACC})^2}{2\sigma^2_{ACC}}} \qquad (3.1)$$

$$\times \prod_{i=1}^{N_{obs}} \left[\frac{N_{sig}}{N} S + \frac{N_{RMD}}{N} R + \frac{N_{BG}}{N} B \right]$$

where μ_x and σ_x (x= N_{RMD} or N_{ACC}) are respectively the average and standard deviation of a Gaussian function estimated in the sidebands, N_{obs} is the number of events found in the analysis region, $N = N_{sig} + N_{RMD} + N_{ACC}$, S,R and B are their respective probability density functions. The maximum likelihood fitting was performed on the data in the physiscs analysis window and it is shown in Figure 3.19 for the 2009-2013 complete dataset.

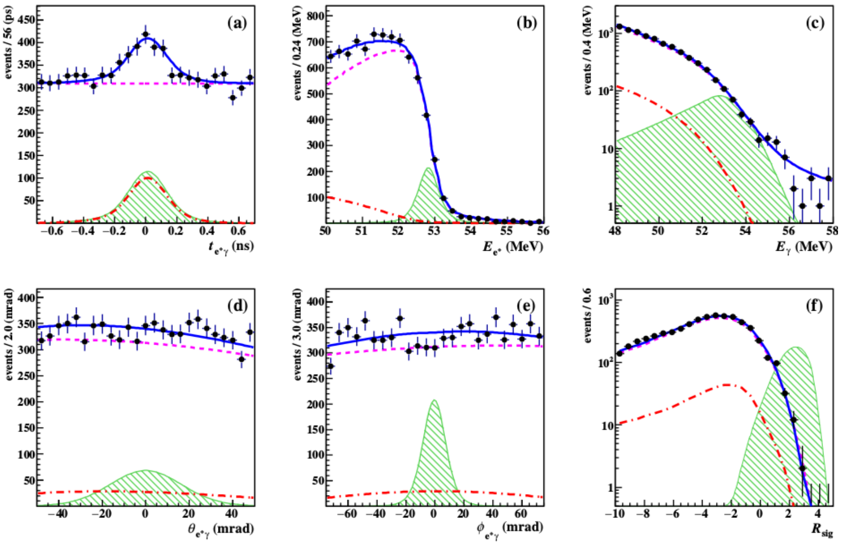

Figure 3.19: Likelihood fit result for 2009-2013 combined dataset. Data (Black dots) are shown with the projections of the the five main observables ($(a) : t_{e^+\gamma}, (b) : E_{e^+}, (c) : E_\gamma, (d) : \theta_{e^+\gamma}, (e) : \phi_{e^+\gamma}$) and variable control R_{sig}.Blue: Total PDF. Magenta: accidental background. Red: RMD background. Green: Expected signal for a BR equal to 100 times the upper limit.

3.2.11 Final results

For the determination of $\mathcal{B}.\mathcal{R}.(\mu^+ \to e^+\gamma)$, the number of detected events is normalized by using both the number of Michel positrons and the measured number of RMD events. The C.L. computation is based on a frequentistic method [45] with a profile likelihood-ratio ordering.

In 2016 the MEG collaboration published a new constraint on the $\mathcal{B}.\mathcal{R}.(\mu^+ \to e^+\gamma)$ <4.2×10^{-13}@90%CL[74], obtained with ≈7.5×10^{14} muons stopped on target.

Table 3.4: Comparison between MEG design and obtained resolution with the upgrade detector performance. Values taken from [72].

Variable	Foreseen MEG	Obtained MEG	MEG II
$\triangle E_\gamma(\%)$	1.2	1.7	1.0
$\triangle t_\gamma(ps)$	43	67	≤67
$\triangle\gamma position(mm)$	4-6	4-6	∼2
$\triangle P_e(keV)$	200	306	≤130
$e^+angle(mrad)$	$5(\varphi), 5(\theta)$	$8.7(\varphi), 9.4(\theta)$	$\leq 4(\varphi), \leq 5(\theta)$
$\triangle t_{e^+}(ps)$	50	107	30
$\triangle E_\gamma(\%)$	1.2	1.7	1.0
$\triangle t_{e\gamma}(ps)$	65	122	80

In Figure 3.20 the event distribution for data is displayed in the signal region; the variables of interest are the positron energy E$_{e+}$, the photon energy E$_\gamma$, the relative time t$_{e+\gamma}$ and the cosine of the angle between the reconstructed trajectories of the particles cos($\theta_{e+\gamma}$). Accidental background events are seen close to the signal region, displayed as confidence intervals at 1σ, 1.64σ, 2σ (the curves on the plots). The background events seen close to the signal region do not allow to consider MEG as a background-free experiment any more. The resulting sensitivity would increase only with the square root of the data taking time. Foreseen and measured resolutions and efficiencies of the MEG detector are shown in Table 3.4 if the calorimeter almost fulfills the predicted performance, for the positron spectrometer the obtained resolutions are worse than expected, in particular for the drift chambers.

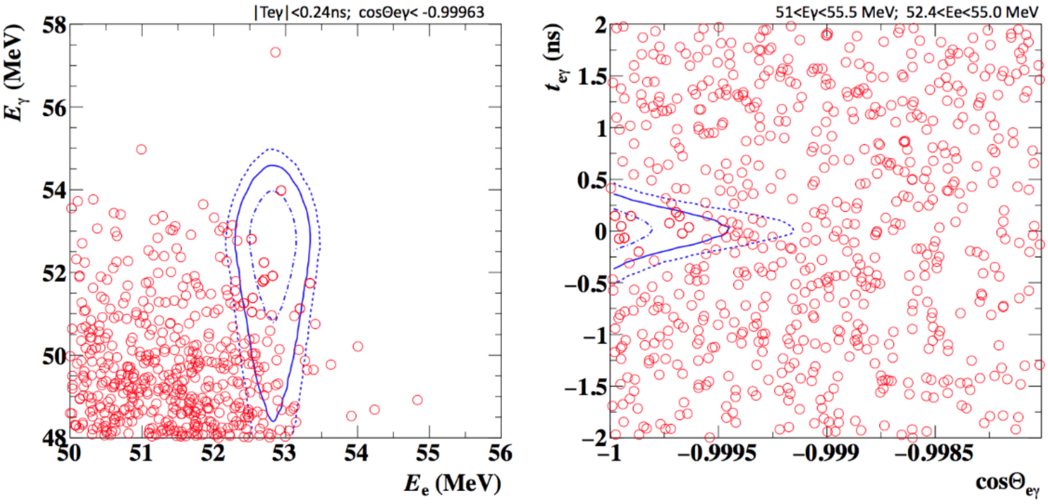

Figure 3.20: Event distributions observed in the analysis window.

3.3 The MEG II Apparatus

3.3.1 The reasons for the upgrade

It is clear that the MEG experiment has practically reached its limit of sensitivity, limited by the resolutions on the kinematic variables of the decay products (Paragraph 3.2.11). The background events are seen close to the signal region and thus the sensitivity does not scale linearly with the collected data.

As seen in the Chapter 1 , the exploration of the SUSY parameter space is not completed yet, in particular SUSY-GUT theories favor the $\mu \rightarrow e\gamma$ channel when compared to other sources of cLFV, these theories predict a B.R. of 10^{-14}– 10^{-11}. The idea is to exploit at its best the capabilities of the already existing MEG apparatus and to take advantage of the knowledge acquired during these years by the MEG collaboration, in order to realize an upgraded experiment. From Table 3.4 , it can be noted that the photon detector and timing counter almost met the design requirement, but the resolutions of the positron spectrometer are substantially worse than the design values, which in turn impacts the e-γ timing measurements. The tracker efficiency is badly affected by the positioning of front-end electronics and mechanical supports which intercept a large fraction of positrons in their path to the timing counter. Additionally, the thin segmented cathode foils used to determine the hit position along the z-coordinate suffer from having low amplitude signals (only a few mV) and being thus vulnerable to noise. Their use in high radiation environments also leads to the formation of deposits which give rise to discharges. As far as the LXe detector, it suffers from degraded energy reconstruction close to the inner face, because of strong non-uniformities in response due to the low granularity of the PMT ś.

Therefore the MEG upgrade, MEG II [72], seeks to resolve the difficulties encountered in MEG with a series of improvements which include new detectors with better acceptances, efficiencies and performances:

1. a higher muon stopping rate;

2. a thinner target with lower contribution of multiple scattering on the positron and photon trajectories;
3. a new positron tracker, with a reduced radiation length, a higher resolution and a higher tracking efficiency;
4. a better coupling between positron tracker and timing counter;
5. a new timing counter, with higher granularity and resolutions;
6. extended LXe calorimeter acceptance and efficiency to achieve a better photon resolution;
7. improvement of the calorimeter performances for the photons converting close to the inner face;

According to such modifications, the trigger system and DAQ will be improved as well, in order to match their performances with those of the new detectors. Figure 3.21 shows a schematic overview of the previous MEG experiment compared to the MEG II while Figure 3.22 shows the design of the MEG II detector apparatus and in Table 3.4 is a list of the expected MEG II resolutions compared to the original MEG apparatus.

3.3.2 Beam and target

The MEG experiment had to reduce the available muon beam intensity, in order to achieve a muon stopping rate of 3×10^7 Hz and thus guarantee a stable operation of detectors and minimize accidental background. An increase in the muon rate, at the maximum of the PSI muon beam intensity (7×10^7 Hz), must be necessarily accompanied with the improvement of the experimental resolutions, in order to keep accidental background low. Target thickness establishes the intrinsic resolution on the determination of the relative angle between photon and positron because of multiple scattering. The reduction of multiple scattering can be achieved by reducing

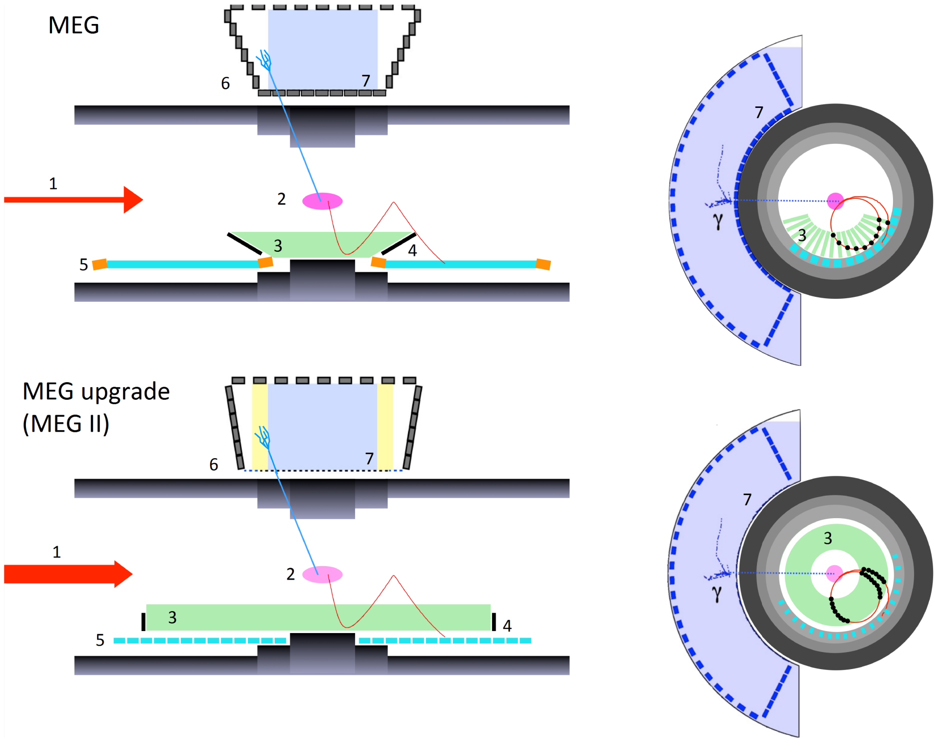

Figure 3.21: The main components of the MEG experiment and their corresponding upgraded version. The numbers correspond to the list in the text. Figure from [72]

the target thickness, but target thickness is related to the muon momentum: the more energetic the muon is, thicker is the target where the muon is completely stopped. The muon beam momentum is currently selected by the magnetic optics of the πE5 channel, which for MEG transmits only surface muons. In principle it is possible to select muons in a momentum window centered at about 26 MeV/c (“subsurface muons”), so that the required thickness of the target can be lower. Figure 3.23 shows the measured momentum spectrum of muons emerging from the graphite target by the πE5 beam line. In MEG II, the two possible options muon beam and stopping target are: a surface muon beam with a 140 μm target thickness and an angle of 15°; a sub-surface muon beam with a 160 μm target thickness and an angle of 15°. These scenarios are under study.

3.3.3 The MEG II Detector

In this section we will describe the upgraded detectors for the MEG II experiment.

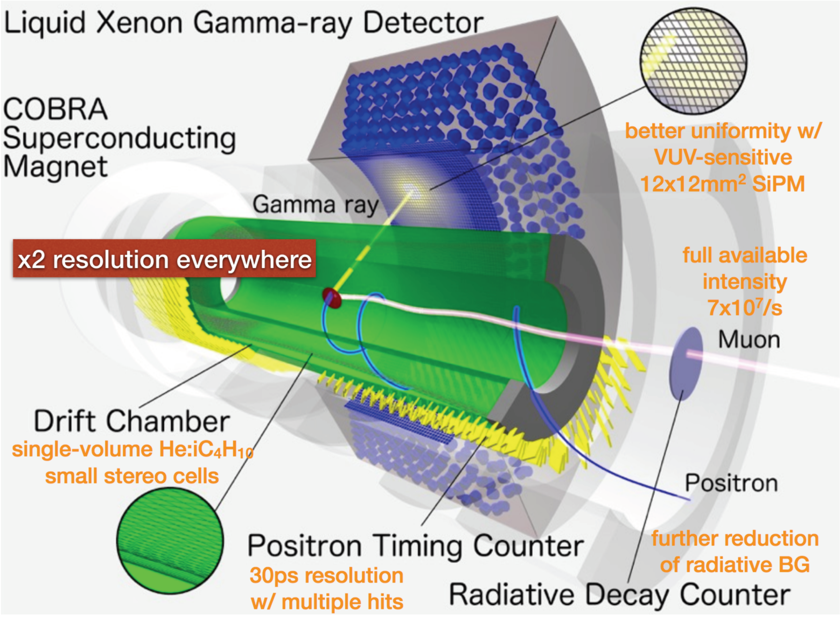

Figure 3.22: MEG II experimental apparatus with with improvements.

Photon detector

LXe calorimeter [83, 72] has a resolution dependent on the depth of the γ-conversion: reconstruction capabilities are worse for photons converting close to the entrance face and at the edge of the acceptance. This is due to the non-homogeneous 2" PMTs coverage of the entrance face, see Figure 3.24. In MEG II, the solution is increasing the detector granularity by replacing the 246 2” PMTs on the entrance face, with 4092 12×12 mm^2 Multi-Pixel Photon Counters (MPPCs), see Figure 3.24. They should be sensitive to the vacuum ultraviolet as the photomultipliers and have fast responses. The MEG II collaboration and Hamamatsu Photonics have developed MPPCs which have a high photon detection efficiency ($\sim$20%) for liquid xenon scintillation light and a fast decay time ($\sim$50 nsec), for more information see [31].

The layout of the lateral faces will be modified as well in order to avoid shadow areas, which result in a reduced acceptance. The proposed structure is visible in Figure 3.25, where the wider acceptance region is highlighted.

Monte Carlo simulations (Figure 3.26) show that, in the new configuration, the resolutions are improved for both shallow and deep events, mainly because of the more uniform photon-collection efficiency. The returned values of the resolutions are 1.1% for shallow events and 1.0% for deep events. The smaller size of the photo-sensors on the entrance face can also bring an improvement on the timing

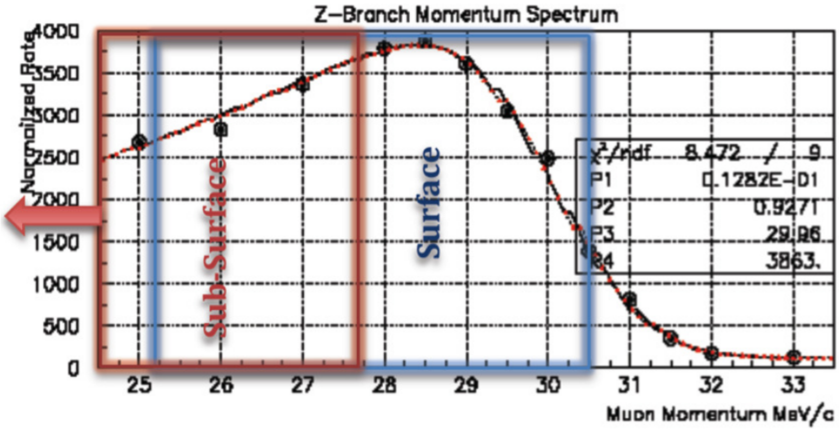

Figure 3.23: The measured muon momentum spectrum from the πE5 channel. The red curve is a fit to the data of a theoretical p$^{3.5}$ distribution folded with a Gaussian resolution function corresponding to the momentum-byte plus a constant cloud-muon background. The blue and red boxes show the full momentum-byte for surface and sub-surface muons respectively. Figure from [72]

resolution of the calorimeter, which is evaluated in simulations as ∼84 ps. The Photon Detection Efficiency is estimated to be improved by ∼9%. The modification of the PMTs layout on the lateral faces extends the LXe calorimeter acceptance by ∼10% on each side.

Positron spectrometer

The new positron spectrometer consists of a low mass cylindrical drift chamber with stereo wires, and a pixelated timing counter. In the new configuration positrons traverse less material along their path and the capabilities of matching the information from the two detectors are powered. They are both designed to operate in COBRA. In the following section will briefly describe both detector.

Timing counter The MEG TC achieved the desired performances during beam tests with a resolution of 40 ps, but during the running phase, the performance worsened with a resolution of 65 ps. This deterioration is due to the behavior of TC PMTs in the COBRA magnetic field. Magnetic fields affect PMTs by increasing the transit time spread and reducing gain.
The TC upgrade consists in a new pixelated timing counter, more information in [18], composed of two arrays of ∼128 small plastic scintillator plates with silicon photomultipliers (SiPMs) read-out, as shown in Figure 3.27: the single plate itself

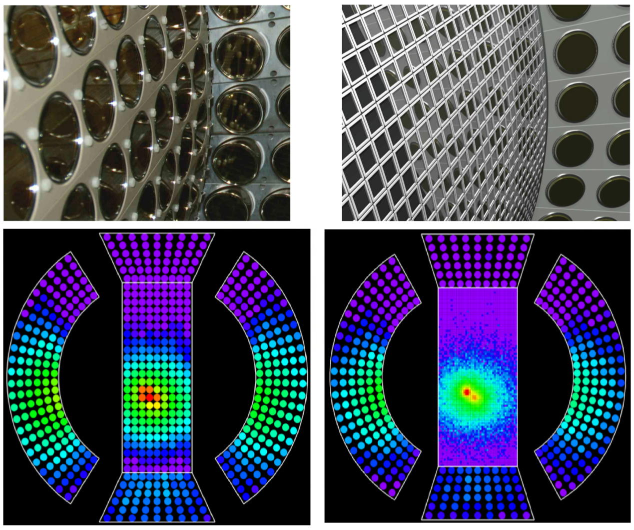

Figure 3.24: Top: interior view of the LXe calorimeter before (on the left) and after the detector upgrade (on the right) for MEG-II. Figure from [72] Bottom: Scintillation light distribution in the LXe calorimeter equipped with PMTs on the entrance face (on the left) and with the MPPCs (on the right).

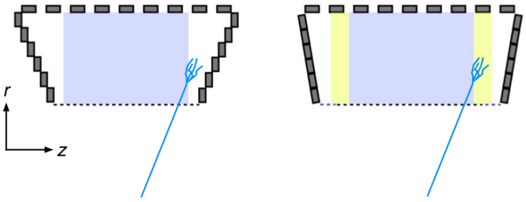

Figure 3.25: Acceptance increase of the upgraded calorimeter due to the changes in the lateral faces. The upgraded fiducial volume is highlighted. Figure from [72].

offers a good time resolution, but an even more precise estimation of the positron impact time can be obtained by averaging on the times of those hit pixels; moreover, the pile-up probability is quite low even at high rates. The single plate dimension is $30 \times 90 \times 5$ mm^3 and is connected to 4 SiPMs, one for each side, whose task is to collect light and send the signal to the DRS.

Preliminary performances show a resolution of about 55 ps using the hit on a single pixel, with the possibility to go down 30-40 ps with multiple hits measurements.

Drift chamber The new positron tracker is a single cylindrical drift chamber (CDCH) with its axis parallel to the muon beam axis. The biggest advantage of this new CDCH is that positrons with a momentum greater than 45 MeV/c will encounter a very small amount of material before reaching the TC. CDCH is composed of 10 layers of drift cells at alternating stereo angles. Each layer has 192 square cells with ratio of field wires to sense wires equal to 5:1 to ensure the proper electrostatic

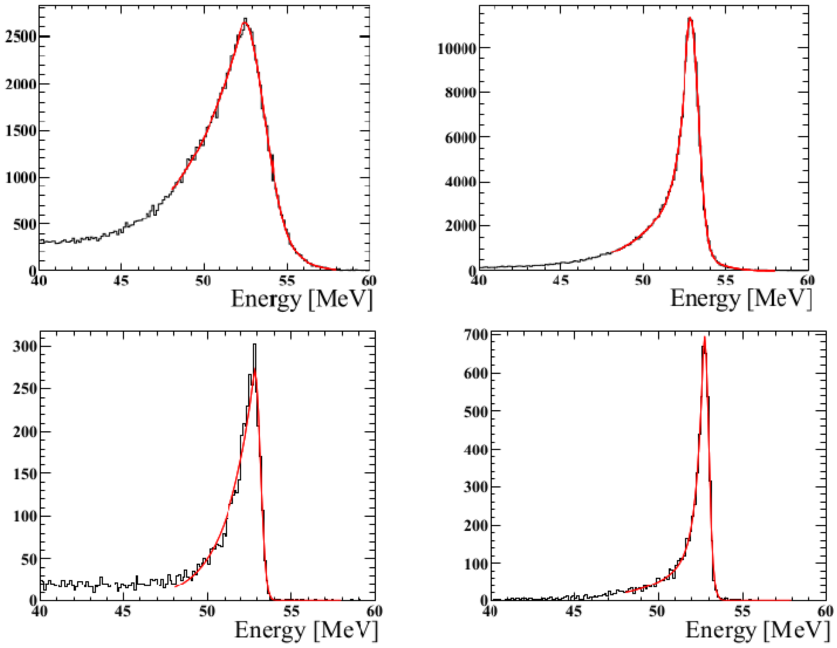

Figure 3.26: Monte Carlo simulation of the energy response of the LXe calorimeter in MEG (the upper plots) and MEG II (the lower plots), for shallow and deep event. Figure from [72].

configuration. The cell size varies linearly between 6.7 mm, at the inner radius, and 8.7 mm at the outer radius. The alternating stereo angles vary from 5.8° to 8.5°. The anodes are 20 μm diameter tungsten wires, while the cathode wires are 40-50 μm aluminum. The chamber is filled with a 85:15 He/iC_4H_{10} mixture, chosen once again for its low mass. The mechanics of the CDCH and the performance will be presented in details in the next chapters.

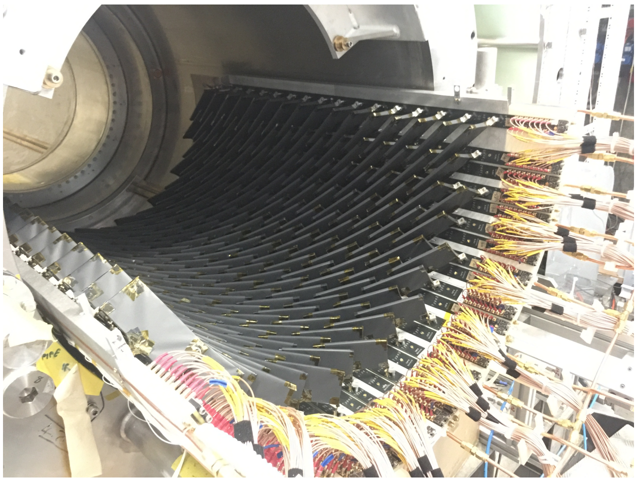

Figure 3.27: Downstream pixelated timing counter in the COBRA.

3.3.4 Radiative Decay Counter

Radiative Decay Counter (RDC) is an additional detector to be newly installed in MEG II ()for information see [81, 60]). It is capable of identifying a fraction of the RMD decays with the γ-ray energy close to its kinematical limit which are the dominant source of background γ-rays for accidental coincidences. Through Monte Carlo (MC) simulation studies, the tagging efficiency of RMDs is evaluated to be $\sim$70% for radiative decays with a photon energy higher than 48 MeV, when the coincidence time window between the RDC and the LXe calorimeter is chosen to be 8 ns. Two RDC modules are foreseen, one in the upstream (US) side and one in the downstream (DS). The US side detector (Figure 3.28: Left) is made of 704 squared scintillation fibers with 250μm thickness. The DS side detector (Figure 3.28: Right) is composed of 12 plastic scintillator bars for the hit time measurement and 76 LYSO crystals for the energy deposit observation, which are both read by MPPC.

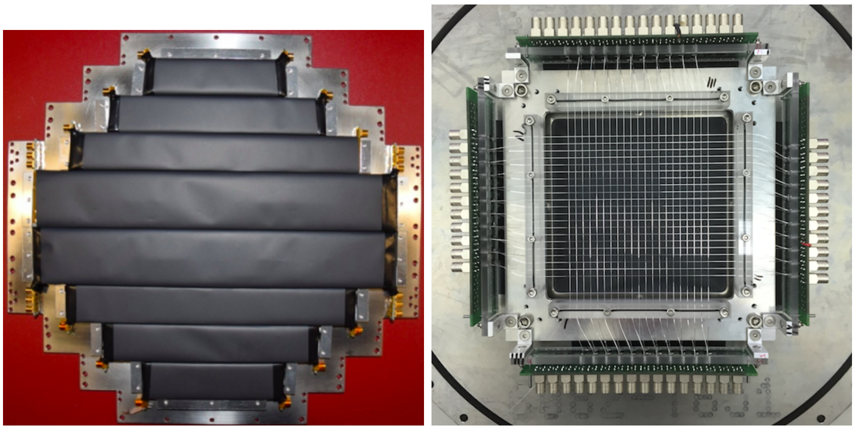

Figure 3.28: Left: RDC downstream. Right: Prototype RDC upstream.

3.3.5 Trigger and DAQ

The MEG II experiment will have a number of channels which is much higher than the one of the MEG experiment. For this reason an upgrade of the DAQ and the trigger system was mandatory. A new VME board, the WaveDream (WDB), was designed at PSI, as shown in Figure 3.29: Left. This board includes both the DAQ and the trigger system.

The trigger is organized on three boards: the WDB, the Trigger Concentrator Board (TCB) and the Data Concentrator Board (DCB), ()for more information see [4, 65]).

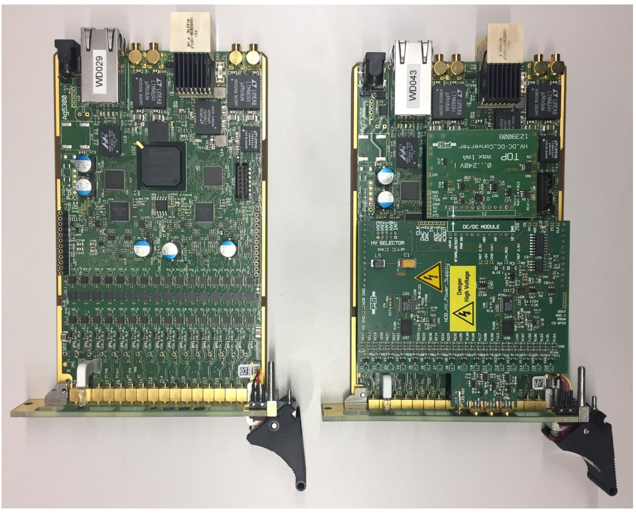

Figure 3.29: Left: The WaveDream Board with 16 single end channel. Right: The WaveDream Board with high voltage module installed.

In Figure 3.30 a comparison of the old versus the new trigger.

The DAQ board combines both the waveform digitizing technology using the DRS4 chip as well as the trigger and splitter functionality of current system. A simplified schematics of the new DAQ board is presented in Figure 3.31. The analog front-end of the DAQ board has been optimized to give an overall bandwidth of the order of 1 GHz, this is granted by a front-end with two switchable gain stages which can be combined to obtain a post-ampliplcation by a factor one to about 70. The post-amplification can be used to increase the signal amplitude coming from the different detectors which are typical in the order of a few tens of millivolt. By increasing the amplitude to a few hundred millivolt, the Signal-to-Noise Ratio (SNR) inside the DRS chip is improved allowing for a more accurate charge measurements.

For the full final system, the DAQ boards will be housed in a dedicated custom crate, which can bring a high cost-saving factor with respect to a standard VME system. The crate can hold up to 16 boards with a total of 256 channels plus a DAQ concentrator board which collects and combines the data before sending them to a PC. The new electronics will exploit the computing power and programming flexibility of modern FPGAs to adapt to the MEG II requirements, even if they will change during the operation. As MEG, the Data readout and event building is based on MIDAS.

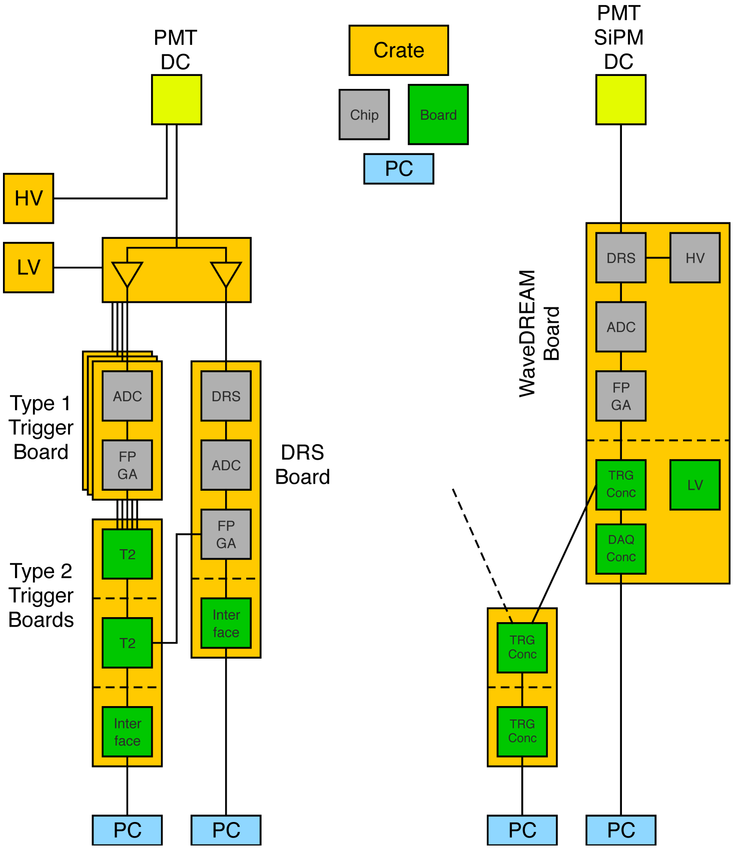

Figure 3.30: Comparison of the old (left) versus the new (right) TDAQ electronics designs.

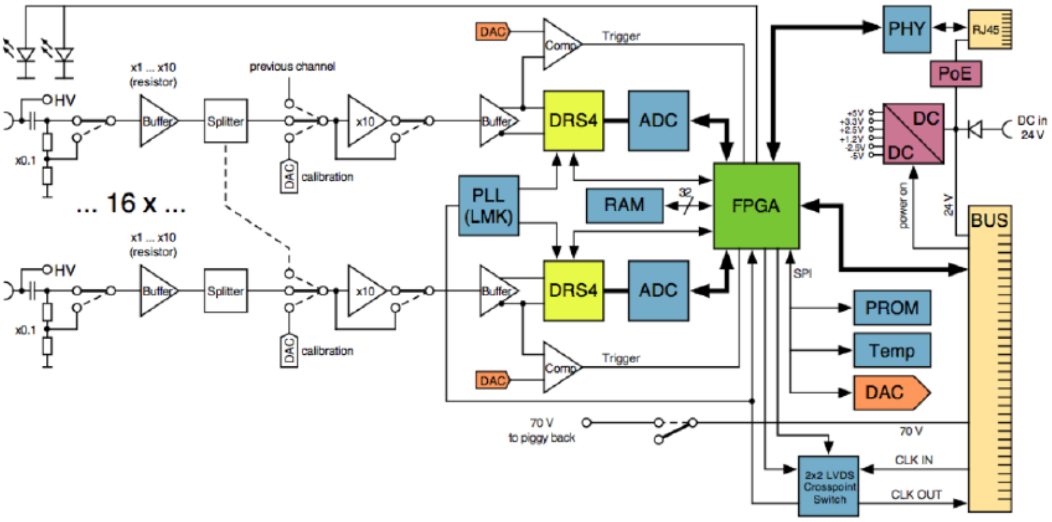

Figure 3.31: Simplified schematics of WaveDREAM board.

Part III

MEG II Drift Chamber

4

MEG II Cylindrical Drift Chamber Design

The positron tracker is the detector that will have major improvements. The new tracker consists in a unique volume low-mass Cylindrical Drift CHamber (CDCH) with a high granularity and a stereo wires configuration. The development of the CDCH involves four working groups within the MEG collaboration: the Lecce group is responsible for the wires procurement and tests, the wiring robot development for the construction of the individual planes that make up the CDCH and the front-end electronics, the Pisa group is responsible for the design and production of the end-plates, the wire PCBs and for the mechanical support and the Roma group is responsible for the gas control system and HV power supply. A PSI group is responsible for the final integration of CDCH in the MEG II experimental apparatus. In this chapter the reasons for the manufacturing choices (geometry, material and mechanics) of CDCH are presented.

4.1 Requirements for the MEG II Drift Chamber

As previously described, each detector must satisfy many requirements in MEG. In particular, the CDCH is required to satisfy several critical issues, especially after the not exciting performance achieved by the previous tracker system. Therefore the development of an innovative method of construction has been strongly desired. Requirements for the drift chamber are the following. First, amount of material used in the drift chamber should be minimized since this affects the tracking resolution and the background suppression capability. Second, the CDCH should be operational under the high counting rate environment especially for the innermost region. Finally, a good resolution is necessary for both the transverse and longitudinal directions.

4.1.1 Light Material

The minimization of the material has been the forefront subject in drift chamber development for high energy physics experiment since, at low momenta, the spatial resolution is limited primarily by multiple Coulomb scattering (MCS). In particular, if the experiment concentrates on the relatively low energy region, below GeV level, a substantially ultralow-mass drift chamber is essential. Furthermore, this is crucial for both the tracking accuracy and the multiple scattering reduction, because amount of generated backgrounds is proportional to the amount of material that composes the detector [82].
For the MEG experiment, the detector resolution and multiple scattering reduction are the most important keys. As discussed in the Chapter 3, the thickness of the target for MEG II was already reduced for minimizing the background.

4.1.2 High Rate

In MEG II, the expected muon rate is $7{\times}10^7$ μ^+/s, the same number of positrons are produced inside detector apparatus because of the muon decays. In such a heavily irradiation environment, a ultralow-mass tracker can cope only after a thorough study on the aging of detector materials [99]. The MEG II CDCH still has a lot of positrons hit regularly, especially in the innermost layer, where we expect a maximum flux of 30 kHz/cm^2. For this reason, the MEG II CDCH is designed to be operational in such an irradiation environment throughout all the period of data taking.

4.1.3 High Resolution

The MEG II CDCH must be designed to obtain excellent spatial resolutions both in the transverse and longitudinal directions by employing an innovative design and by using the minimum amount of material. This requirement is already satisfied if the requirement "Light Material" is fulfilled successfully, since the resolution is limited primarily by MCS. To minimize the MCS is necessary to reduce the amount of material traversed by the particles including the mechanical and electronic support of the readout.

4.2 Drift Chamber geometry description

The MEG II positron tracker is a unique volume, cylindrical drift chamber, with the axis parallel to the muon beam. The external radius (R_{ext}=284 mm) of the chamber is constrained by the available space inside the COBRA magnet, while the internal radius (R_{int}=196 mm) is large so that low energy positrons, less than 45 MeV/c, are swept out of the magnet by the gradient field without crossing the sensitive volume. Its length is dictated by the necessity of:

- avoiding any material along the positrons path to the timing counter in order to increase the positron efficiency;

- tracking the positrons trajectories up to as close as possible to the TC, in order to minimize the contribution of the track length measurement to the positron timing resolution and to increase the positron reconstruction efficiency.

The active length of the CDCH is $\sim$193 cm [72]. The drift cell size is indicated in the next paragraph.

4.2.1 Stereo Angle choice

A drift chamber is a gaseous tracking system that can be assimilated to a system of proportional wire detectors in a wide cylindrical volume, filled with a gas mixture. The sense wires are strung axially (or para-axially) to the chamber and are surrounded by a number of cathode wires in an electrostatic configuration similar to the elementary cell of a proportional counter. The information that can be gathered in the simplest drift chamber setup is the drift time: when an ionizing particle enters inside the sensitive volume, it creates free electrons and ions after colliding with a gas molecule; if the electric field intensity is strong enough, a primary electron generates an avalanche, whose electrons are collected by the anode wire after a certain drift time. Thanks to this information, it is possible to obtain the position where the avalanche started, which also corresponds to the point where the primary electron was created. The precision of this measurement depends on the type of gas mixture, which influences the drift velocity and the electron diffusion and on the geometrical configuration.

The geometrical configuration determines the electric field of the cells, and hence the readout electronics used to amplify the signals and the accuracy of data analysis algorithms.

A limiting factor of a drift chamber is the poor position resolution on along the sense wire. This can be overcome by inserting layers of wires tilted with respect to each other. These are the so called "stereo layers" and longitudinal resolutions below 1 mm can be reached for stereo angles of the order of a few hundred milliradians.

The stereo layers can be arranged in three different types of configurations (see Figure 4.1):

- constant stereo angle (ε_i) with the advantage of having the same view for all wires at the cost of same cell deformation as a function of the layer radius;
- constant projection angle (α_i) to preserve the cell aspect ratio for all layers at the cost of a height dependence of the cell size along z;
- constant drop (δ_0): in this configuration the radial extent of the cell is constant for all layers.

The constant drop configuration has been used in the KLOE drift chamber [16]. For the MEG II CDCH, we have chosen the constant projection angle $\alpha_i = \alpha = 30°$ configuration.

In Figure 4.1 a schematic view of a stereo wire configuration is shown. The wire length is $l_i = L/\cos\varepsilon_i$ where L is the chamber length and and ε_i is stereo angle. The wire radii at the end-plates and at the chamber center respectively are r_i and $r_{i0} = r_i \cos(\alpha_i/2)$, where α is the projected angle on the end-plates subtended by the wire. For MEG II CDCH, $\alpha = 30°$, L=1912 mm, the stereo angle ε_i is determined as a function of radius r_i by the following formula:

$$\varepsilon_i = \arctan\left(\frac{2r_i}{L}\sin\alpha\right) \tag{4.1}$$

and increases with r_i. In this way, the volume subtended by the wires in the drift chamber takes the shape of a rotational hyperboloid whose surface is given by the envelope of the wires planes. The radial position of the wire of the i-th layer along the z-axis is:

$$r_i(\mathrm{z}) = r_i \cos\alpha\sqrt{1+\tan^2\alpha\frac{4z^2}{L^2}}. \tag{4.2}$$

The stereo drop is defined as $\delta_{io} = r_i - r_{i0}$ ($\delta_i(\mathrm{z}) = r_i - r_i(\mathrm{z})$). The stereo angle sign can be both positive and negative different depending on the wires layers, thus defining two different views: U-view and V-view (see Figure 4.2). In this views, all wires with the same sign of the stereo angle are nearly parallel. Each layer consists of an anode sub-layer between two cathode sub-layers, all oriented at the same stereo angle, one placed at a smaller inner radius with respect to the anode sub-layer and

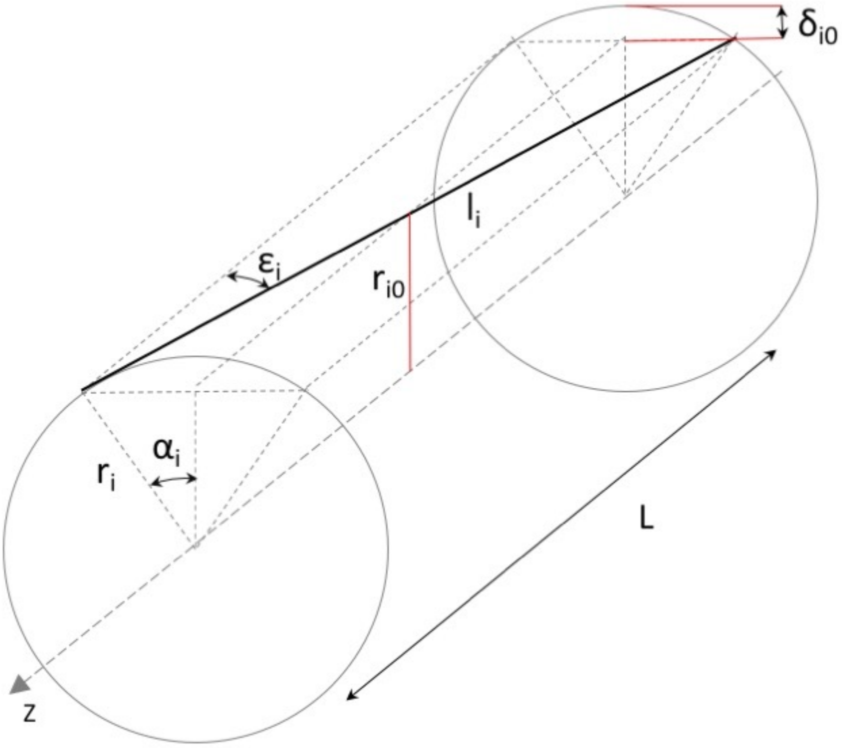

Figure 4.1: Geometrical configuration of a stereo wire. δ is the drop, ε_i is the stereo angle for the i-th layer, α is the projected angle on the end-plates subtended by the wire.

the other at a larger outer radius, the radial distance between these two sub-layers corresponding to the cell size.

Each anode sub-layer includes 192 sense wires alternated with 192 field wires. Each cathode sub-layer includes 384 field wires. Two consecutive layers, at apposite sign stereo angles, are contiguous, i.e., the outer cathode sub-layer of the inner layer is placed at the same radius as the inner cathode of the outer layer (Figure 4.2).

The ratio between the field wires and the sense wires in a generic cell is therefore 5:1. The cell size w_i is therefore $w_i = (2\pi r_i)/192$ and goes from ∼6.7 mm to ∼8.9 mm at z=0. The spacing between adjacent wire in a sub layer goes form ∼3.1 mm to ∼4.4 mm. The principal geometric parameters (α, ε and drop) of CDCH are reported in Figure 4.3.

The MEG II CDCH consists of 10 layers, with 10 anode sub-layers and 22 cathode sub-layers, the two additional cathode sub-layers are needed to complete the configuration of the first and last layers. Lastly, two layers of guard wires at an intermediate voltage, adjusted to equalize the gain of the inner and outer layers surround the active volume of the chamber.

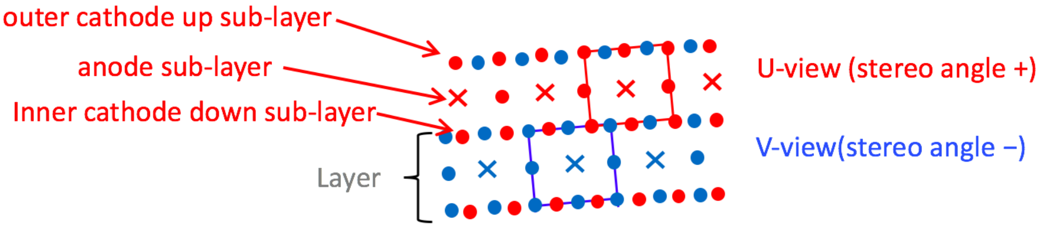

Figure 4.2: Drift cells configuration.

The total number of sense, field and guard wires are, respectively, 1920, 8448 and 768. The principal geometric parameters (α, ε and drop) of CDCH are reported in Figure 4.3.

4.2.2 Material and size of the wires

In the MEG II CDCH, three kinds of wires are used:

- the cathode wires (field): they define the drift cells of the chamber;

- the anode wires (sense): they collect the ionization electrons generated by the positrons traversing the gas of the drift chamber;
- the guard wires: they define the electric field configuration near the edge of the active volume.

The choice of the wire size is dictated by electrostatics considerations. In the MEG II CDCH, a gas gain of approximately 3×10^5 is required to be fully efficient. Under this condition, the electric field at the surface of the sense wires is about 2×10^5 V/cm (see Figure 4.4) for a sense wire diameter of 20 μm. The field wire diameter must be chosen so that the electric field, integrated over the surface of all field wires surrounding a sense wire, be less than 20 kV/cm, i.e., below the limit for positive ions in the Helium based gas mixture to avoid the onset amplification of dark currents [19, 77].

Therefore, the ratio of field wire surface to sense wire surface must be at least 10. Given the ratio of 5 to 1 of field wires to sense wires in acell, it is sufficient to chose a field wire diameter a factor 2 larger than sense wire diameter, i.e. 20 μm. The diameter of the field wires of the anode sub-layers have been increased from 40 μm to 50 μm since they would otherwise exhibit a higher electric field because of their proximity to the anode wire.

Several wire types, manufactured by different companies (Alloy Wire International, California Fine Wire Company and Luma Metall Fine Wire Products), were examined and tested. In a mixture or compound, the radiation length X_0 can be approximated by [52]:

$$X_0 = \frac{1}{\sum_i \frac{w_i}{X_i}} \tag{4.3}$$

where w_i and X_i are the fraction by weight and the radiation length for the i-th element respectively.

The possible options considered for the guard and field wires with their main features (density and the radiation length X_0, equivalent radiation length of all wires and of wires + gas, and the multiple scattering angular deflection Θ_{MCS} for a positron track) are listed in Table 4.1. The best performance is obtained with the aluminum 5056 alloy from the CFW company, which has been chosen for the field and guard wires with 40 μm and 50 μm diameters. The alloy is composed by aluminum

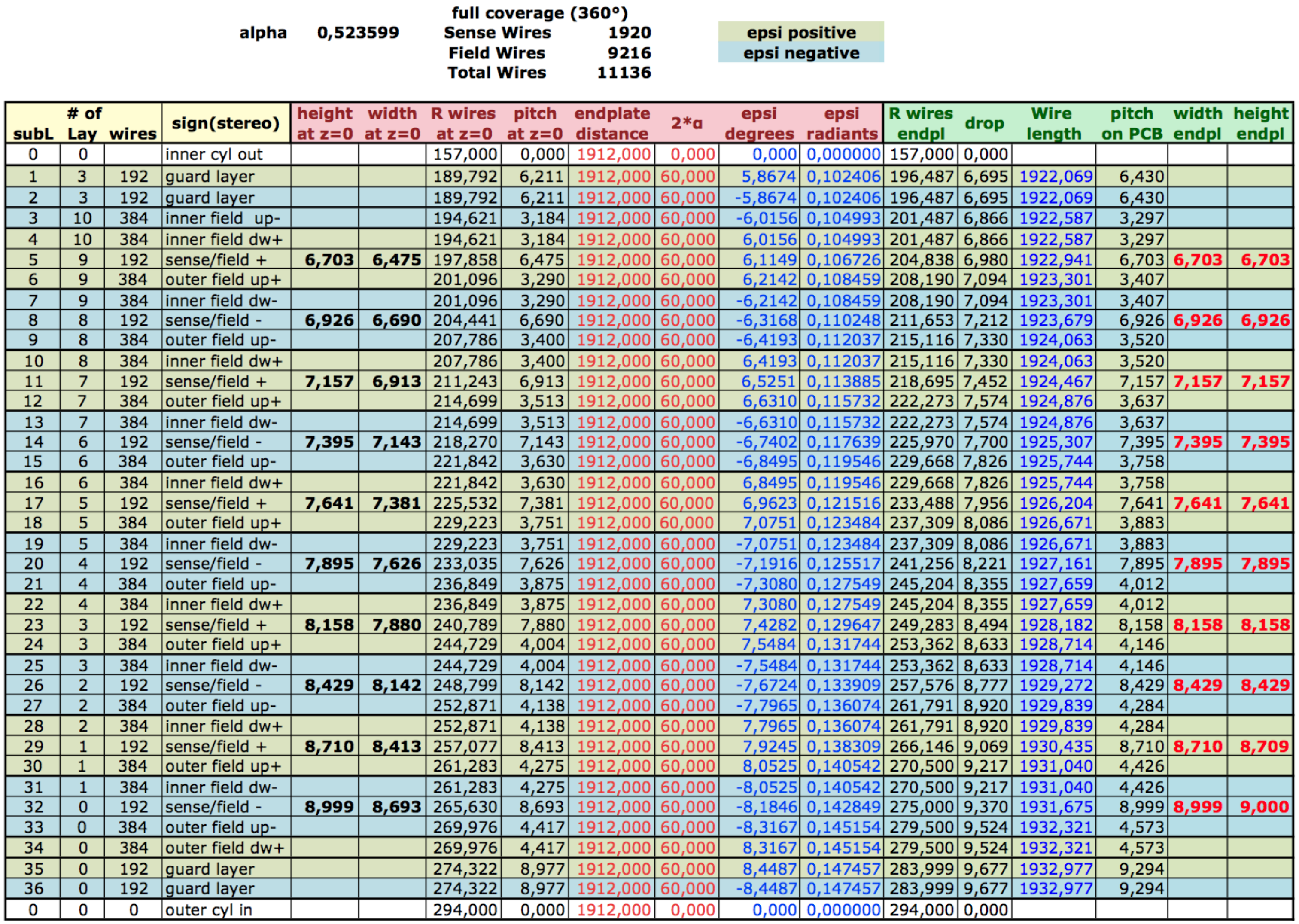

alpha 0,523599

full coverage (360°)
Sense Wires 1920
Field Wires 9216
Total Wires 11136

epsi positive
epsi negative

subL	# of Lay	# of wires	sign(stereo)	height at z=0	width at z=0	R wires at z=0	pitch at z=0	endplate distance	2*α	epsi degrees	epsi radiants	R wires endpl	drop	Wire length	pitch on PCB	width endpl	height endpl
0	0		inner cyl out			157,000	0,000	1912,000	0,000	0,000	0,000000	157,000	0,000				
1	3	192	guard layer			189,792	6,211	1912,000	60,000	5,8674	0,102406	196,487	6,695	1922,069	6,430		
2	3	192	guard layer			189,792	6,211	1912,000	60,000	-5,8674	0,102406	196,487	6,695	1922,069	6,430		
3	10	384	inner field up-			194,621	3,184	1912,000	60,000	-6,0156	0,104993	201,487	6,866	1922,587	3,297		
4	10	384	inner field dw+			194,621	3,184	1912,000	60,000	6,0156	0,104993	201,487	6,866	1922,587	3,297		
5	9	192	sense/field +	**6,703**	**6,475**	197,858	6,475	1912,000	60,000	6,1149	0,106726	204,838	6,980	1922,941	6,703	**6,703**	**6,703**
6	9	384	outer field up+			201,096	3,290	1912,000	60,000	6,2142	0,108459	208,190	7,094	1923,301	3,407		
7	9	384	inner field dw-			201,096	3,290	1912,000	60,000	-6,2142	0,108459	208,190	7,094	1923,301	3,407		
8	8	192	sense/field -	**6,926**	**6,690**	204,441	6,690	1912,000	60,000	-6,3168	0,110248	211,653	7,212	1923,679	6,926	**6,926**	**6,926**
9	8	384	outer field up-			207,786	3,400	1912,000	60,000	-6,4193	0,112037	215,116	7,330	1924,063	3,520		
10	8	384	inner field dw+			207,786	3,400	1912,000	60,000	6,4193	0,112037	215,116	7,330	1924,063	3,520		
11	7	192	sense/field +	**7,157**	**6,913**	211,243	6,913	1912,000	60,000	6,5251	0,113885	218,695	7,452	1924,467	7,157	**7,157**	**7,157**
12	7	384	outer field up+			214,699	3,513	1912,000	60,000	6,6310	0,115732	222,273	7,574	1924,876	3,637		
13	7	384	inner field dw-			214,699	3,513	1912,000	60,000	-6,6310	0,115732	222,273	7,574	1924,876	3,637		
14	6	192	sense/field -	**7,395**	**7,143**	218,270	7,143	1912,000	60,000	-6,7402	0,117639	225,970	7,700	1925,307	7,395	**7,395**	**7,395**
15	6	384	outer field up-			221,842	3,630	1912,000	60,000	-6,8495	0,119546	229,668	7,826	1925,744	3,758		
16	6	384	inner field dw+			221,842	3,630	1912,000	60,000	6,8495	0,119546	229,668	7,826	1925,744	3,758		
17	5	192	sense/field +	**7,641**	**7,381**	225,532	7,381	1912,000	60,000	6,9623	0,121516	233,488	7,956	1926,204	7,641	**7,641**	**7,641**
18	5	384	outer field up+			229,223	3,751	1912,000	60,000	7,0751	0,123484	237,309	8,086	1926,671	3,883		
19	5	384	inner field dw-			229,223	3,751	1912,000	60,000	-7,0751	0,123484	237,309	8,086	1926,671	3,883		
20	4	192	sense/field -	**7,895**	**7,626**	233,035	7,626	1912,000	60,000	-7,1916	0,125517	241,256	8,221	1927,161	7,895	**7,895**	**7,895**
21	4	384	outer field up-			236,849	3,875	1912,000	60,000	-7,3080	0,127549	245,204	8,355	1927,659	4,012		
22	4	384	inner field dw+			236,849	3,875	1912,000	60,000	7,3080	0,127549	245,204	8,355	1927,659	4,012		
23	3	192	sense/field +	**8,158**	**7,880**	240,789	7,880	1912,000	60,000	7,4282	0,129647	249,283	8,494	1928,182	8,158	**8,158**	**8,158**
24	3	384	outer field up+			244,729	4,004	1912,000	60,000	7,5484	0,131744	253,362	8,633	1928,714	4,146		
25	3	384	inner field dw-			244,729	4,004	1912,000	60,000	-7,5484	0,131744	253,362	8,633	1928,714	4,146		
26	2	192	sense/field -	**8,429**	**8,142**	248,799	8,142	1912,000	60,000	-7,6724	0,133909	257,576	8,777	1929,272	8,429	**8,429**	**8,429**
27	2	384	outer field up-			252,871	4,138	1912,000	60,000	-7,7965	0,136074	261,791	8,920	1929,839	4,284		
28	2	384	inner field dw+			252,871	4,138	1912,000	60,000	7,7965	0,136074	261,791	8,920	1929,839	4,284		
29	1	192	sense/field +	**8,710**	**8,413**	257,077	8,413	1912,000	60,000	7,9245	0,138309	266,146	9,069	1930,435	8,710	**8,710**	**8,709**
30	1	384	outer field up+			261,283	4,275	1912,000	60,000	8,0525	0,140542	270,500	9,217	1931,040	4,426		
31	1	384	inner field dw-			261,283	4,275	1912,000	60,000	-8,0525	0,140542	270,500	9,217	1931,040	4,426		
32	0	192	sense/field -	**8,999**	**8,693**	265,630	8,693	1912,000	60,000	-8,1846	0,142849	275,000	9,370	1931,675	8,999	**8,999**	**9,000**
33	0	384	outer field up-			269,976	4,417	1912,000	60,000	-8,3167	0,145154	279,500	9,524	1932,321	4,573		
34	0	384	outer field dw+			269,976	4,417	1912,000	60,000	8,3167	0,145154	279,500	9,524	1932,321	4,573		
35	0	192	guard layer			274,322	8,977	1912,000	60,000	8,4487	0,147457	283,999	9,677	1932,977	9,294		
36	0	192	guard layer			274,322	8,977	1912,000	60,000	-8,4487	0,147457	283,999	9,677	1932,977	9,294		
0	0	0	outer cyl in			294,000	0,000	1912,000	0,000	0,000	0,000000	294,000	0,000				

Figure 4.3: Summary of principal geometric parameters of CDCH. It can be noted that the cells are square to the endplate (width enpand height enpl) but not the center of the CDCH, the drop and the stereo angle (epsi, in absolute value) increases by moving away from the innermost layer and alpha is constant.

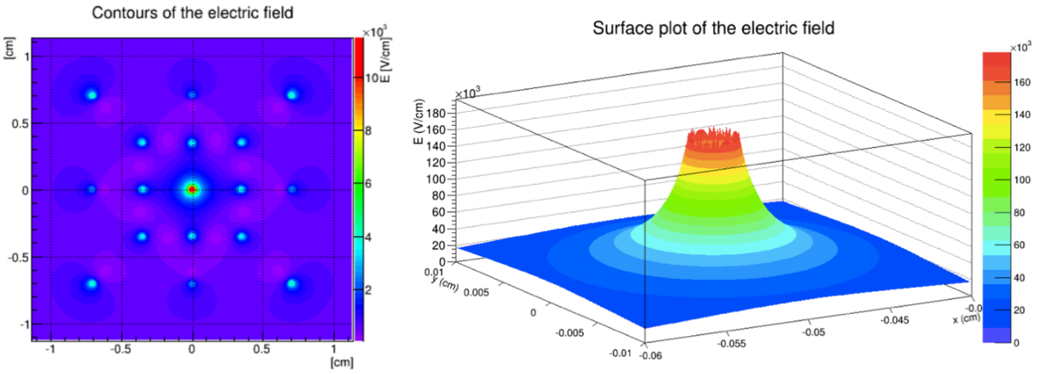

Figure 4.4: Left: The electric field in a drift cell. Right: The field close to the anode wire.

Table 4.1: Summary of the possible field and guard wires

Type	X_0 (mm)	ρ (g/cm^3) ($10^{-3}X_0$)	$\langle X\rangle^{wires}$ ($10^{-3}X_0$)	$\langle X\rangle^{tot}$ (mrad)	Θ^{wires}_{MCS} (mrad)	Θ^{tot}_{MCS}
Al(5056)	2.9	89	0.72	1.5	6	7.6
Stainless Steel (302)	7.8	17.8	2.2	3	9.3	11
Ti	4.51	36	1.26	2.1	6.8	9
CuBe	8.36	14.7	2.58	3.4	10.1	11.7

(94.6%), magnesium (5.01%), iron (0.14%), silicon (0.1%) and other elements. The wire is silver-plated to protect the aluminum alloy and to facilitate the soldering phase. The density is ρ=2.9 g/cm^3 and the resistivity is $\simeq$20 Ω/m. The stress-strain curves for the aluminum wires are shown in Figure 4.5 and Figure 4.6. They exhibit an elastic limit about 43 g and 67 g, respectively for 40 μm and 50 μm diameter, with a maximum elongation of about 4,6 mm per meter of wire and a break point at about 50 g (Figure 4.5) and 75 g (Figure 4.6) respectively.

Two possible wire have been considered for the anodes: pure-tungsten (W) and tungsten-3%rhenium (W/Rh). From Figure 4.7 one can notice that the W/Rh wire has a higher elastic limit 7 mm/m at 85 g with respect to the pure W wire (5.2 mm/m at 62 g) but this advantage cannot be exploited since it lays well outside of the elastic range of the Al field wires. On the other end, the W/Rh wire is less uniform moreover, exhibits and, a larger resistivity (293 Ω/m vs 175 Ω/m with respect to the W wire) which means a readout electronics with less bandwidth and gain and, therefore, higher noise. These features are critical for the application of the cluster counting technique [97, 43], hence the choice for the sense wires has been 20 μm pure-W wires, gold plated (ρ=19.27 g/cm^3). In Figure 4.7 is shown the stress-strain

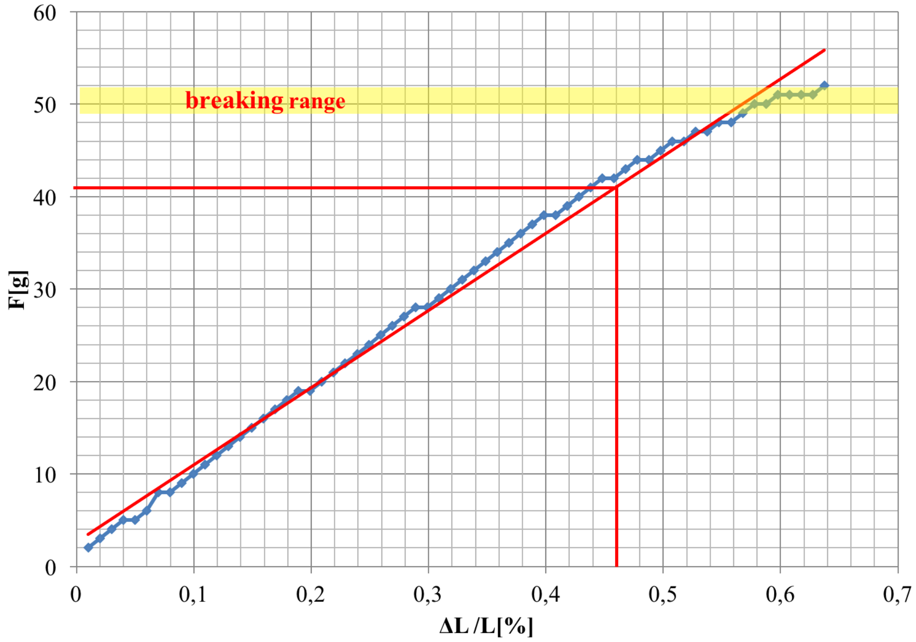

Figure 4.5: Stress-strain curve for Aluminu5056-AG pltd 40 μm.

curve for the pure-W wire. In Figure 4.8 some hysteresis studies on the pure-W wire are shown.

The mechanical parameter of the Al5056-Ag pltd and W-Au pltd wires chosen for the CDCH are summarized in Table 4.2. In Figure 4.8 is shown the operating range of all wires. The operating point is chosen at an absolute elongation of 4 mm for the 2 m long wires, corresponding to a relative elongation of 0.2% at about 40% of the elastic limit for all wires.

Table 4.2: Mechanical parameter of the wires.

Wire	Elastic limit Elongation (mm/m)	Elastic limit Tension (g)	Break point Elongation (mm/m)	Break point Tension (g)	Elastic Modulus (g/mm/m)
20 μm W	5.30 ± 0.05	62.0 ± 0.7	19.7 ± 0.3	86.0 ± 2.5	11.92 ± 0.091
40 μm Al	4.81 ± 0.14	44.3 ± 0.8	5.82 ± 0.33	50.0 ± 2.5	9.20 ± 0.13
50 μm Al	4.90 ± 0.04	69.5 ± 0.5	5.58 ± 0.31	75.3 ± 3.9	14.17 ± 0.20

4.2.3 Cell electrostatic stability

In a drift chamber, the electrostatic forces among field and sense wires may be not negligible and may displace a wire from its nominal position creating distortions in the electrical field configuration with a consequent increase of the electrostatic force

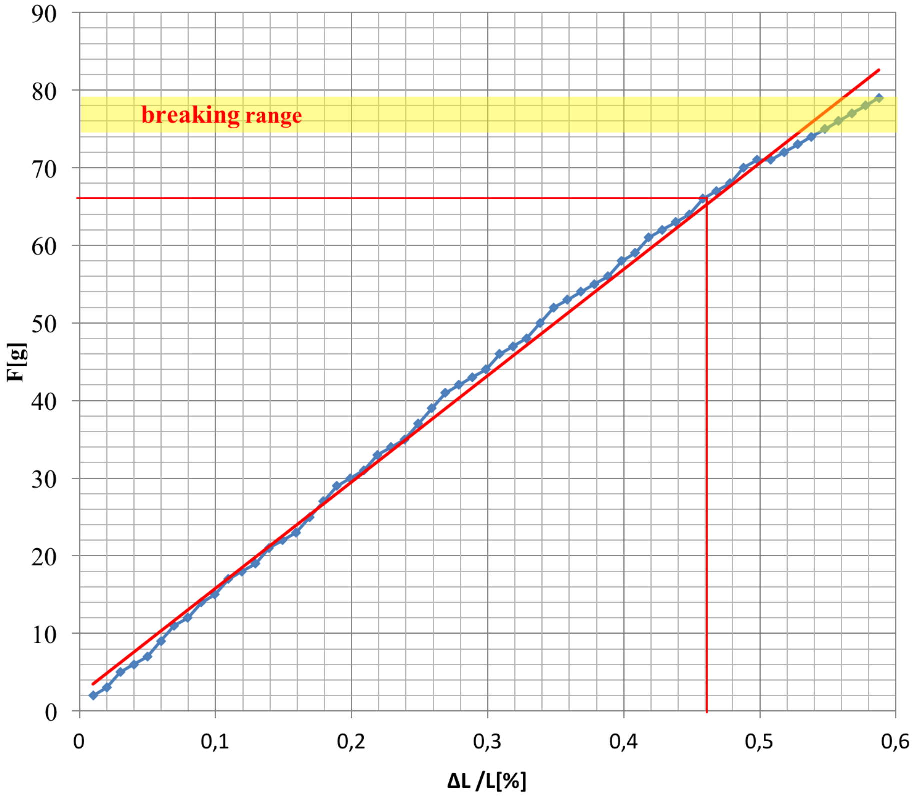

Figure 4.6: Stress-strain curve for Aluminu5056-AG pltd 50 μm.

among wires [97]. Because of mechanical tolerances in the chamber construction, the wire position is known with an uncertainty of $\sim$50 μm from the center of the chamber and with uncertainty of $\sim$20 μm on the position along the circumference of the layer (Section 6.1.3), while the uncertainty on the length is about $\sim$200 μm due to the deformation of the end-plates (Section 4.5), to these must add the contribution due to the spread of the wires gravitational sagittas. The equation that describes the vertical displacement x, from the ideal straight trajectory of a wire as a function of the coordinate along y is [100]:

$$T\frac{d^2x}{dy^2} + kx + g\rho\sigma = 0 \tag{4.4}$$

where T is the mechanical tension given to the wire, kx is the electrostatic force acting on it, ρ is the wire density and σ is its transverse cross section, all per unit length. Solving Eqution 4.4 for the case of no electric field, we obtain the gravitational wire sagitta:

$$s_g = \frac{l^2 g\sigma\rho}{8T} \tag{4.5}$$

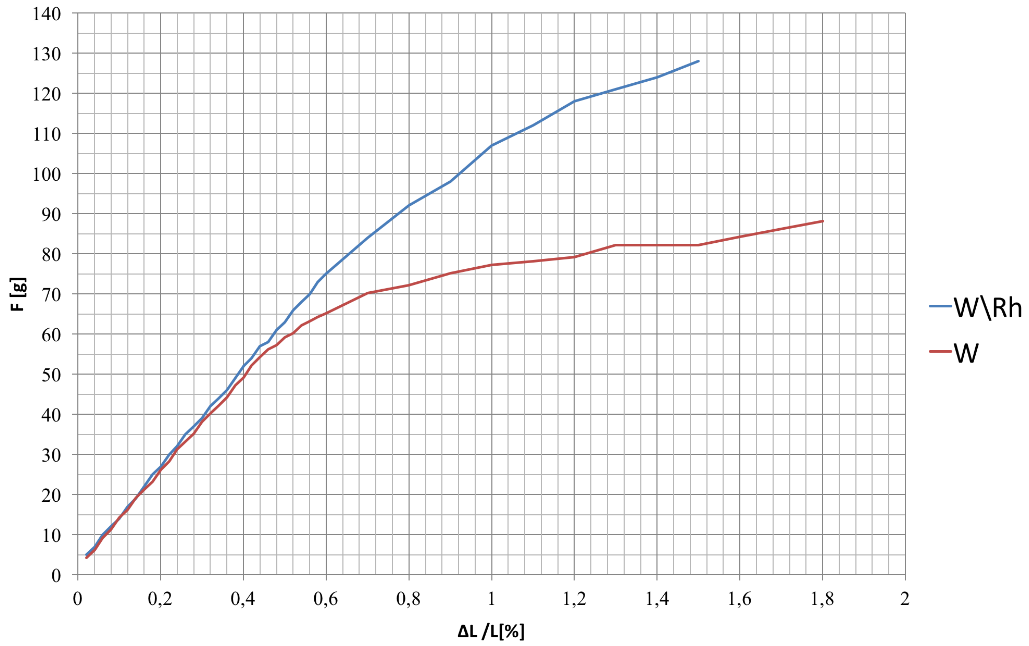

Figure 4.7: Stress-strain curve for W-Au pltd 20 μm and W/3%Rh.

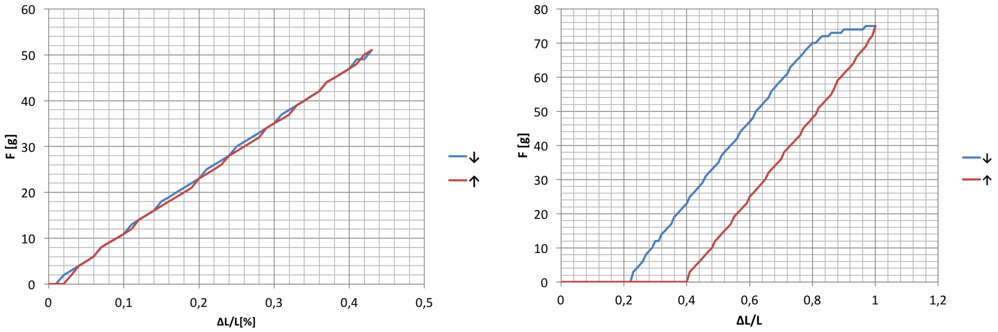

Figure 4.8: Hysteresis curve after elongations below (at left) and above (at right) the elastic limit.

where l is the wire length. The sagitta is inversely proportional to the mechanical tension. In the presence of an electric field, the sagitta due to both the electrostatic and the gravitational forces, is:

$$s = s_g \frac{2}{q^2} \left(\frac{1}{\cos q} - 1 \right), \tag{4.6}$$

$$q^2 = \frac{k}{T} \left(\frac{L}{2} \right)^2. \tag{4.7}$$

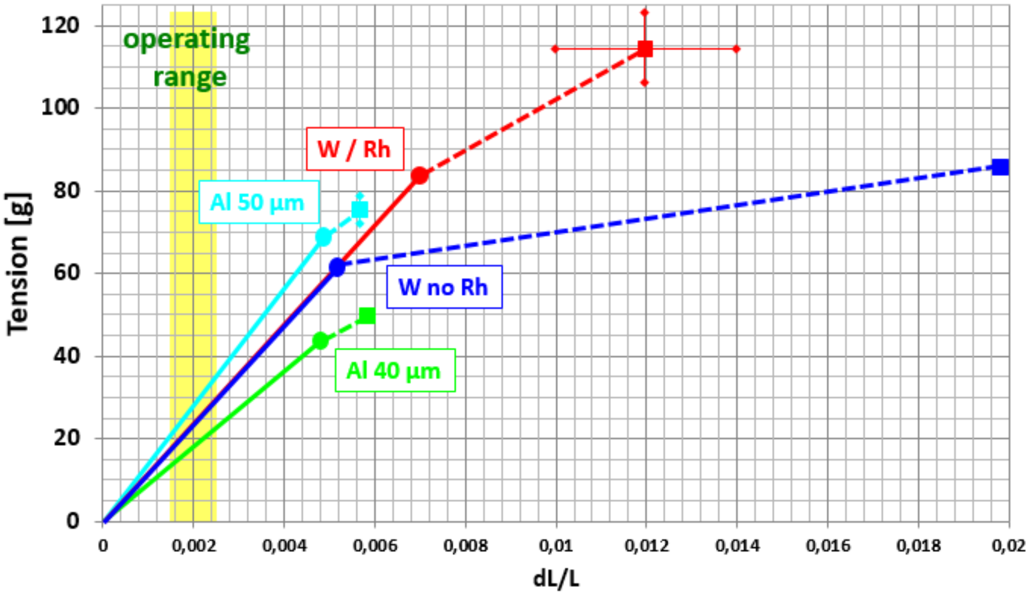

Figure 4.9: Stress-strain curve for all wires. In yellow, the operating range determined by MEG.

The term $\alpha = \frac{2}{q^2}\left(\frac{1}{\cos q} - 1\right)$ represents the incremental factor of the gravitational sagitta due to the addition of the electrostatic force. The cell is electrostatically stable when $q^2 \leq 1$. An approximated expression for q^2 can be written:

$$q^2 = 4\pi\epsilon_0 \frac{1}{[a\ln(a/r)]^2} \frac{V^2}{2T} \frac{L^2}{4} \tag{4.8}$$

where r is the radius of the wire and a is the typical spacing between sense and field wires. in the case of MEG II, q^2 =0.016<1 and the electrostatic sagitta is about 100 μm, therefore stability.

In Table 4.3 the expected values obtained from the Equation 4.5 of the gravitational sagitta for the wires used in the CDCH with a elongation ΔL=4 mm are reported.

Table 4.3: The gravitational sagitta ΔL=4 mm with the nominal wiring mechanical tension

Thype	Sagitta(μm)	Mechanical Tension (g)
20 μm W-Au pltd	115	24.52
40 μm Al-Ag pltd	91	19.25
50 μm Al-Ag pltd	93	29.64

4.3 GAS choice

A very important element for a drift chamber is the gas filling the sensitive volume. Usually, a mixture of gases composed of a noble gas and a quencher is used. Noble gases are used because they require lower electric field intensity for the avalanches formation. The quencher is required to avoid self-sustained discharge.
MEG CDCH requires a highly transparent gas to minimize the MCS, for this reason it uses a Helium based gas mixture. Helium based gas mixtures offers some advantages:

- long radiation length (pure He: $X_0 \simeq$5300m at STP) and the high ionization potential of helium (24.5 eV compared to the 15.7 eV of argon) causes small primary ionization density ($\sim 4.8/cm$);
- the time separation between consecutive ionization clusters goes from a few ns to a few tens of ns;

both specially suitable for cluster counting techniques. In conclusion, the MEG CDCH uses an ultra-low mass gas mixture with Helium and Isobutane (85:15) with X_0=81.09 g/cm^2, in this configuration, a 52.8 MeV/c positron produces about 14.5 ionization clusters/cm.

4.4 Multiple scattering and Material Budget Estimate

In MEG, the accurate reconstruction of the positron tracks is strongly influenced by MCS. Its minimization is critical in order to achieve high momentum and angular resolutions.
However, since the CDCH is made up of layers of wires, which significantly increases the amount of material crossed by the positrons and, therefore, the MCS contribution, great attention was posed on the wire material and on their size. The average amount of material traversed by a positron emitted at the origin with a radius of curvature r

is calculated assuming that the wires are uniformly smeared in the active volume of chamber. The equivalent amount of material in terms of radiation length $\delta x/X_{0eq}$ traversed by a positrons in a generic cell is:

$$\frac{\delta x}{X_{0eq}} = \frac{\rho_{gas} h}{X_{0gas}} + \sum_{i=1}^{3} x_i \frac{\pi r_i^2}{h} \frac{\rho_i h}{X_{0i}} \tag{4.9}$$

where h is the cell width, ρ_{gas} and X_{0gas} are, respectivelly the density and the radiation length of the gas mixture, x_i, r_i, ρ_i and X_{0i} the number, radius, density and radiation length of the different wires, where i stands for sense, 50 μm field and 40 μm field wires. in MEG II chamber, we have:

- ρ_{gas}=0.5398 g/cm^3, X_{0gas}=81,09 g/cm^2;
- x_{sense}=1, r_{sense}=10 μm, ρ_{sense}=19.27 g/cm^3, X_{0sense}=6,76 g/cm^2;
- $x_{50field}$=1, $r_{50field}$=25 μm, $\rho_{50field}$=2,9 g/cm^3, $X_{050field}$=24,01 g/cm^2;
- $x_{40field}$=4, $r_{40field}$=20 μm, $\rho_{40field}$=2,9 g/cm^3, $X_{040field}$=24,01 g/cm^2.

Therefore

$$\frac{\delta x}{X_{0eq}} = 18.76 \times 10^{-6} \tag{4.10}$$

for an average positron track, hitting in average 60 cells, one has a total contribution of:

$$\langle \frac{1}{\sin\alpha} \rangle \times 60 \frac{\delta x}{X_{0eq}} = 1.3 \times 10^{-3} \tag{4.11}$$

where α is the average crossing angle of the positron track within a cell $\langle\alpha\rangle = 60^\circ$. Table 4.4 lists the individual contribution of the various materials to the total radiation length of the chamber.

4.5 CDCH Mechanics

The positron tracker is composed of 10 concentric layers, divided into 12 identical 30° sectors per layer, each of which is composed 16 drift cells. [3, 39]. The wires are soldered on ad hoc wire PCBs (see Section 5.2), fixed at the right distance on

Table 4.4: Multiple scattering contributions.

Item	Description	Thickness(10^{-3} X_0)
Target	140 μm Polyethylene	0.21
Sense wires	20 μm W	0.16
Field wires	40 μm and 50 μm Al	0.33
Inner gas	He	0.06
CDCH gas	85He:15iC_4H_{10}	0.53
Inner foil	20 μm Mylar	0.14
Total	1 full turn (without) target	1.49(1.28)

'upstream' (US) and 'downstream' (DS) end-plates with respect to the muon beam. The stereo angle is obtained by inserting the wire PCB in the i-th sector of the US end-plate and in the $(i \pm 2)$-th sector of the DS end-plate.

The cells are approximately squares and at the end-plates their widths range from 6.7 mm to 9.0 mm. The corresponding cell size at the center of the chamber (z=0) is reduced by about 15% with respect to the end-plates (see Equation 4.2). Figure 4.10 shows a schematic of wire position of the wires at the end-plates (Bottom) and at the center (Top) of the drift chamber.

The end-plates, a 2-mm thick carbon fiber cylindrical support at the outer radius R=294 mm and an aluminized mylar foil, 20 μm thick at the inner radius R=157 mm, delimit the sensitive volume of CDCH.

The end-plates, see Figure 4.11: Right, have a helm shape with 12 spokes at 30°, one per sector and are made up of gold-plated aluminum with a thickness of 30 mm. They are loaded with a total force of 3000 N due to the tension on the wires and have a maximum deflection at the extremity of the helm spokes of about 200 μm, tolerable, given the elongation of the wire.

The gas volume in each sector is closed by the radial overlap of the wire PCB's, to which the ends of the wires are soldered, alternated with PEEK spacers (Figure 4.11: Left), to define the proper cell height in each of the twelve sectors.

The end-plates are empty up to a radius of 161.5 mm, where the mylar cylindrical foil (see Figure 4.12) separating the active volume of the chamber from the inner COBRA volume, filled with pure Helium, is placed. The thin foil is maintained under tension by some rings and a slight pressure gradient between the gas chamber and the helium in the COBRA volume. The nominal distance between the two end-plates is 1932 mm. The carbon fiber structure (see Figure 4.13) is fixed on the end-plates

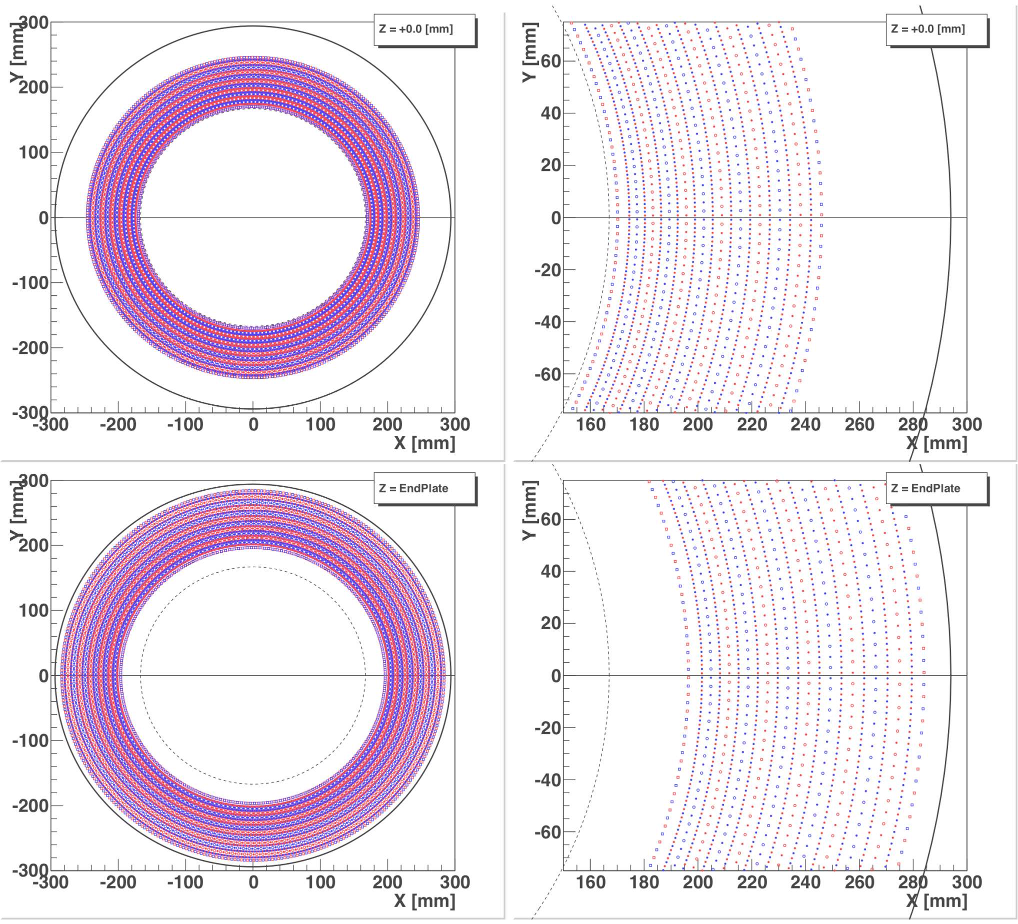

Figure 4.10: Schematics of wires position in the drift chamber at the end-plates (Bottom) and at the center (Top). The guards are represented with an empty square, the cathodes with a in filled circle and the anodes with a empty circle. Blue and red colours correspond to the different signs of the stereo angles.

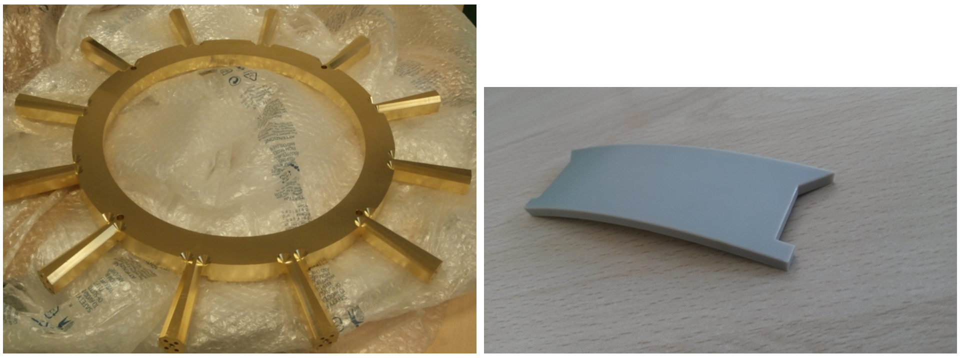

Figure 4.11: Left: The CDCH end-plates. Right: The spacer.

with screws and its deformation occurs at about 85 times the nominal tension as it results from FEA (Finite Elements Analysis) simulation [38].

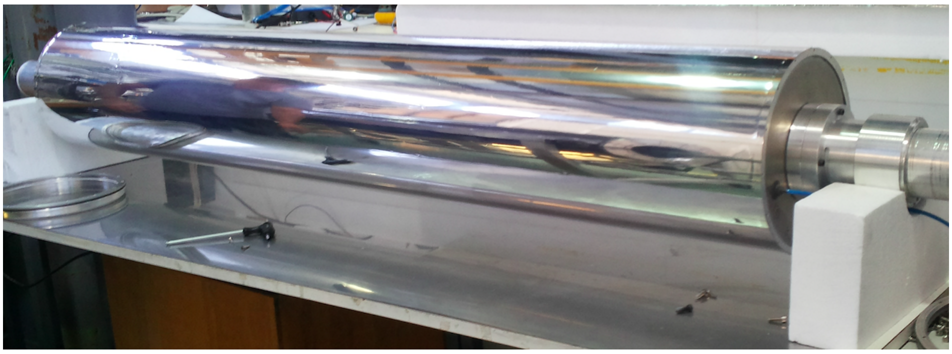

Figure 4.12: Prototype of mylar inner foil.

Figure 4.13: A piece of the carbon fiber cylindrical structure.

4.6 Read-out Electronics

The fundamental requirement of electronics read-out is to amplify and to acquire high-speed signals from the CDCH. For this purpose, a specific high performance 8-channels front-end electronics (FE) has been designed by using commercial devices, shown in Figure 4.14, and tested [11, 10].

The FE single channel schematic is represented in Figure 4.15, it is a double-stage gain amplifier based on an Analog Device ADA4927 [42] and a Texas Instruments THS4509 [59], giving a 3-dB bandwidth around 1 GHz at a gain of 21 dB, as

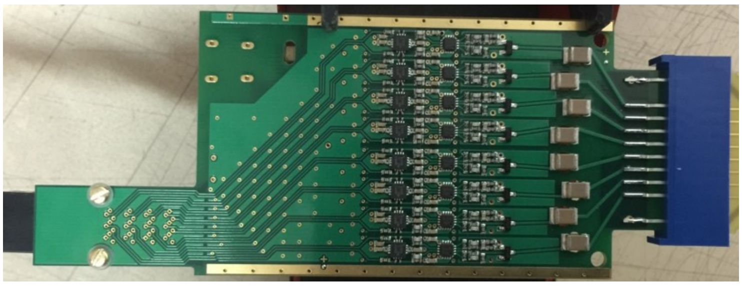

Figure 4.14: FE PBC Board.

illustrated in Figure 4.16.

The FE PCB is very compact and the width of the single channel on the PCB is about

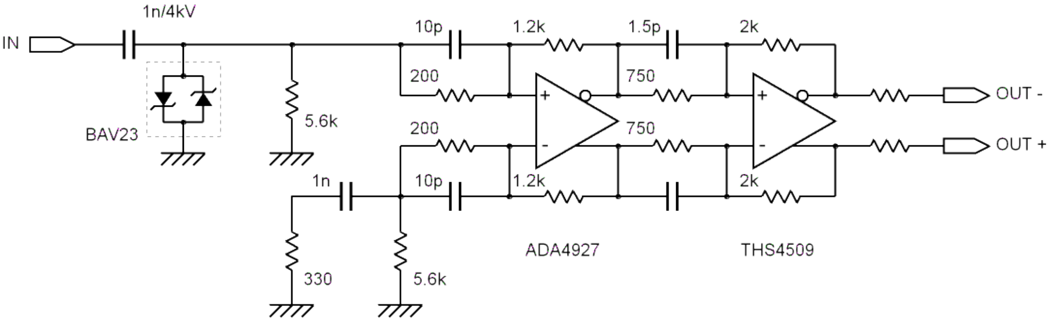

Figure 4.15: FE single channel schematic.

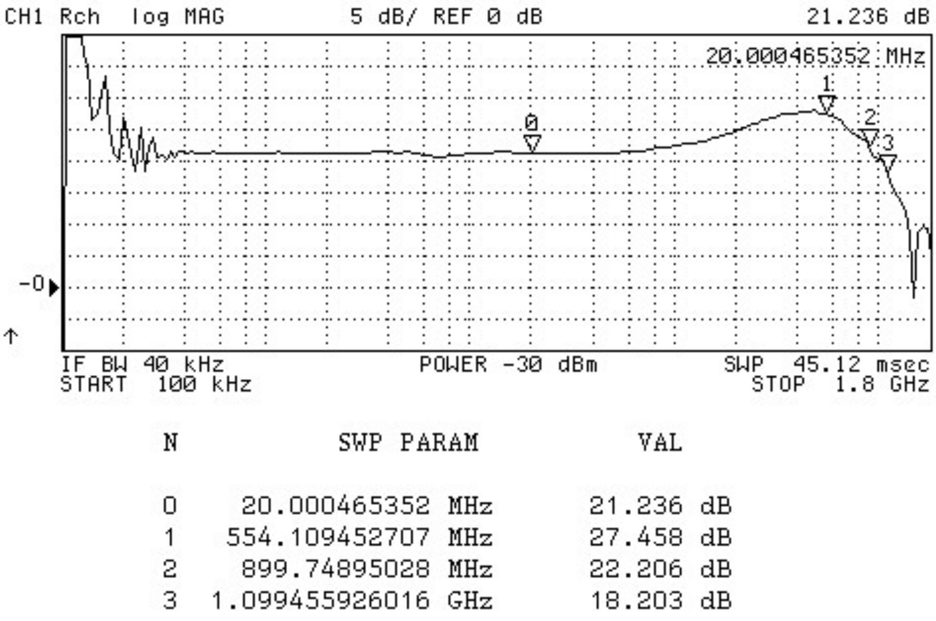

N	SWP PARAM	VAL
0	20.000465352 MHz	21.236 dB
1	554.109452707 MHz	27.458 dB
2	899.74895028 MHz	22.206 dB
3	1.099455926016 GHz	18.203 dB

Figure 4.16: Frequency response of FE.

7 mm. Considering the available space between the layers and the area of the FE

output connector socket used, three different versions of PCB have been designed, one with the output connector on the right, one on the center and one on the left, as visible in Figure 4.17.

Pre-amplified differential signals are successively digitised by the Wave Dream Board (WDB), connected to the FE Board through a 5 m long custom cable (Amphenol Spectra Strip SkewClear [33]). In order to balance the attenuation of the output cable, a pre-emphasis RC network has been designed and implemented on both the stages, which introduces a peak to compensate the cable losses (see Figure 4.16: marker 1).

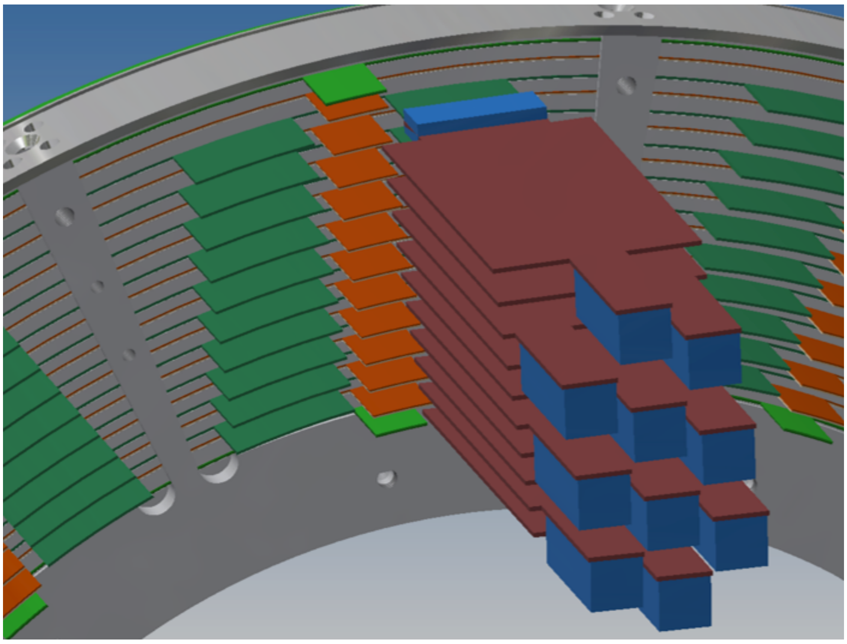

Figure 4.17: Drawing of a sector of end-plate with FE PCBs.

The power dissipated by each FE PCB is about 2.4 W. Each end-plate, dissipates a heat of approximately 576 W and therefore, both end-plates need to be cooled with a chiller (Julabo FL1201 [61]) with the temperature of FE Board electronics continuously monitored by sensors in the end-plates.

4.7 High Voltage and gas system

As mentioned in the Section 4.3 and Section 4.2, the MEG II CDCH has a gas gain (avalanche multiplication factor) of a few 10^5. At these values, the electric field on the surface of the anodes is about 200 kV/cm, while on the surface of the cathode wire is about 20 kV/cm, below the onset of positive ions multiplication. This results in an anode voltage of about 1600 V, while the cathodes wires are kept at ground. The guard wires are at about 900 V. MEG II maintains the same high voltage system as MEG I with the addition of some HV modules [75].

The gas system controls the pressure and the quality of the gas of CDCH. The gas flow is about 700 sccm and the chamber volume exchange occurs every 10 hours. The pressure of the detector is based on the differential pressures with the volume of COBRA (helium atmosphere), and with the atmospheric pressure. Gas quality is controlled by oxygen sensors, isobutane sensors and humidity sensors, and by a monitor chamber [69], which monitors the gas amplification in real time with radioactive sources and cosmic rays.

4.8 Conclusion

The high wire density (12 wires/cm^2) does not allow for the use of a traditional feed-through technique as wire anchoring system and therefore it was necessary to develop new wiring strategies. The number of wires and the stringent requirements on the precision of their position and on the uniformity of the wire mechanical tension impose the use of an automatic system to operate the wiring procedures. This system will be described in the next chapter.

5

CDCH construction: the wiring robot

Due to the high wire density, the use of the traditional feed-through technique as wire anchoring system can hardly be implemented and therefore it is necessary to develop new wiring strategies. In this chapter, the semi-automatic system used for wiring the CDCH, the wiring robot, will be presented.

5.1 The construction technique of CDCH

Normally the drift chamber end-plates serve the purpose of containing the gas and of anchoring the wires in the correct position by means of feedthroughs. Consequently, the wire positions and tensions are influenced by the gas differential pressure which can deform the end-plates [21].

Moreover, because of the high wire densities, the use of feedthrough prevents the possibility to make small cells. In the MEG II CDCH, the gas containment function is performed by the peek spacers and by the wire PCBs (see Section 4.5), on which wires are soldered. The use of wire PCB allows for higher densities of wires, accurately positioned (a few tens of microns) and strung at the correct mechanical tension. The design of the wire PCBs is crucial for the correct geometry of the CDCH and for its operation.

5.2 The wire PCB

The wire PCBs are made of400 μm thick FR4 board with 35 μm gold plated copper tracks. Three types of wire PCBs have been produced (guards, cathodes and anodes) schematically shown in Figure 5.1. Three reference markers (crosses) are printed on

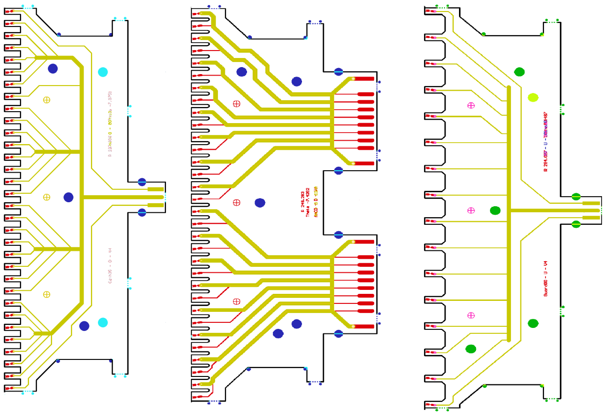

Figure 5.1: Wire PCB for guards (right), cathodes (left) and anodes (center)

the wire PCBs together with some sub-layers information (layer number, PCB type, stereo angle). The reference markers are used for the optical survey to check each wire-PCB position once they are mounted on the end-plates, in addition there are five holes (two at fixed position and three depending on the wire layers) for proper handling during assembly.

The anode PCBs have pads for both anode and cathode wires (16 pads each) and two 8-channel connectors, where the anode pads are individually routed, while the cathode pad are daisy-chained together. The cathode and guard wire PCBs have respectively 32 and 16 pads, all daisy-chained together, with the exception of the two extreme wires, kept floating for independent readout of the mechanical tension. All wire PCB pads are oriented along the stereo angle to prevent unwanted wire stresses at the soldering, as shown in Figure 5.2. For symmetry reason, two versions of wire PCB have been designed for each sublayer, one for the upstream side (US) and another one for the downstream side (DS) (see Figure 5.3).

The wire PCBs shape is complementary to the shape of the spokes in order to fit into the correct position at the end-plates in each sector. The wire PCBs dimension, the pitch between soldering pads and the wiring angle vary as a function of the radius and, therefore, of the number assigned to the wire PCB.

As seen in the Section 4.2, a layer consists of three sub-layers, separated by suitable spacers, two consecutive layers (i-th and $i+1$-th) having cathode sub-layers at the same CDCH radius (see Figure 5.4). This is achieved by overlapping the innermost cathode wire PCB of the i-th layer with an equal wire PCB mounted upside down and, therefore, at the opposite sign stereo angle, as shown in Figure 5.5.

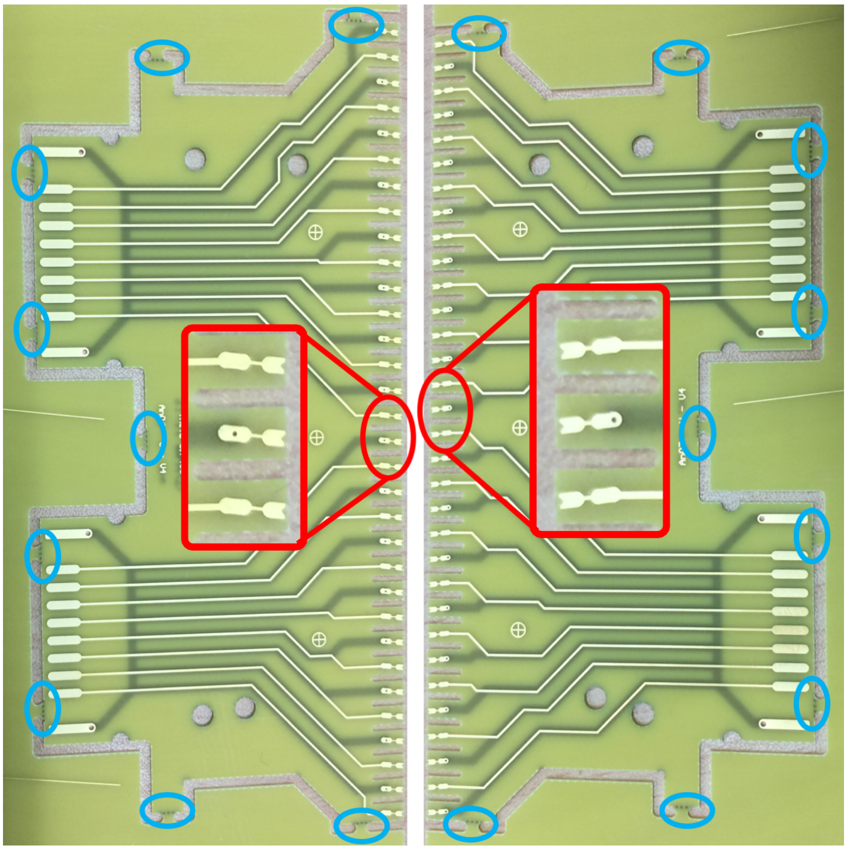

Figure 5.2: Pads are aligned at the different stereo angle. In blue circles, the "punched points" are indicated.

The US and DS wire PCB are coupled together in a single FR4 board for a precise alignment of the PCBs during the wiring procedure, in this way the geometrical parameters of the CDCH (length, stereo angle, wire pitch) are all respected. All parameters of the CDCH geometry are generated by a C++ macro [38].

5.3 Wiring parameter

To perform the wiring phase, it is necessary to know the different parameters of CDCH as a function of the layer radius, in Figure 5.6 the value of the parameter for the different sub-layers are reported and Figure 5.7 shows the parameters necessary to the wiring robot for a positive stereo angle (Top) and negative stereo angle (Bottom). In the following, the calculations to obtain the parameter values according to the geometry described in Chapter 4 are listed. The parameters of the wire PCB of each sub-layer are:

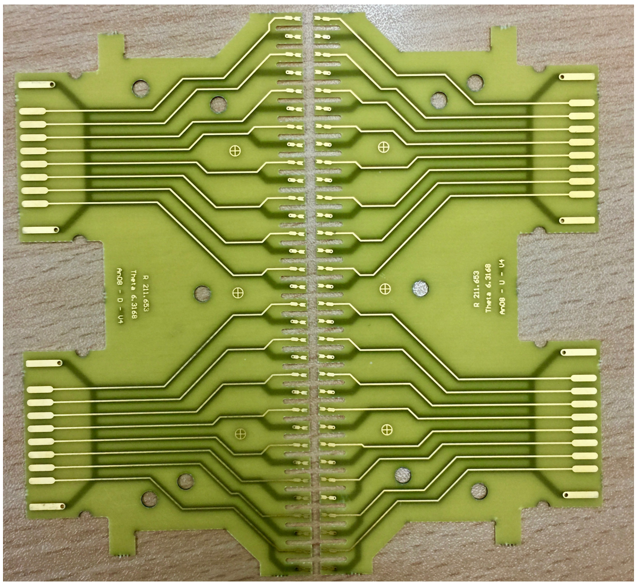

Figure 5.3: PCB US and PCB DS.

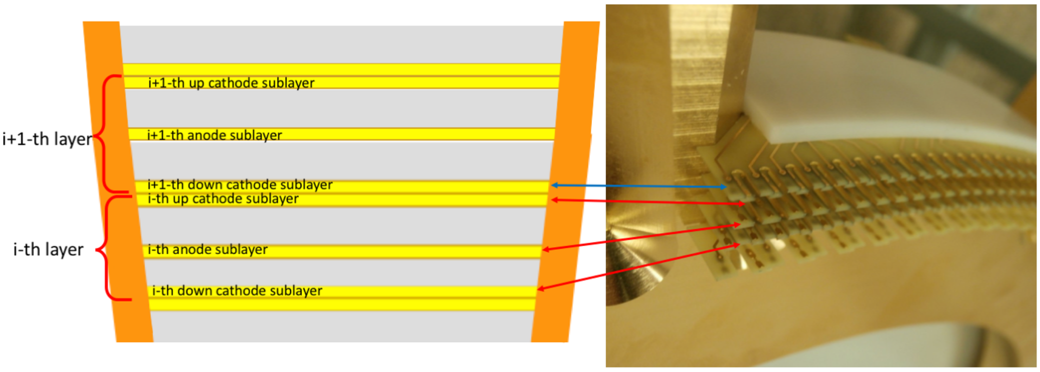

Figure 5.4: Stack of PCBs and PEEK spacers defining the drift chamber geometry.

- p(pitch): distance between two pads on the wire PCB;
- ε: stereo angle;
- L_0:nominal wire length.

and r_c is the rotating cylinder radius (Section 5.4.1) of the wiring robot. From these parameters one can calculate:

- ϑ_ε: angular pitch at stereo angle ε

$$\vartheta_\varepsilon = \frac{1}{2} \arcsin\left(2\frac{p}{2\pi r_c}\cos\varepsilon\right); \tag{5.1}$$

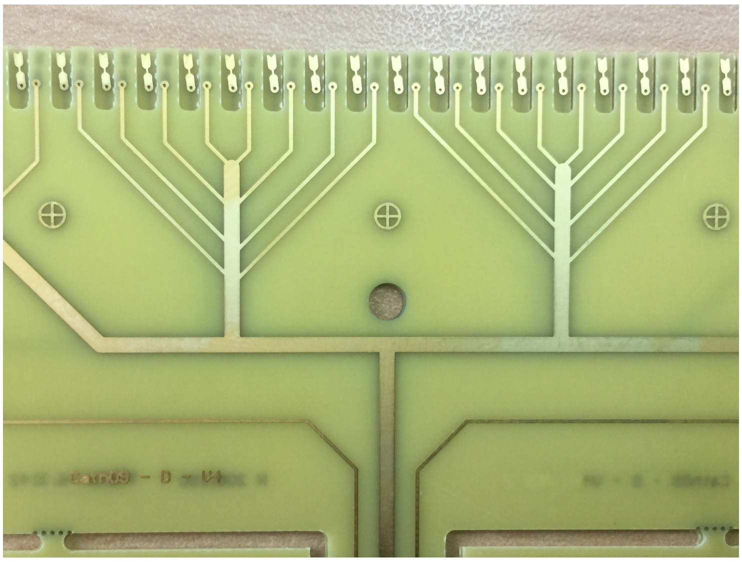

Figure 5.5: Cathode wire PCB flipped.

- p_ε: pitch(distance between wires) at stereo angle ε (Figure 5.7)

$$p_\varepsilon = p\frac{\cos\varepsilon}{\cos\vartheta_\varepsilon}; \tag{5.2}$$

- φ: angle between wire PCB and cylinder axis (Figure 5.7)

$$\varphi = \varepsilon - \vartheta_\varepsilon; \tag{5.3}$$

- L_ε: wire length at stereo angle ε

$$L_\varepsilon = \frac{L_0}{\cos\varepsilon}; \tag{5.4}$$

- ΔY_ε: excess wire (helical pitch- wire length) (Figure 5.7)

$$\Delta Y_\varepsilon = 2\pi\sqrt{r_c^2 + \left(\frac{p_\varepsilon}{2\pi}\right)^2} + p\left(\sin\varepsilon - \frac{p_\varepsilon}{2\pi r_c}\cos\varepsilon\right) - L_\varepsilon; \tag{5.5}$$

- ΔX: gap between US wire PCB and DS wire PCB (Figure 5.7)

$$\Delta X = \Delta Y_\varepsilon \cos\varepsilon; \tag{5.6}$$

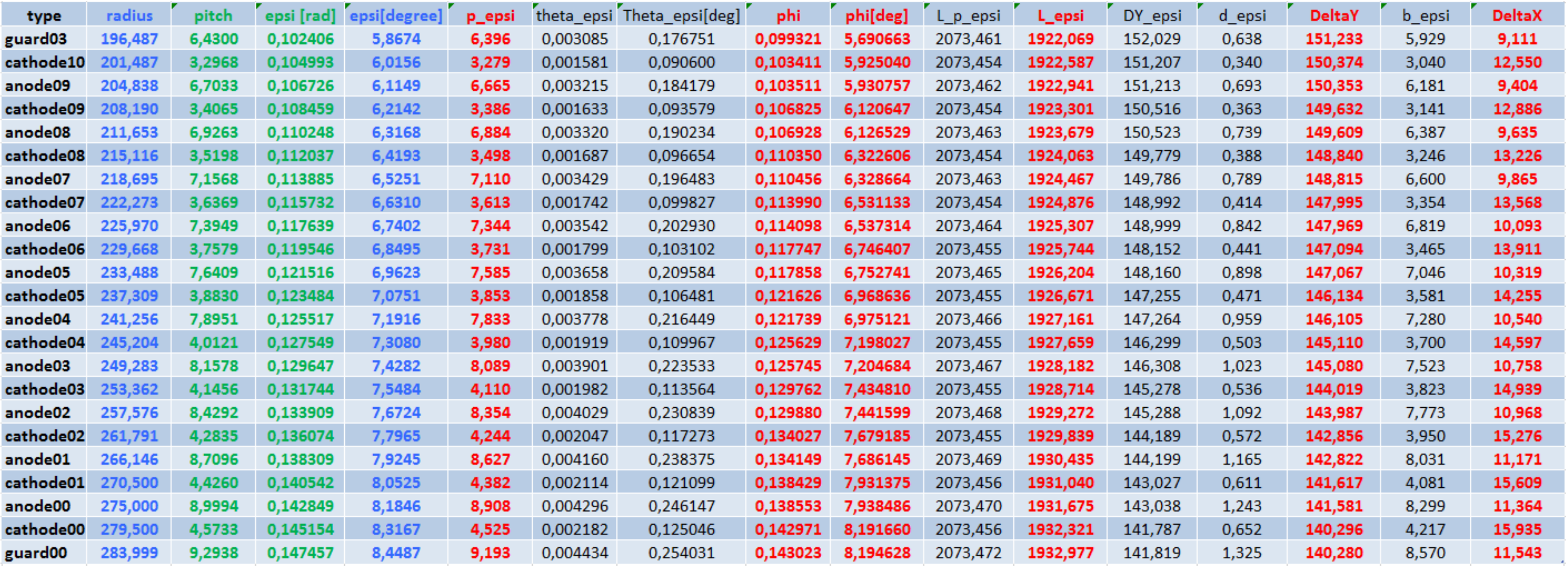

type	radius	pitch	epsi [rad]	epsi[degree]	p_epsi	theta_epsi	Theta_epsi[deg]	phi	phi[deg]	L_p_epsi	L_epsi	DY_epsi	d_epsi	DeltaY	b_epsi	DeltaX
guard03	196,487	6,4300	0,102406	5,8674	6,396	0,003085	0,176751	0,099321	5,690663	2073,461	1922,069	152,029	0,638	151,233	5,929	9,111
cathode10	201,487	3,2968	0,104993	6,0156	3,279	0,001581	0,090600	0,103411	5,925040	2073,454	1922,587	151,207	0,340	150,374	3,040	12,550
anode09	204,838	6,7033	0,106726	6,1149	6,665	0,003215	0,184179	0,103511	5,930757	2073,462	1922,941	151,213	0,693	150,353	6,181	9,404
cathode09	208,190	3,4065	0,108459	6,2142	3,386	0,001633	0,093579	0,106825	6,120647	2073,454	1923,301	150,516	0,363	149,632	3,141	12,886
anode08	211,653	6,9263	0,110248	6,3168	6,884	0,003320	0,190234	0,106928	6,126529	2073,463	1923,679	150,523	0,739	149,609	6,387	9,635
cathode08	215,116	3,5198	0,112037	6,4193	3,498	0,001687	0,096654	0,110350	6,322606	2073,454	1924,063	149,779	0,388	148,840	3,246	13,226
anode07	218,695	7,1568	0,113885	6,5251	7,110	0,003429	0,196483	0,110456	6,328664	2073,463	1924,467	149,786	0,789	148,815	6,600	9,865
cathode07	222,273	3,6369	0,115732	6,6310	3,613	0,001742	0,099827	0,113990	6,531133	2073,454	1924,876	148,992	0,414	147,995	3,354	13,568
anode06	225,970	7,3949	0,117639	6,7402	7,344	0,003542	0,202930	0,114098	6,537314	2073,464	1925,307	148,999	0,842	147,969	6,819	10,093
cathode06	229,668	3,7579	0,119546	6,8495	3,731	0,001799	0,103102	0,117747	6,746407	2073,455	1925,744	148,152	0,441	147,094	3,465	13,911
anode05	233,488	7,6409	0,121516	6,9623	7,585	0,003658	0,209584	0,117858	6,752741	2073,465	1926,204	148,160	0,898	147,067	7,046	10,319
cathode05	237,309	3,8830	0,123484	7,0751	3,853	0,001858	0,106481	0,121626	6,968636	2073,455	1926,671	147,255	0,471	146,134	3,581	14,255
anode04	241,256	7,8951	0,125517	7,1916	7,833	0,003778	0,216449	0,121739	6,975121	2073,466	1927,161	147,264	0,959	146,105	7,280	10,540
cathode04	245,204	4,0121	0,127549	7,3080	3,980	0,001919	0,109967	0,125629	7,198027	2073,455	1927,659	146,299	0,503	145,110	3,700	14,597
anode03	249,283	8,1578	0,129647	7,4282	8,089	0,003901	0,223533	0,125745	7,204684	2073,467	1928,182	146,308	1,023	145,080	7,523	10,758
cathode03	253,362	4,1456	0,131744	7,5484	4,110	0,001982	0,113564	0,129762	7,434810	2073,455	1928,714	145,278	0,536	144,019	3,823	14,939
anode02	257,576	8,4292	0,133909	7,6724	8,354	0,004029	0,230839	0,129880	7,441599	2073,468	1929,272	145,288	1,092	143,987	7,773	10,968
cathode02	261,791	4,2835	0,136074	7,7965	4,244	0,002047	0,117273	0,134027	7,679185	2073,455	1929,839	144,189	0,572	142,856	3,950	15,276
anode01	266,146	8,7096	0,138309	7,9245	8,627	0,004160	0,238375	0,134149	7,686145	2073,469	1930,435	144,199	1,165	142,822	8,031	11,171
cathode01	270,500	4,4260	0,140542	8,0525	4,382	0,002114	0,121099	0,138429	7,931375	2073,456	1931,040	143,027	0,611	141,617	4,081	15,609
anode00	275,000	8,9994	0,142849	8,1846	8,908	0,004296	0,246147	0,138553	7,938486	2073,470	1931,675	143,038	1,243	141,581	8,299	11,364
cathode00	279,500	4,5733	0,145154	8,3167	4,525	0,002182	0,125046	0,142971	8,191660	2073,456	1932,321	141,787	0,652	140,296	4,217	15,935
guard00	283,999	9,2938	0,147457	8,4487	9,193	0,004434	0,254031	0,143023	8,194628	2073,472	1932,977	141,819	1,325	140,280	8,570	11,543

Figure 5.6: the parameter table for the different layers.

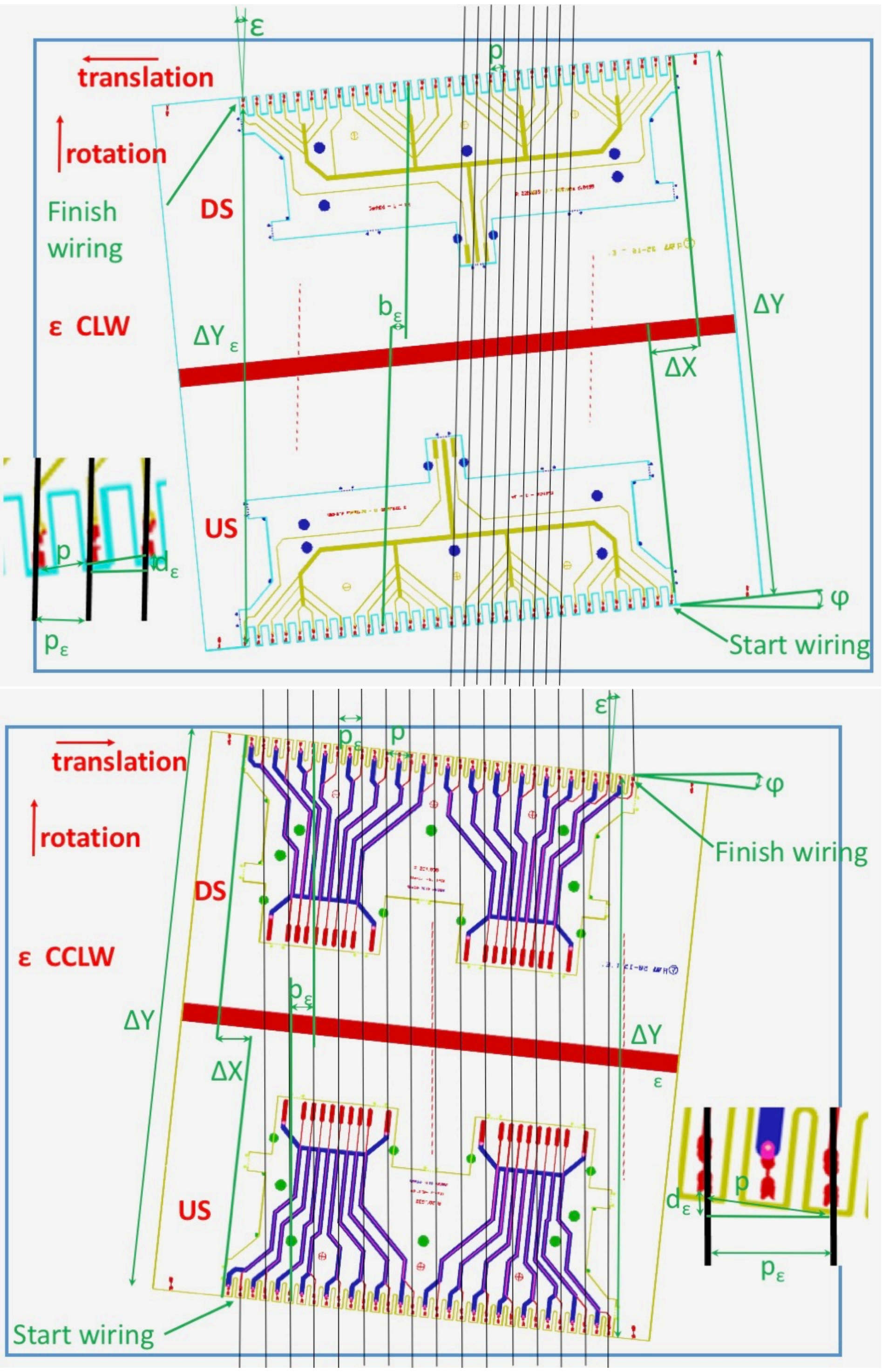

Figure 5.7: Schematic of the parameters necessary to the wiring robot for positive angle stereo (Top) and negative angle stereo (Bottom).

- b_ε: helix increment (Figure 5.7)

$$b_\varepsilon = p \cos\varphi - \Delta Y_\varepsilon \cos\vartheta_\varepsilon; \tag{5.7}$$

- ΔY: distance between the pad lines of the two wire PCBs (Figure 5.7)

$$\Delta Y = \Delta X \tan \varphi - \frac{b_\varepsilon}{\cos \varphi}; \tag{5.8}$$

- d_ε: azimuthal distance between two pads of the same side

$$d_\varepsilon = \frac{p \sin \varphi}{\cos \vartheta_\varepsilon}; \tag{5.9}$$

As mentioned earlier, in the CDCH there are two views (U and V), for this reason there are two wiring directions, the first from right to left (φ and ε are positive (clockwise)) and the second from left to right (φ and ε are negative (counter clockwise)). In both cases, the direction of rotation of the cylinder is unique.

5.4 Wiring robot

The CDCH construction is carried out using a semi-automatic system, called wiring robot, especially designed in the laboratories of the University of Salento and INFN Lecce. The wiring robot is required to manage the positioning of a large quantity of wires with precise alignment and mechanical tension. The system is composed of three subsystems:

1. the wiring system;
2. the soldering system;
3. the extraction system;

Figure 5.8 shows an overall view of the wiring robot. In this section, the three systems will be described in detail, justifying some choices made.

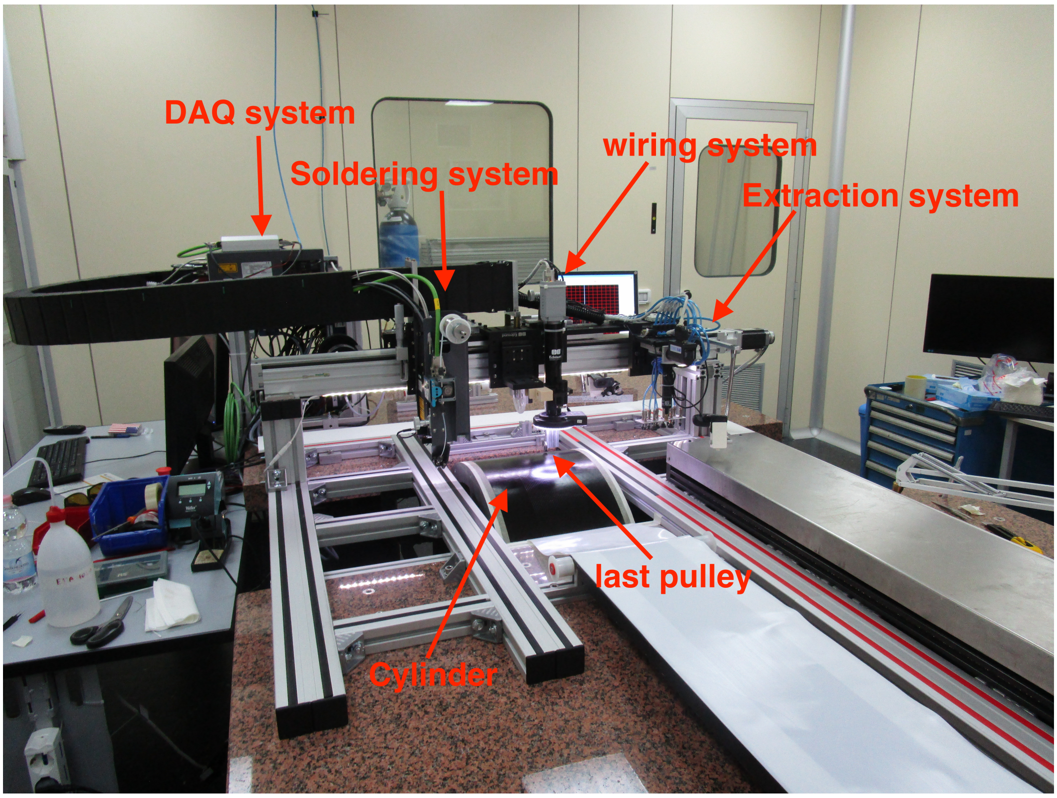

Figure 5.8: Wiring robot.

5.4.1 The wiring system

The wiring system has the task of distributing the wire along a helicoidal trajectory with high precision and with a constant pre-defined mechanical tension. To this purpose, a linear axis and a rotating cylinder are used. The linear axis (main axis) hosts the wire spool holder, co-axial with a torsiometer and an electromagnetic brake. The wire from the spool is fed through a pulley system to the cylinder. The helicoidal trajectory is obtained by synchronizing the main axis with the rotation of the cylinder, unwinding the wire from the spool.

Rotating Cylinder

The rotating cylinder, made of fiber glass, with 658 mm diameter and 300 mm length is coupled to Al spokes (Figure 5.9: Left). A section parallel to the cylinder axis (Figure 5.9: Right) has been replaced with an Al hump which is used as a support for the wire PCBs. A rubber layer covers the cylinder external surface to avoid wire slipping during the wiring process. The final diameter is 660.2 mm, the exact value necessary to wire the MEGII CDCH.

The cylinder axis is coupled through ball-bearings to a stepper motor controlled with National Instruments CompactRIO (cRIO) [58].

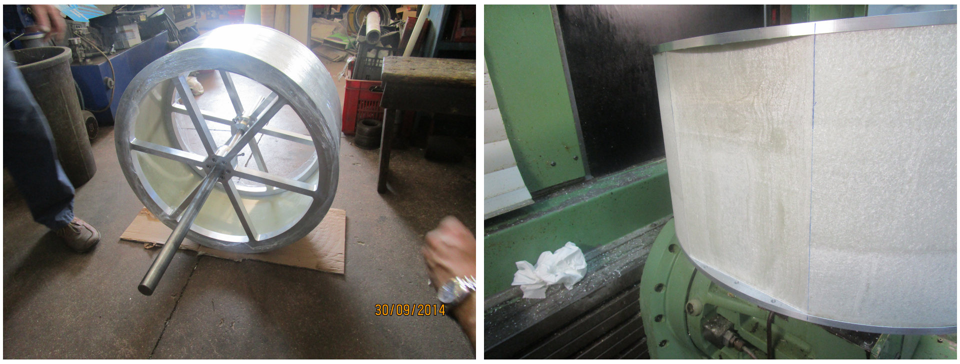

Figure 5.9: The cylinder in the different processing phases. The cylinder coupled with the spokes (Left). Finished cylinder (Right).

Due to the load distribution, the cylinder results unbalanced, mainly because of the aluminum hump, causing a non-uniform tension distribution along the wire. In order to compensate the effect of the unbalance some additional weights have been added at the inner cylinder surface, with the help of a torsiometer (MAGTROL TM 300 [67]) mounted on the axis of the cylinder, Figure 5.10 shows the calibration curve of the torsiometer and Figure 5.11 represents the torque vs the rotation phase of cylinder, revealing an unbalance of about ±90 g with an offset of ~30°.

Figure 5.12 shows the result of the addition of weights at the indicated offset angles. The residual unbalance is about 17.82 g.

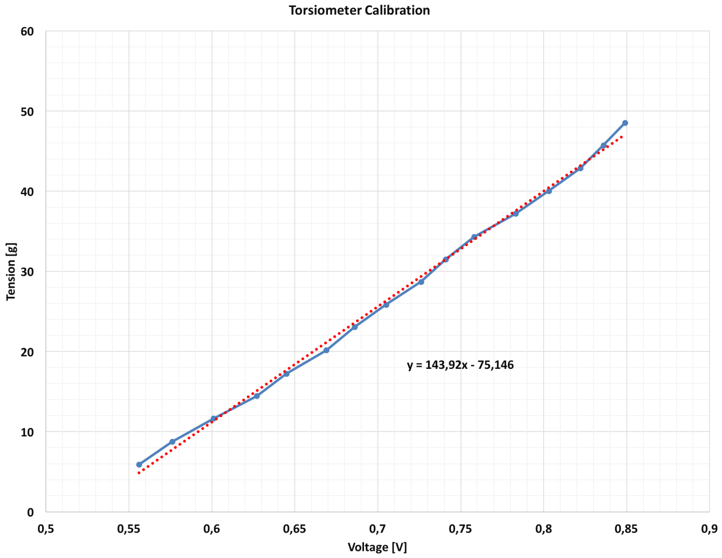

Figure 5.10: Torsiometer calibration curve

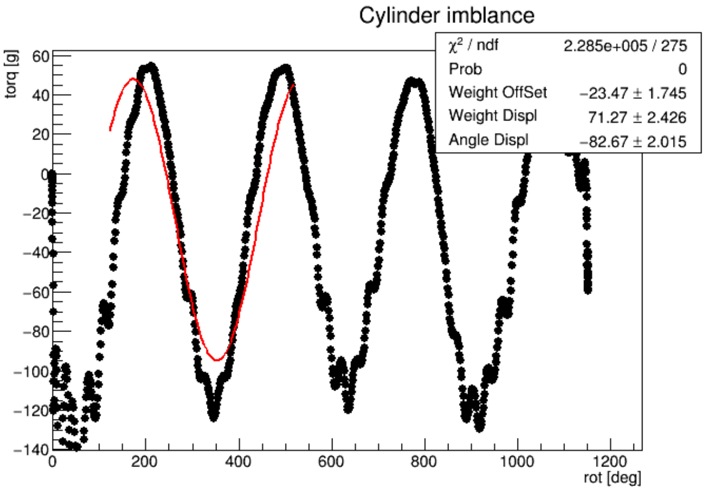

Figure 5.11: Torque vs angular position with the unbalanced cylinder

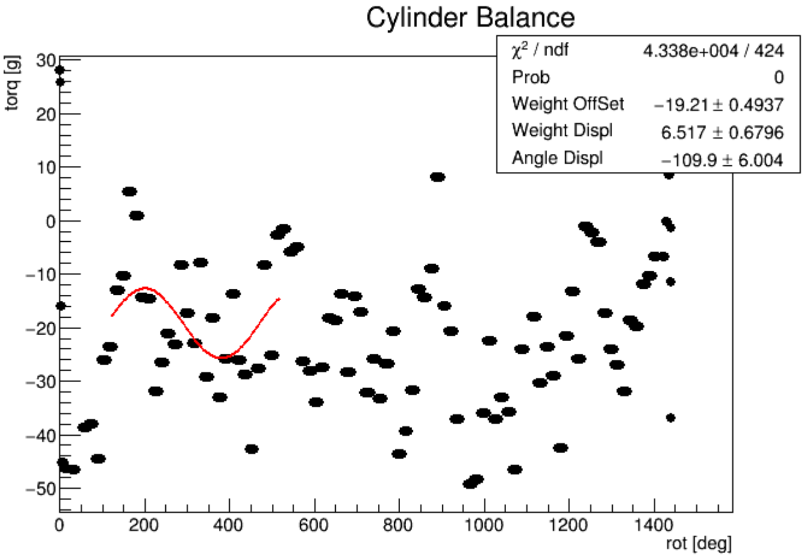

Figure 5.12: Torque vs angular position after balancing.

Wire spool holder

The wire spool holder (Figure 5.13) is composed of a torsiometer (ETH messtechnik DRFL-VIII [76]) and an electromagnetic brake-clutch (Magtrol HCF-8M [66]) co-axially connected. The first element is only used to obtain further check of the mechanical tension applied, while the latter is used to set the mechanical tension of the wire through a feedback system which will be described in the next sections.
The DRFL-VIII Torsiometer gives a voltage as output signal ranging between 0 V and 10 V proportional to the torque in the range 0-0.5 Nm. The torsiometer output has been connected to the DAQ system (described in the following sections). The

HCF-8M brake-clutch is controlled in current by means of a current-regulated power supply (Magtrol 5210 [68]), the power supply is connected and controlled directly from the DAQ system with a voltage signal.

Figure 5.14 shows the calibration curve for the electromagnetic brake, highlighting presence of hysteresis.

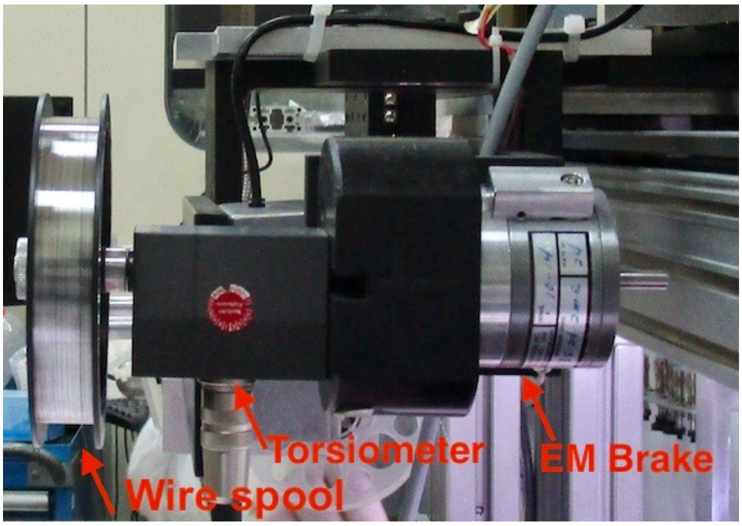

Figure 5.13: Wire spool holder

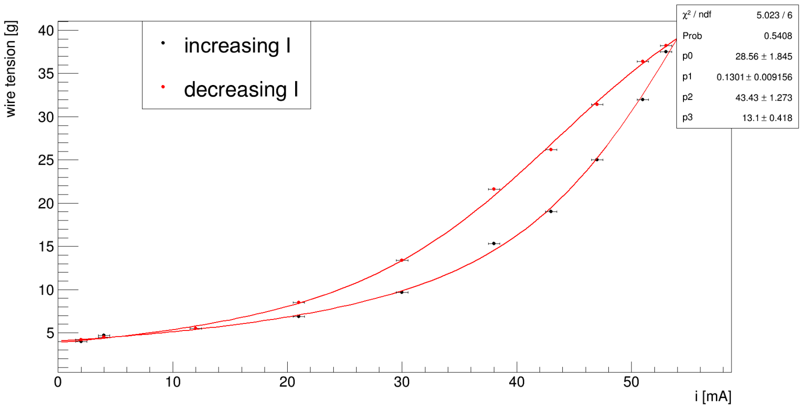

Figure 5.14: Calibration curve of the electromagnetic brake

Pulley system

The pulley system guides the wire from the wire spool to the rotating cylinder, avoiding sharp bends which may damage the wire. It consists of 6 pulleys mounted on the main axis with ball bearings (see Figure 5.15): three of these are used to drive the wire, while the others are used to measure the wire mechanical tension during the wiring whith the central one connected to a strain gauge (Micro Load Cell

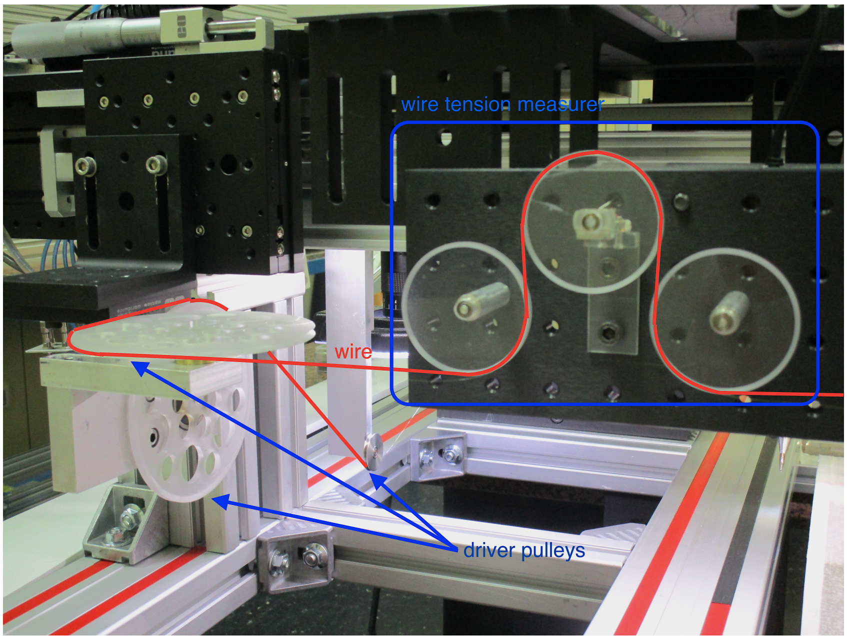

Figure 5.15: Pulley system. In red the wire path is depicted.

CZL639HD [87]) which measures in the range from 0 g to 100 g with a sensitivity of 50 mg. Its output signal is connected to the DAQ System with a Wheatstone bridge and an amplifier (Phidgets 1046 [88]). Figure 5.16: Bottom shows the calibration curve for the strain gauge.

A digital camera PIXELINK PL-B776 [90] controls the wire alignment during the wiring phase.

Wire tension feedback

The wire tension is controlled by a feedback system implemented in the DAQ system, using the eletromagnetic brake and the strain gauge.

As can be seen in Figure 5.17, the strain gauge is mounted on the top pulley which is aligned with the other two and, therefore, measures twice the wire tension. During the wiring phase, the DAQ system acquires, at a rate of 24 measures/ms, the wire mechanical tension and carries out a smoothing using a FIR filter moving average every 100 sample, corresponding to 0,5 mm of unwound wire (at the wiring speed of 12.5 cm/s).

To ensure a constant wire tension throughout a multi-wire plane (16 or 32 wires)

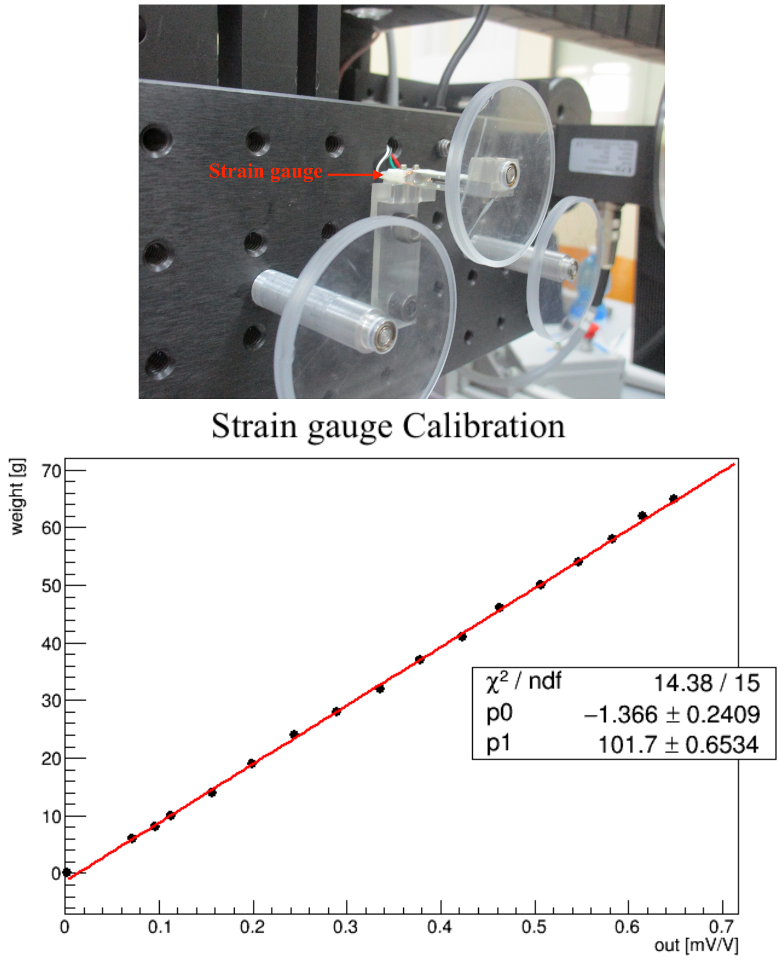

Figure 5.16: Top: Strain gauge mounted on pulley. Bottom: Calibration curve of the strain gauge

one additional wire is wound during the acceleration phase of the rotating cylinder before reaching a stable value of tension and one during the deceleration at the completion of the wiring phase.

The DAQ system initially sets the voltage to the electromagnetic brake by performing a spline interpolation of the increasing curve shown in Figure 5.18. After the cylinder has reached constant speed and the wire mechanical tension is at the set value, the feedback system reads the wire tension through the strain gauge and compares it with the one of the setpoint voltage.

The feedback correction is applied by interpolating the data set points of Figure 5.18, red points, to decrease the wire tension, black points to increase it.

In Figure 5.19 is plotted the wire mechanical tension without feedback correction (Top), with a fixed brake voltage (Center) and with the activated feedback (Bottom). From Figure 5.19 it is evident that a residual oscillation of ±0.35 g around a very

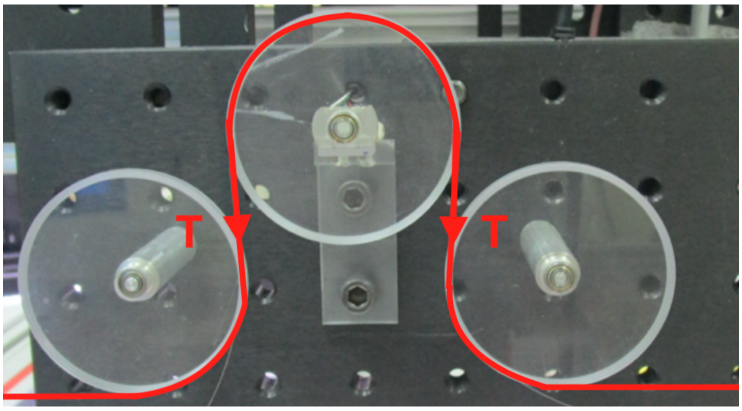

Figure 5.17: Wire tension measuring system. In red the wire path is depicted.

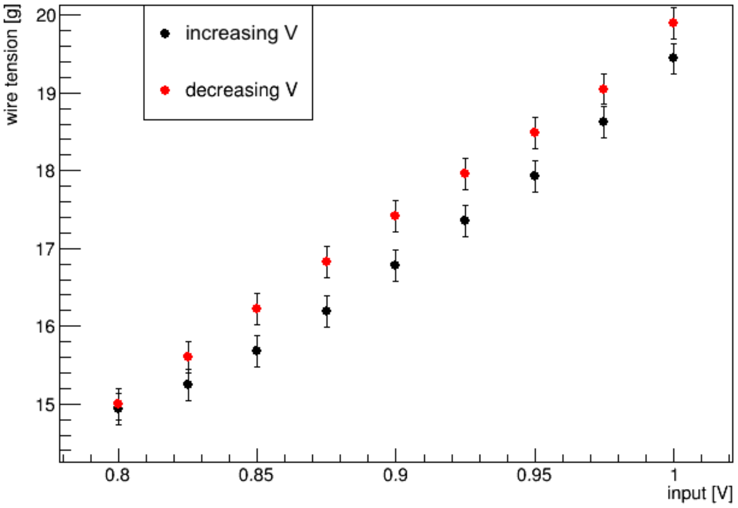

Figure 5.18: Curves used for the feedback system between the brake and strain gauge.

stable fixed value of 16.8 g remains to be corrected. The number of oscillation in one full turn of the cylinder (∼7) indicates a period of about 30 cm on the wire, suggesting that these may be due to an off-center of the wire spool, the diameter of which is about 10 cm. However, the systematic difference in tension between two adjacent wires can be at most one oscillation out of 7 and, therefore: 0.35 g/7=0.005 g.

5.4.2 The soldering system

Each wire is fixed at both ends on the pads of the wire PCB, while still constrained around the rotating cylinder under its own tension. The soldering phase is accomplished by an IR laser soldering system (LASCON Hybrid with a solder wire

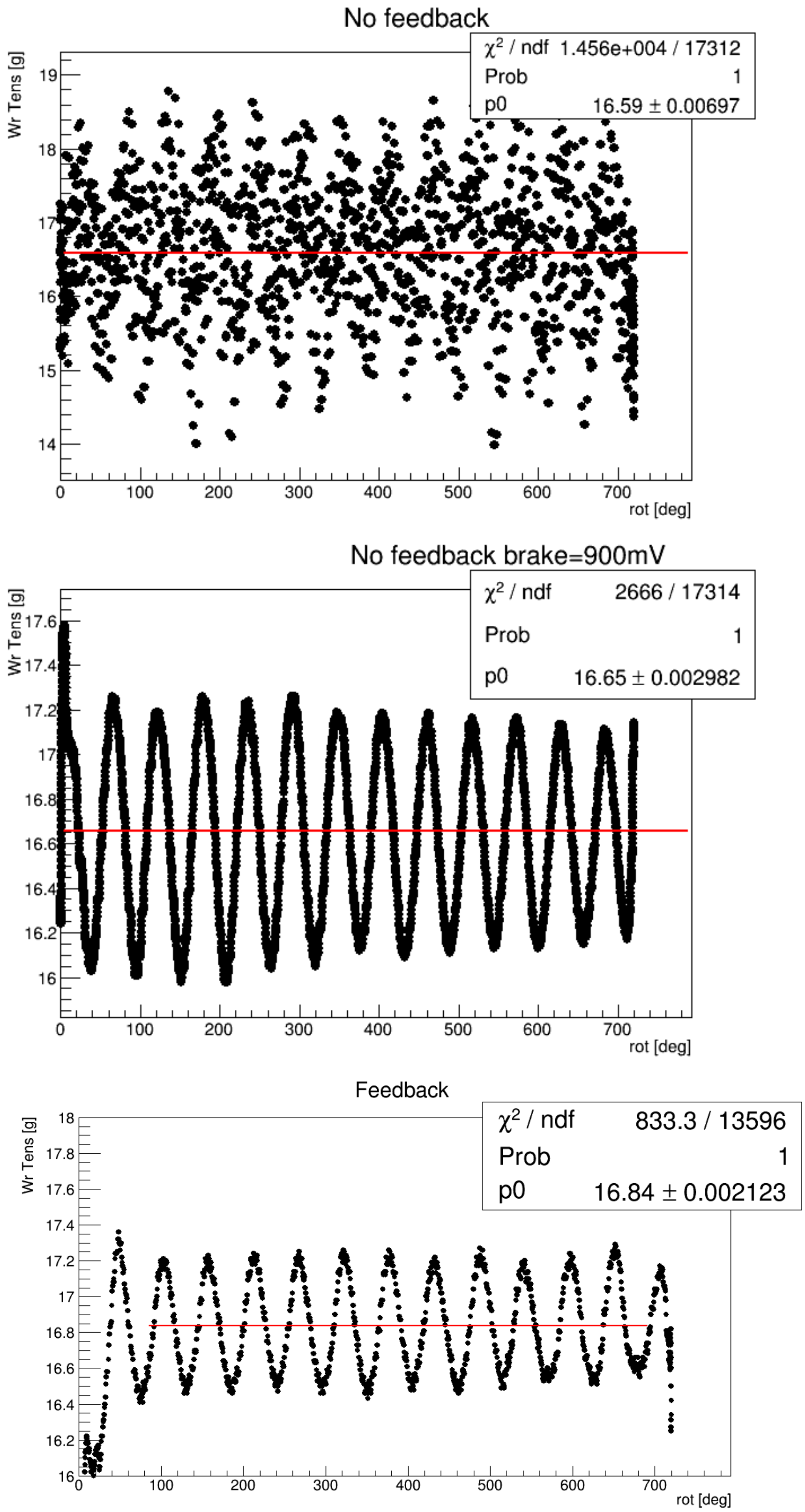

Figure 5.19: The mechanical tension of the wire without feedback (Top), with the brake fixed voltage (Center) and with the active feedback (Bottom)

feeder [63]) consisting of a solder wire feeder, a 68 W IR laser, a pyrometer and a digital camera, as shown in Figure 5.20. The last three elements are assembled in a single block and share the same focal length. The digital camera allows to see in real time the soldering operations and the pyrometer monitors the temperature at the laser focus.

The movement of the laser system and its operations are controlled by the DAQ system. In particular, the laser system is synchronized with the positioning system (cylinder and main axis) by using a pattern matching software developed with LabVIEW program[1] [57] to localize the soldering pad. All the soldering parameters (temperature, soldering time, solder wire length and feeding speed) are defined in order not to cause any damages to the wires through a proper Laser script embedded in LabVIEW. In Figure 5.21 the variation of the parameters during the soldering phase are shown.

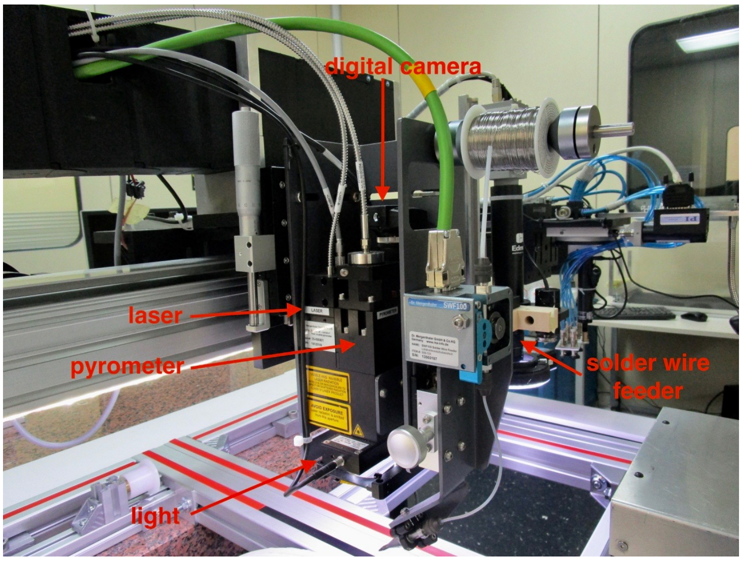

Figure 5.20: Laser system.

The solder wire used has a low melting point of 160 °C to avoid damages to the wire Ag plating and low outgassing in order not to contaminate the CDCH gas during the data taking.

---

[1] LabVIEW is the programming language used for the DAQ

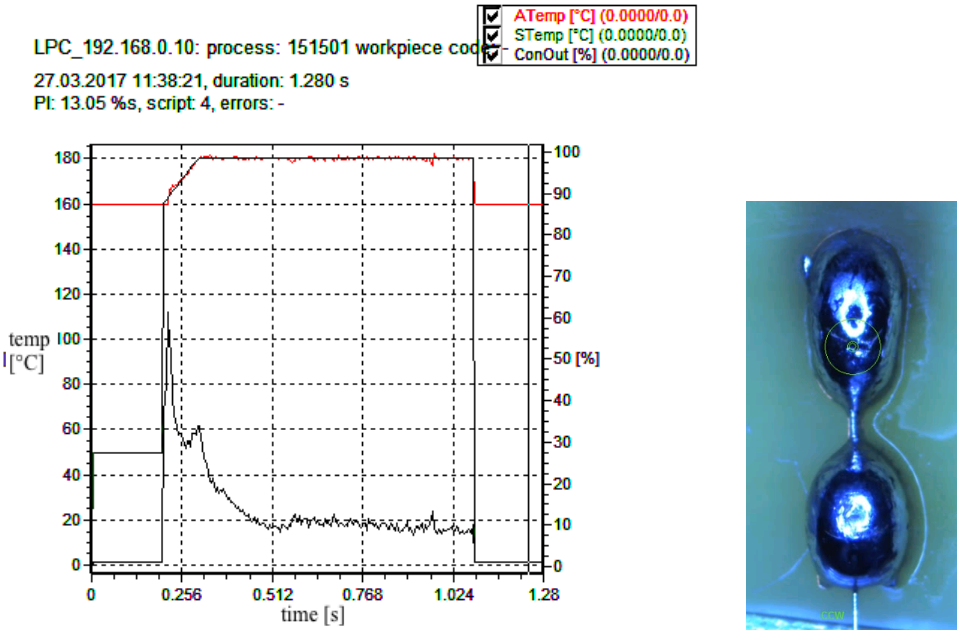

Figure 5.21: The laser spot temperature (red line), the pyrometer value (green line) and of the laser during a soldering (Left) and a solder photo (Right).

5.4.3 The extraction system

The extraction system enables to unroll and de-tension the wound layer of soldered wires around the cylinder. The extraction system (see Figure 5.22) is constituted by:

- a linear actuator (Zaber T-LA60 [103]);
- a rotation slide (PI C-663 [89]);
- a plate with suction cups;
- a vacuum system (SMC ZK2 [96]);
- a linear axis.

The first two elements aligned with the positioning system are used to place the suction cups plates on the US wire PCB; the vacuum system to release the wire PCB from the rotating cylinder and the linear axis to unroll the multi-wire plane. The whole system is controlled by the DAQ.

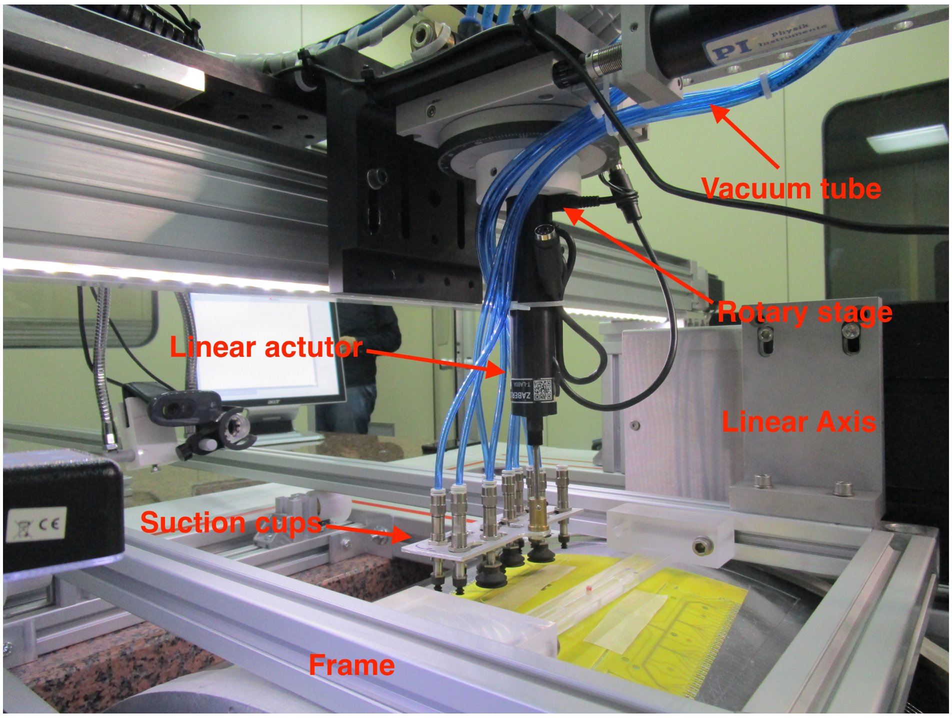

Figure 5.22: Extract system.

In order to extract the multi-layer wire. The long helicoidal wire is cut between the soldering pads. Then the US wire PCB is lifted off from the cylinder surface (see Figure 5.24) with the vacuum activated suction cups and placed on the transport frame (Figure 5.23). The unrolling is accomplished by synchronizing the cylinder rotation with the linear displacement of the frame carried out with the linear axis. Once the layer of soldered wires is completely unrolled, the DS wire PCB is lifted off from the cylinder, as the US one, and placed on the other end of the transport frame (Figure 5.23). The US and DS wire PCB supports are made of plexiglass and they are dedicated to hold the wire PCBs at correct positions by means of teflon screws. The US support is fixed to the frame, whereas the DS support is free to slide in the frame by means of threaded rod thus adjusting the length of the wires and, therefore, their tension.

Figure 5.23: The trasport frame with the different support.

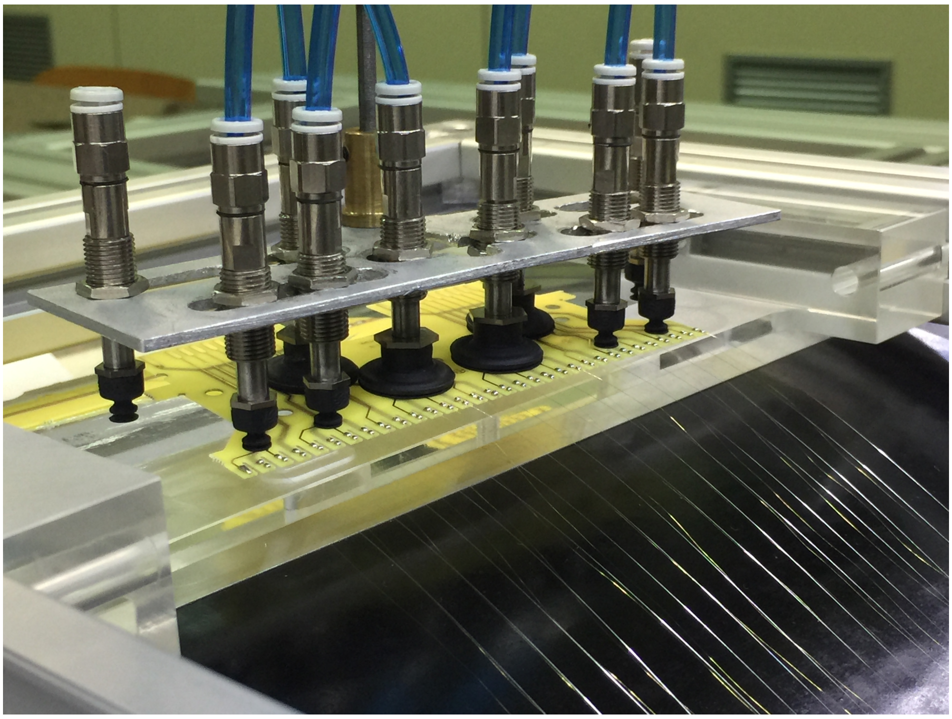

Figure 5.24: The US wire PCB is lifted off from the cylinder surface.

5.5 DAQ system

The DAQ system must monitor and accurately synchronize all the systems described in the previous sections. A real-time controller from National Instrument with several add-on modules, as described in the next section, has been chosen to perform this task and to allow the use of LabVIEW to develop the control software, highly integrated to the hardware components.

5.5.1 DAQ Hardware

The hardware of the DAQ system (see Figure 5.25) is the Real-Time PowerPC Controller NI cRIO-9024®and the chassis NI cRIO-9112®, as shown in Figure 5.26. The chassis allows the parallel communication of several additional modules. The installed add-on modules [56] are:

- 4 NI 9512®Axis Stepper Drive Interface;
- 1 NI 9207®Voltage/Current Analog Input with 24-bit resolution;

- 1 NI 9264®Analog Output Voltage 1 NI 9381®Multifunction I / O Module

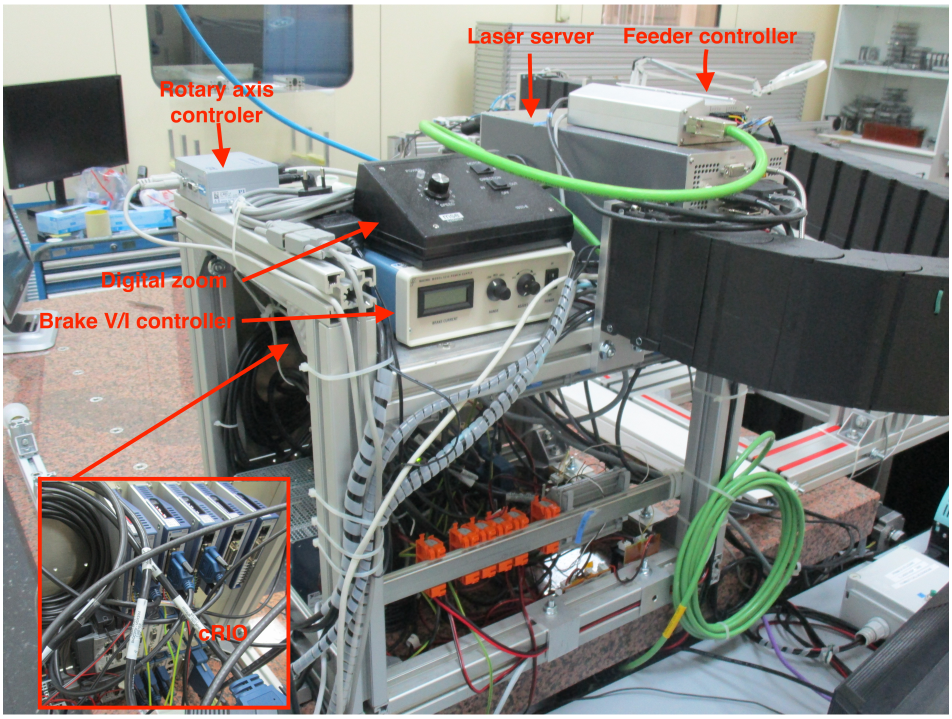

Figure 5.25: DAQ system.

Figure 5.26: cRIO Controller with chassis and modules.

These modules are used to connect the different elements constituting the wiring robot. In particular, the NI 9512®modules are used to control the various axes (main axis and extraction axis) and the rotating cylinder. The I/O modules are used to send commands to the soldering system, to read the torsiometer, to set the voltage to the electromagnetic brake, to activate the vacuum suction cups.

The soldering system has its own management server, to which the cRIO and the PC are connected, respectively, with additional modules and ethernet cable. At the beginning of operation, the laser server performs calibration and communicates with the controller to set the parameters. All other elements (linear actuator, rotary slide, strain gauge, digital cameras) are directly connected to the control PC and synchronized with the controller using LabVIEW.

5.5.2 DAQ Software

The DAQ software is developed entirely in LabVIEW® [57]. To perform the correct synchronization of the various elements, the specific modules developed by National Instrument as NI SoftMotion®for the management of movements or NI Vision®for the management of the digital camera are used.

Figure 5.27 shows the main screen of the software for the management of the movements determined by the operator and the different steps for winding a multi-wire plane. At startup of the software, input is required, regarding the type of layer and other information, as shown in Figure 5.28. The software performs some SQL query on the wiring database to get all the layer parameters and writes information about the operators, then asks.

The operators move the wiring system in the home position (the central reference marker of the UP wire PCB), so that the software can calculate the positions of all the pads. In Figure 5.29 and Figure 5.30 the graphic interfaces for the management of the soldering and for the extraction system are shown. After performing the extraction and receiving the confirmation by the operator that the multi-wire plane is accepted, the software updates the Data Base (DB) with the multi-wire plane product information including the graphs of the mechanical tension of the thread

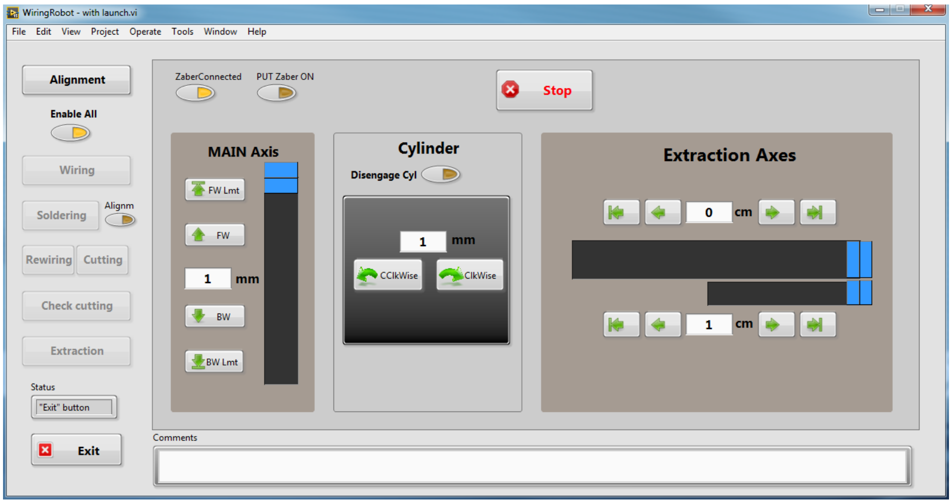

Figure 5.27: The main screen of the software.

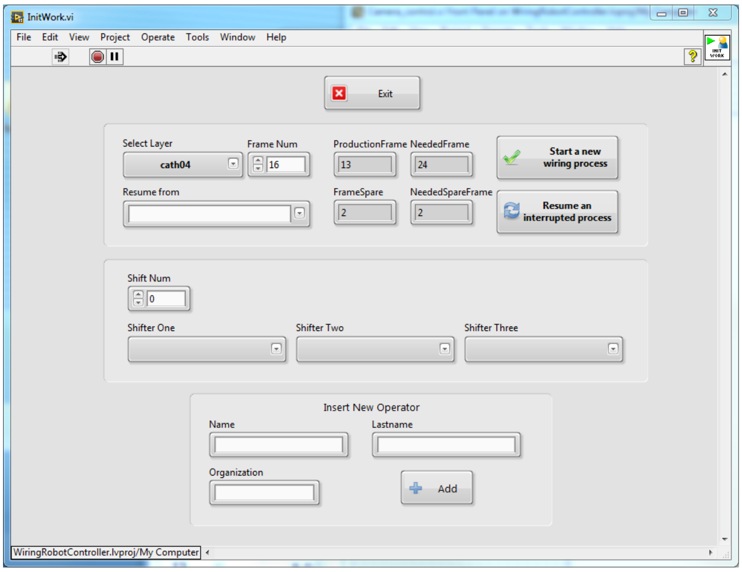

Select Layer: cath04
Frame Num: 16
ProductionFrame: 13
NeededFrame: 24
Resume from:
FrameSpare: 2
NeededSpareFrame: 2
Shift Num: 0
Shifter One:
Shifter Two:
Shifter Three:

Figure 5.28: The software screen to enter the frame information.

in several turns, extrapolated with a root macro. Figure 5.31 shows the diagram Entity/Relationship (E/R) of the DB with the various fields.

The different phases for the production of a multi-wire plane are described in the next chapter.

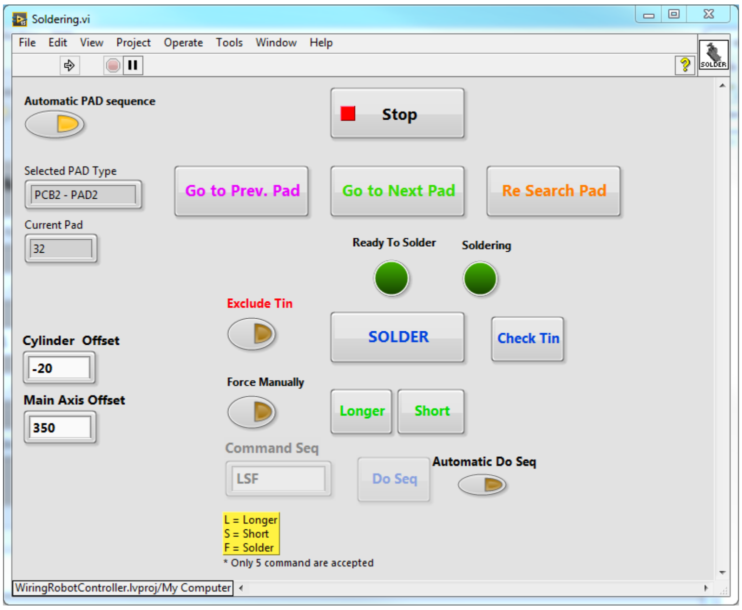

Selected PAD Type: PCB2 - PAD2
Current Pad: 32
Cylinder Offset: -20
Main Axis Offset: 350
Command Seq: LSF

L = Longer
S = Short
F = Solder
* Only 5 command are accepted

Figure 5.29: The graphic interfaces for the management of the soldering system.

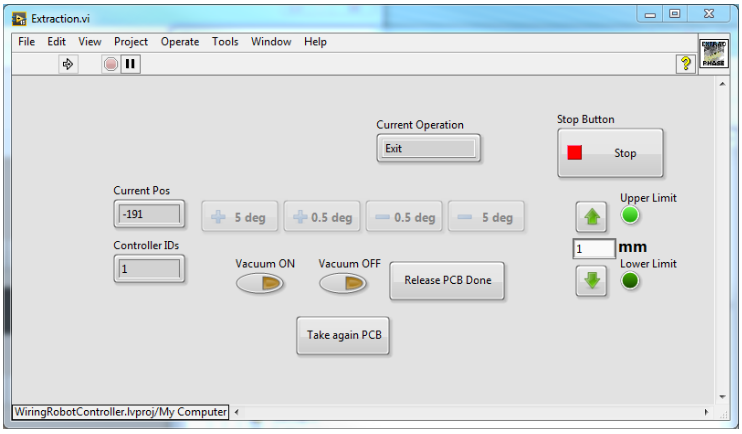

Current Operation: Exit

Current Pos: -191

Controller IDs: 1

1 mm

WiringRobotController.lvproj/My Computer

Figure 5.30: he graphic interfaces for the management of the extraction system.

5.6 Conclusion

In this chapter the wiring robot in its different parts has been described. It is used for the construction of multi-wire plane that compose the CDCH. In the next chapter we will see the steps for the construction of a multi-wire plane and the assembly on the final structure of the CDCH.

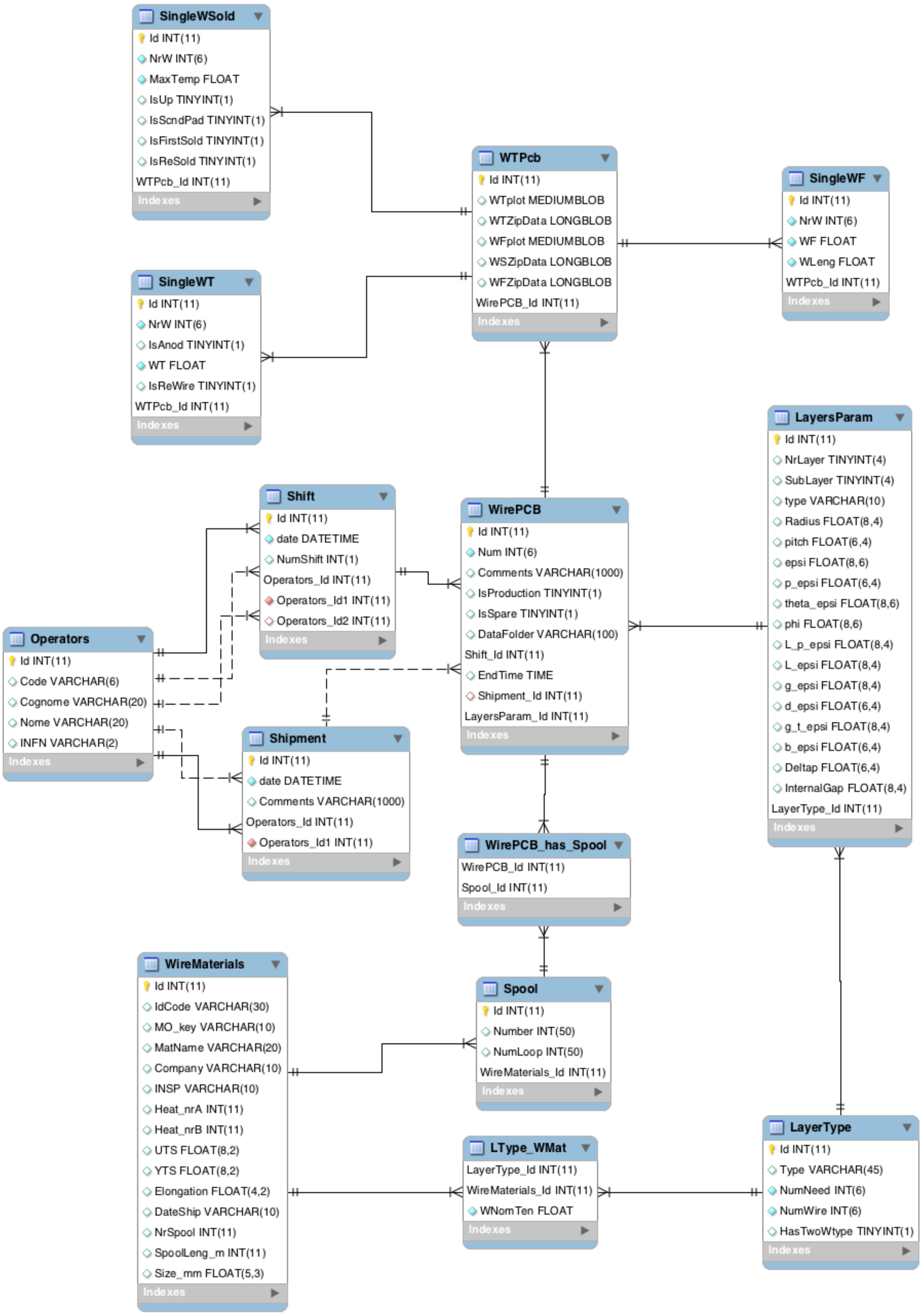

Figure 5.31: Diagram E/R of the DB.

6

CDCH construction

This Chapter deals with the construction of the MEG II CDCH illustrating the wiring of a multi-wire plane with the wiring robot described in Chapter 5. The different stages to produce a the plane, the methods for testing the quality of the produced plane and its assembly on the end-plates are described.

6.1 Wiring of the multi-wires plane

The wiring of a multi-wire plane is carried out in several steps, identical for all layers independently of the variation of the geometrical parameters (stereo angle, radius, pitch). All the operations of wiring are done in a clean room at the INFN Lecce and University of Salento, this is a necessary condition to prevent damage of the wires due to the environmental conditions (see Appendix 8). This section is dedicated to the description of the different steps

6.1.1 Template for the wire PCBs

In order to standardize the wiring phase for all layer types and facilitate the positioning of the wire PCBs on the rotating cylinder (Figure 6.1: Left), a template, based on the geometric parameters has been used for each layer.

The template is formed by two identical aluminum trapezes 300 μm thick(Figure 6.1: Right), which are mounted on the aluminum hump of the cylinder (Figure 6.1: Right). The dimensions are calculated according to the dimensions of the wire PCB and the angle φ, as illustrated in Figure 6.3.

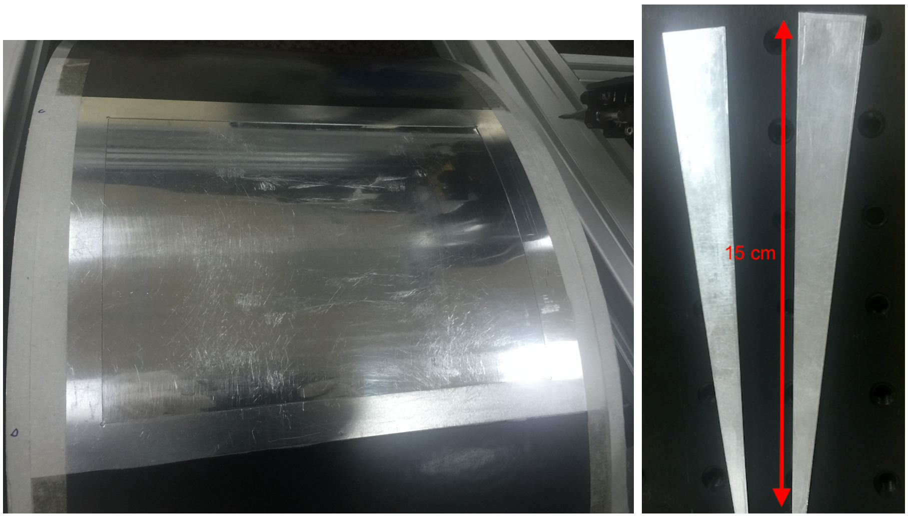

Figure 6.1: Left: The aluminum hump without template. Right: Trapezes for template.

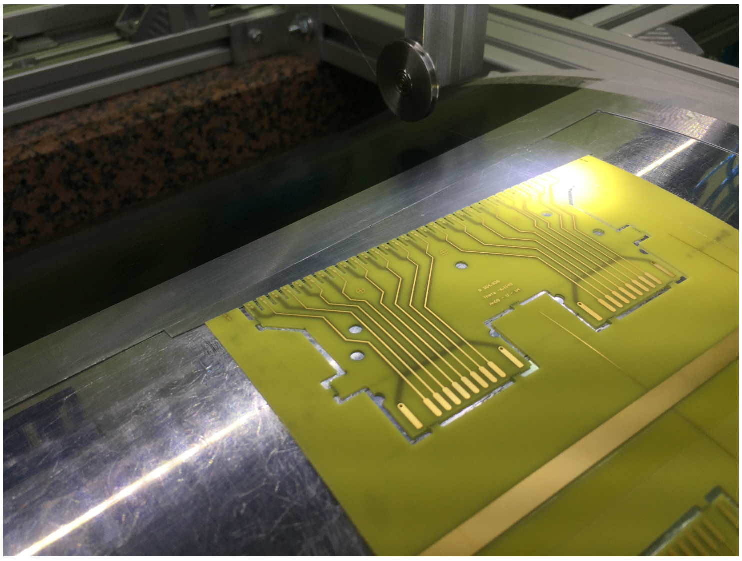

Figure 6.2: Cylinder with trapezes and wire PCBs mounted.

6.1.2 Startup of the wiring

To start the wiring phase, the wire PCB is placed on the rotating cylinder with the side of the pads aligned in contact with the trapezes and the DS and US boards along the direction of rotation.

The operators fill up the information appearing on the control screen, as shown in Figure 5.28. The wiring robot is brought to the home position and all references are reset.

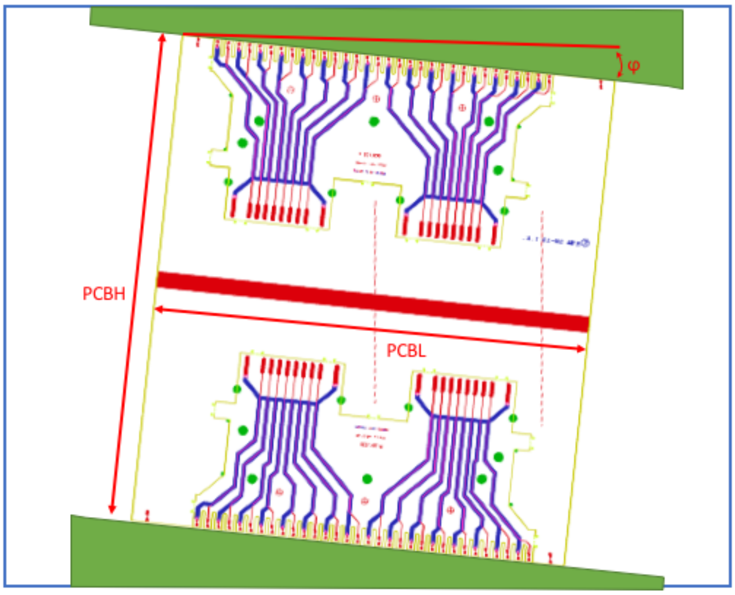

Figure 6.3: Schematic of trapezes (in green) with the geometric parameters of the layer.

6.1.3 Wiring Phase

A 32 wire plane is formed by winding single 32 pitches helicoidal path around the rotating cylinder and over the wire PCB by matching the wire pads. For the anodic layers, composed of alternating sense and field wires, two wiring of 16 wires are carried out in sequence by changing the wire spool according to the software instructions.

At the beginning of the wiring phase, the correct position of the wire PCB is verified with an optical camera by checking that, after a full turn, each pad of the US wire PCB is aligned with the corresponding pad of the DS wire PCB to the desired accuracy ($\pm 20\ \mu$m). If the check fails the positioning of the wire PCB must be repeated. Afterwards, after feeding the wire through the wire distribution system, the tension measuring strain guage is reset at no tension,

As mentioned in the previous chapter, the pitch is set by synchronizing the stepper motors with the cRIO system. The position of the wire is controlled, during the wiring phase, by a digital camera on a linear slide (see Figure 6.4). The accuracy on the position is about 20 μm (see Figure 6.6: Left). The wire mechanical tension is set to a nominal value and monitored by the strain gauge on a screen (Figure 6.5) for the control by the operators.

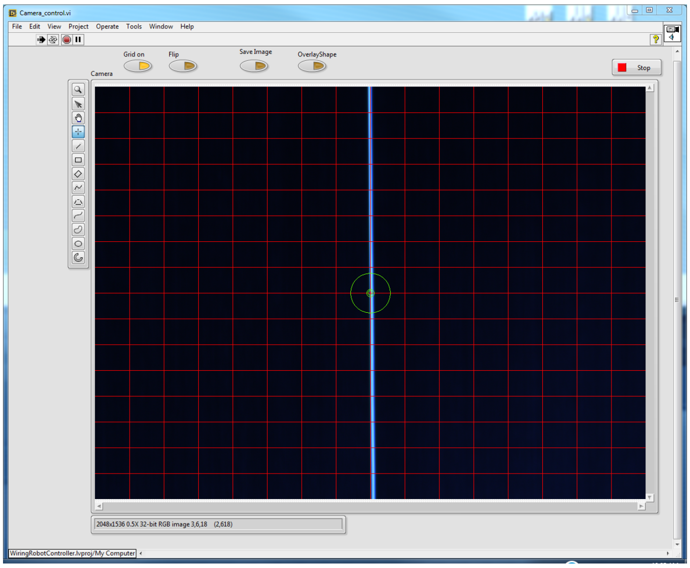

2048x1536 0.5X 32-bit RGB image 3,6,18 (2,618)

WiringRobotController.lvproj/My Computer

Figure 6.4: Diplay the wire during the wiring phase with digital camera

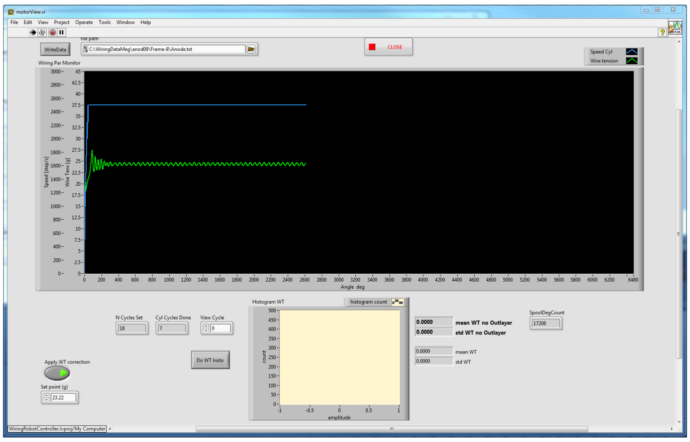

file path: C:\WiringDataMeg\anod09\Frame-8\Anode.txt

N Cycles Set: 18

Cyl Cycles Done: 7

View Cycle: 0

Set point (g): 23.22

mean WT no Outlayer: 0.0000

std WT no Outlayer: 0.0000

mean WT: 0.0000

std WT: 0.0000

SpoolDegCount: 17208

WiringRobotController.lvproj/My Computer

Figure 6.5: Monitor of wire tension and cylinder speed.

The information (the wire tension and torque of the spool torsiometer) are saved and analyzed by a macro root on the DB. Figure 6.7 shows the graphs obtained from the analysis of the wire tension and in Figure 6.6: Right a multi-wire plane wired.

6.1.4 Soldering phase

A mylar strip is placed on the wires next to the soldering pads to protect the wires from possible flux splashes or tin balls during the soldering phase, as shown in Figure 6.8.

The soldering phase (see Figure 6.9) occurs while the wires are still constrained

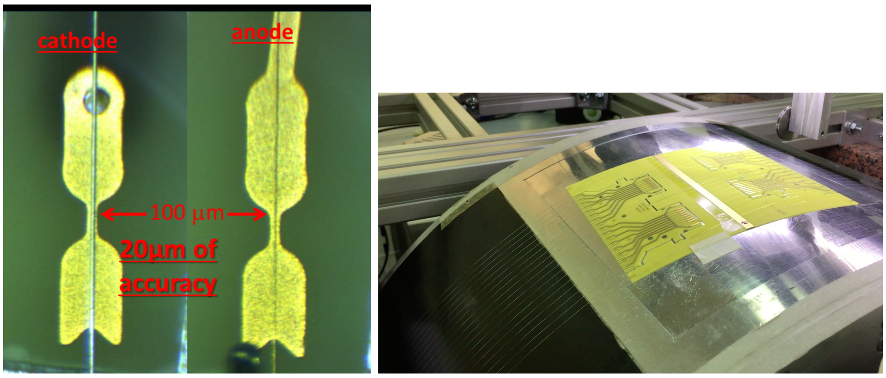

Figure 6.6: Left: Position of the wire on the pad. Right: Multi-wire plane wired.

around the winding cylinder under their own tension. The soldering laser system is controlled by the cRIO and it is synchronized with the positioning system by a pattern matching software (see Figure 6.10) developed with LabVIEW to localize the soldering pad.

All the soldering parameters (temperature, soldering time, solder wire length and feeding speed) are defined to avoid damaging the wires through a proper Laser script, selected by the control software. At the end of the soldering process, all these parameters are transferred from the laser server to the control PC to be analyzed and saved to DB.

6.1.5 Cutting phase

After the soldering phase is completed, the wound multi-wire plane needs to be unrolled from the rotating cylinder and placed on the transport frame during the extraction phase. To this purpose, the excess wire between the wire PCBs must be removed, as shown in Figure 6.11. The wire is cut at the edge of the soldering pads and through a digital camera the operators check that no wire portions stick out of the pad. The cutting phase is the only completely manual operation performed during the wiring process.

6.1.6 Extraction phase

Before unrolling the multi-wire plane from the rotating cylinder, the wire PCBs must be punched out of the FR4 foil to which they were coupled (see Figure 5.2).

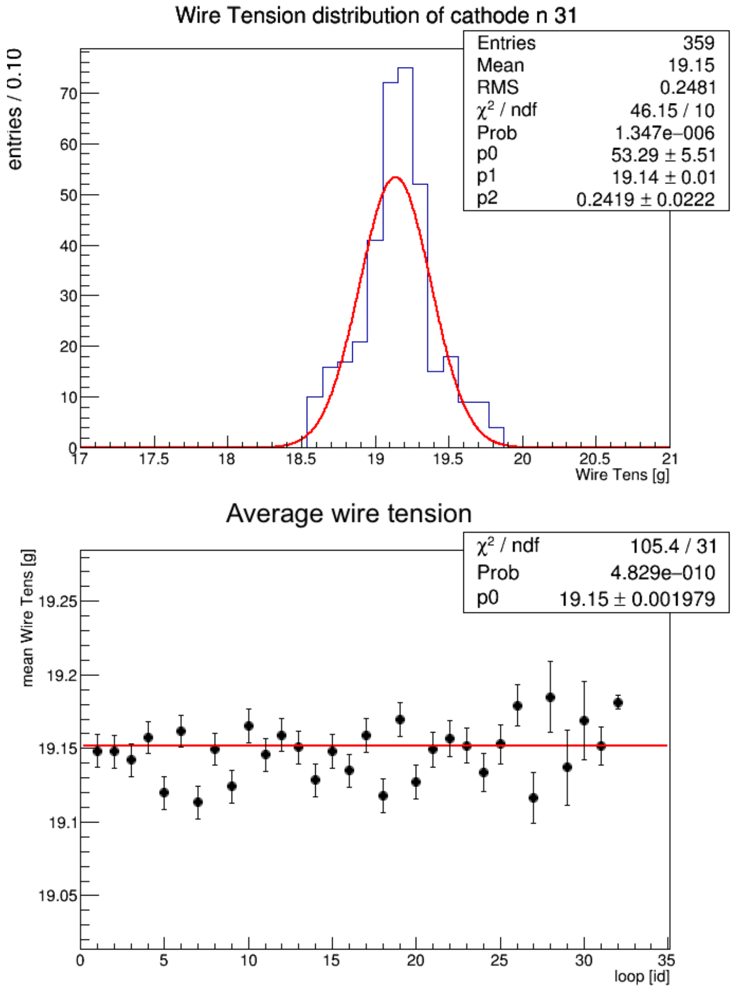

Figure 6.7: Top: The distribution of the wire tension during the wiring. Bottom: Average wire tension for each loops.

The UP wire PCB then is lifted off from the rotating cylinder with a linear actuator connected to the set of vacuum operated suction cups (see Figure 5.24) and placed on the fixed support of the trasport frame (see Figure 6.12) . The unrolling is accomplished by synchronizing the cylinder rotation with the linear displacement of the frame. Once the multi-wire plane is completely unrolled (see Figure 6.13), the second wire PCB is lifted off from the cylinder (see Figure 6.14), as the first one, and placed on the sliding support of the transport frame.

The frame is then removed from the extraction system, the multi-wire plane is inspected and stored inside the clean room (see Figure 6.14). 39 such frames (24 cathodes plus 2 spares and 12 anodes plus 1 spare) are then shipped to the assembly station at INFN Pisa. During the transport, the 3 sets of 13 frames are wrapped in a welded seal bag (Figure 6.15) to avoid contamination from outside and equipped

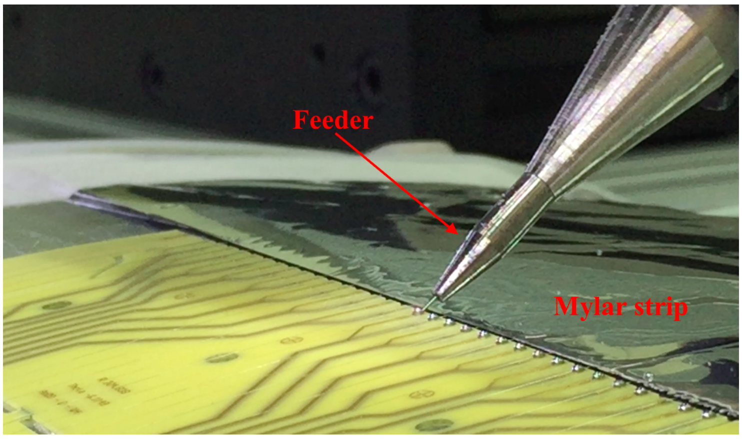

Figure 6.8: Soldering phase.

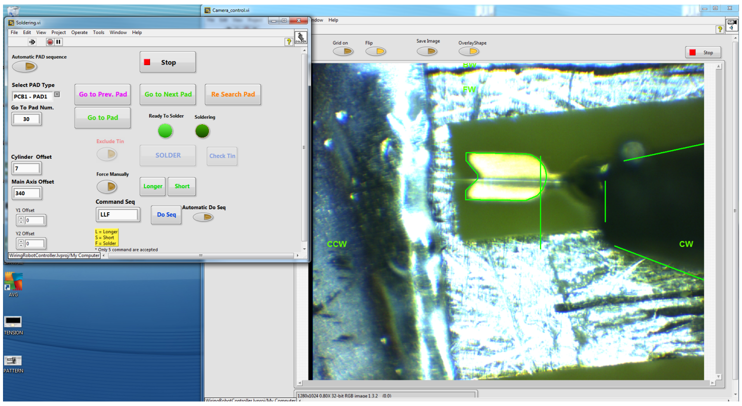

Select PAD Type: PCB1 - PAD1
Go To Pad Num.: 30
Cylinder Offset: 7
Main Axis Offset: 340
Y1 Offset: 0
Y2 Offset: 0
Command Seq: LLF

L = Longer
S = Short
F = Solder
* Only 5 command are accepted

WiringRobotController.lvproj/My Computer

Figure 6.9: Left: Control screen for the soldering phase with the display of the digital camera.

with valves in order to be flushed with dry gas and with relative humidity sensor to continuously monitor the RH during storage and transport.

6.2 Quality checks on the multi-wire plane

A check on the quality of the multi-wires planes is performed soon after production according to the following steps:

- Visual inspection to remove unwanted dirt contaminating the wires and to identify possible kinks on the wires. in which case the entire plane will be rejected;

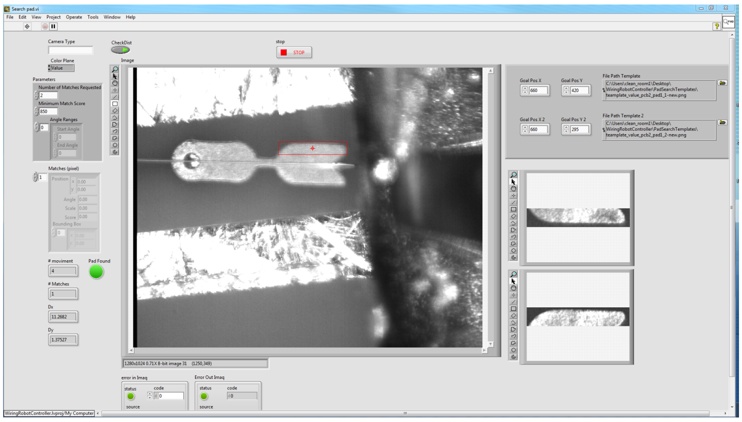

Camera Type:
Color Plane: Value
Parameters
Number of Matches Requested: 2
Minimum Match Score: 850
Angle Ranges: 0
Start Angle: 0
End Angle: 0
Matches (pixel): 1
Position x: 0.00
Position y: 0.00
Angle: 0.00
Scale: 0.00
Score: 0.00
Bounding Box: 0
x: 0.00
y: 0.00
moviment: 4
Matches: 1
Dx: 11.2682
Dy: 1.37527
Goal Pos X: 660
Goal Pos Y: 420
File Path Template: C:\Users\clean_room1\Desktop\WiringRobotController\PadSearchTemplates\teamplate_value_pcb2_pad1_1-new.png
Goal Pos X 2: 660
Goal Pos Y 2: 295
File Path Template 2: C:\Users\clean_room1\Desktop\WiringRobotController\PadSearchTemplates\teamplate_value_pcb2_pad1_2-new.png
1280x1024 0.71X 8-bit image 31 (1250,349)
error in Imaq: status, code 0, source
Error Out Imaq: status, code 0, source

Figure 6.10: Pattern matching.

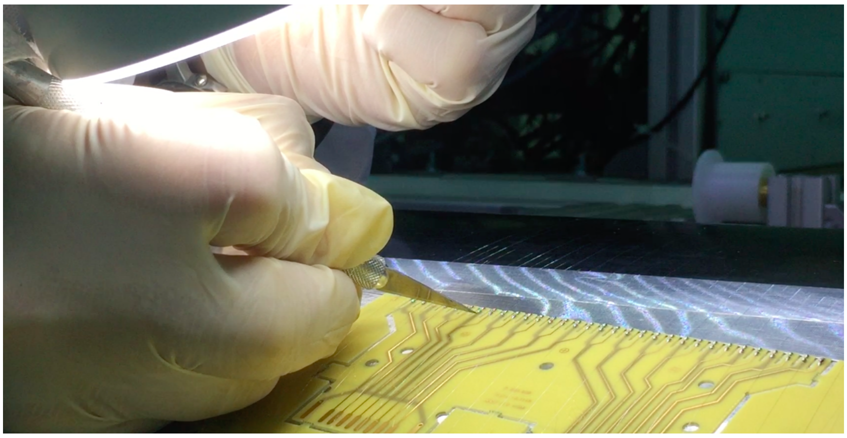

Figure 6.11: Cutting phase.

Figure 6.12: Wire PCB UP placed on the fixed structure.

- Stress test by performing 10 cycles of elongation up to 1 mm above the nominal length of the wire tensioned under a linear optical encoder to induce breakage of damaged wires, in wich case the entire plane will be rejected;

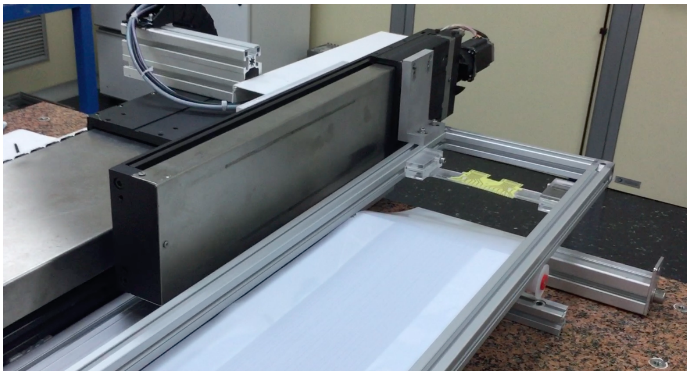

Figure 6.13: Multi wire plane unrolled matching.

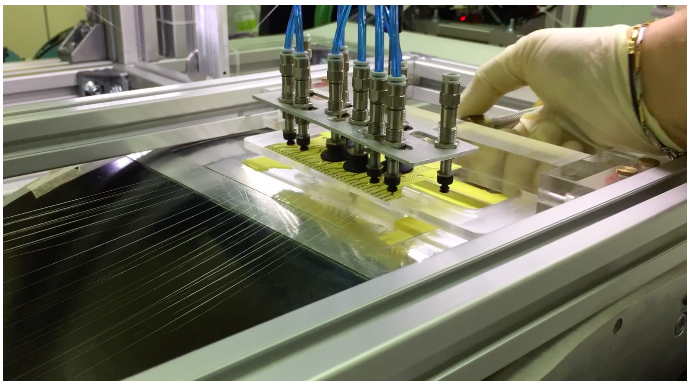

Figure 6.14: DS wire PCB is lifted off from the cylinder.

Figure 6.15: The frames are wrapped in a welded seal bag.

- Wire mechanical tension measurement according to the description in next paragraph. The correct electrostatic stability of the cell under high voltage (see Section 4.2.3) must be ensured with wires at the nominal length.

Table 6.1: Resonance frequencies for the three types of wires. The linear density values take into account the different alloy composition and their coating.

Wire	μ (10^{-6}g/m)	T (g)	f (Hz)
50 μm Al (Ag)	6.53	29.64	54.74
40 μm Al (Ag)	4.38	19.25	53.83
20 μm W (Au)	6.04	24.51	51.74

6.2.1 Measurement of the wire mechanical tension

The measurement of the wire mechanical tension is performed with the method of the resonant oscillation induced on the wires. The first nominal resonant frequency of a wire is given by:

$$f = \frac{1}{2L}\sqrt{\frac{T}{\mu}} \tag{6.1}$$

$$\mu = \pi r^2 \rho \tag{6.2}$$

where L is the length, T is the tension, μ is the linear density, ρ is the volume density and r is the radius of the wire.

The resonance frequencies for the three different wires , at the indicated tensions, are reported in Table 6.1. A system has been developed (Figure 6.16) to measure the variation of the capacitance C_{ww} between two adjacent wires:

$$C_{ww} = \frac{2\pi\varepsilon}{\ln\left(\frac{4H}{d}\right)} \tag{6.3}$$

$$|\delta f| \approx \frac{C_{ww}}{4\pi C\sqrt{LC}}\frac{\frac{2}{3}}{\ln\left(\frac{2H}{d}\right)}\frac{dH}{H} \tag{6.4}$$

where ε is dielectric constant, H is the distance between the wires, d is wire diameter and L, C are inductance and capacitance of the LC resonant circuit and δf is the frequency variation.

A sinusoidal HV signal applied between the two wires induces oscillations causing a variation of the mutual capacitance, the measurement of which, as a function of the frequency of the induced HV signal shows the characteristic resonance shape.

In Figure 6.17 is shown the resonant oscillation frequency for a fixed length of the multi-wire plane (Top) and the wire length vs $(f[Hz])^2$ curves measured for the two external wires of a cathode multi-wire PCB (Bottom). The two curves do not overlap because of a small angle between two wire PCBs on the transport frame. Figure 6.18

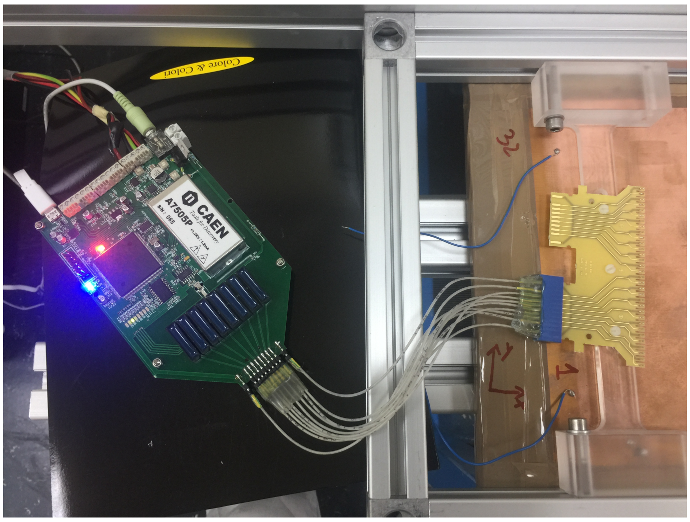

Figure 6.16: The wire tension measuring system.

shows the wire length as a function of the wire mechanical tension, the red dashed line indicates the operating point of the 40 μm Al field wires: L=1925,774 mm at a tension T=19,2 g.

6.3 Assembly procedure

The CDCH is finally assembled at INFN Pisa. The wire PCBs of the multi-wire planes must be kept parallel in order to avoid stresses to the wires at the soldering points. For this reason the assembly procedure is performed with a DEA Ghibli coordinate measuring machine in a clean room. The machine allows a position accuracy of about 20 μm in the horizontal plane and 40 μm on the vertical axis of the fiducial crosses on the wire PCBs.

After passing a mechanical stess test (a repeted cycle of elongation up to 25% over the nominal tension), and a check of the wire tension in which the wire oscillations are induced by an acoustic burst with loud speakers on a multi-wire plane at high voltage), the multi-wire frame can be mounted on the chamber end-plates.

During the assembly phase, the end-plates (Figure 6.19) are moved in at a shorter distance than the nominal one to avoid stressing the wires in the procedure.

The mounting procedure is performed with an adjustable arm consisting of two blocks (Figure 6.20: Top), the distance of which can be adjusted to fit the length of the layer. The wire PCBs, fixed to the transport frame, are anchored to the

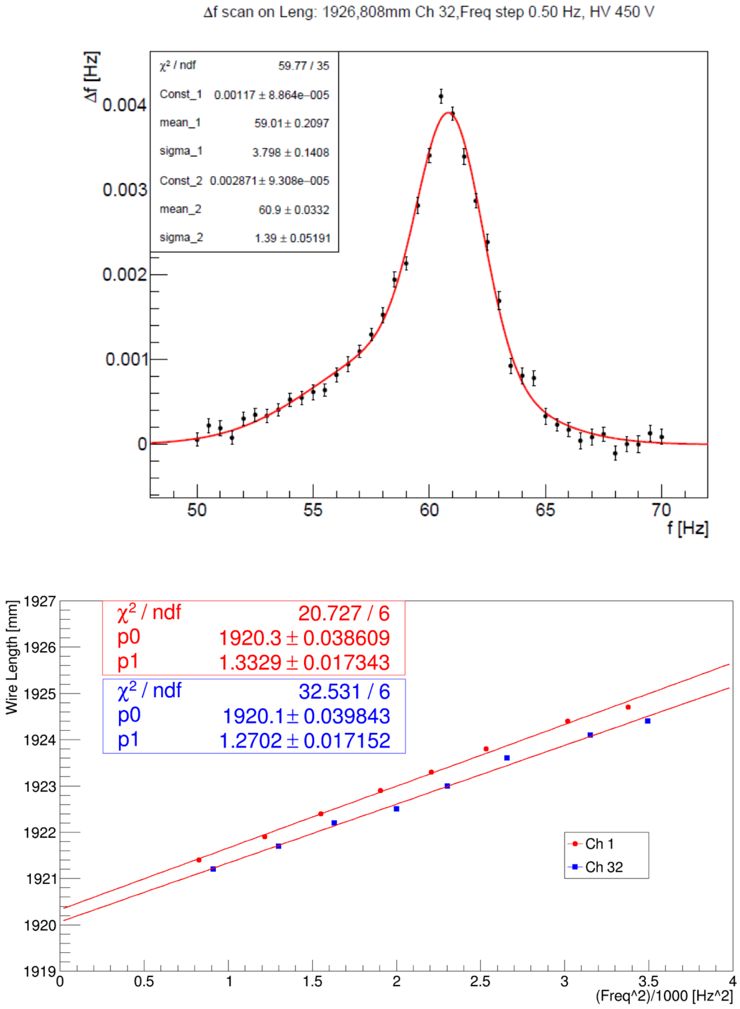

Figure 6.17: Top: Frequency scan for a given wire length. Bottom: Wire length as a function of the $(f[Hz])^2$ for theexternal wire of a cathode multi-wire plane.

adjustable arm with a clip and then released from the frame. The adjustable arm (with the attached multi-wire plane) is then placed next to the end plates for the engagement procedure and it is fixed to a support structure to prevent damaging the wires (Figure 6.20: Above). The adjustable arm transfers the multi-wire layer on the end plates between two spokes. The final positioning is driven by hand through dedicated nippers. The wire PCBs are glued on the PEEK spacer with double-sided tape previously applied on the inner layer. The PEEK spacers are needed to separate the layers at the right distance (Figure 5.4). This procedure is repeated for each of the 12 sectors and for the 10 layers (Figure 6.21 and Figure 6.22).

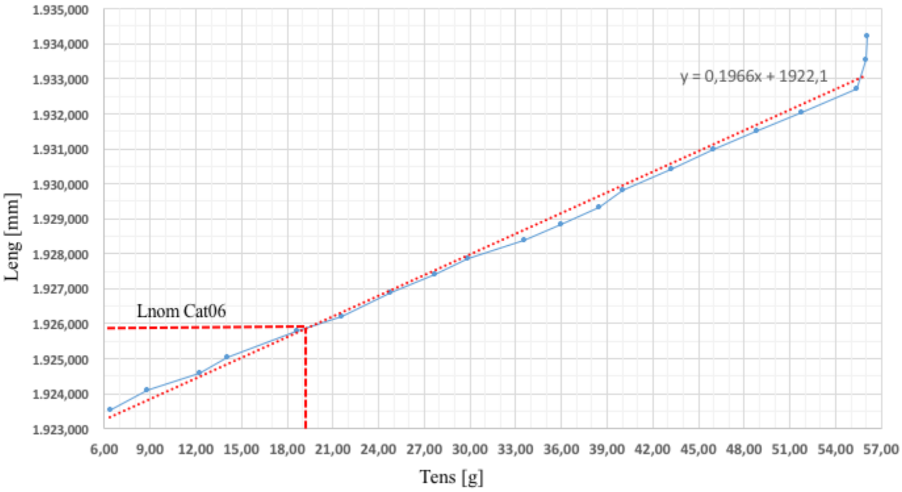

Figure 6.18: Wire length vs Tension. The red dashed line indicates the operating point of the 40 μm Al field wires

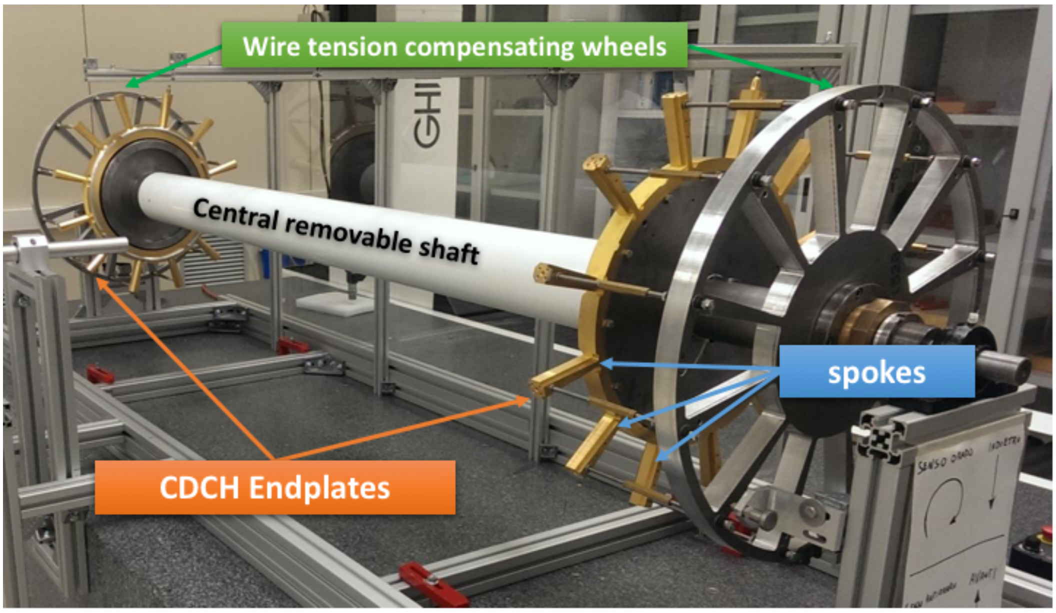

Figure 6.19: CDCH assembly station.

6.4 Conclusion

After mounting the outermost layer, the end-plates are moved to the nominal distance and the CDCH is closed with the outer structural carbon fiber cylinder. Then the end-plates are sealed to prevent gas leakage and the support structures (pcb holders, FE PCBs and extension) are mounted prior to transport to PSI.

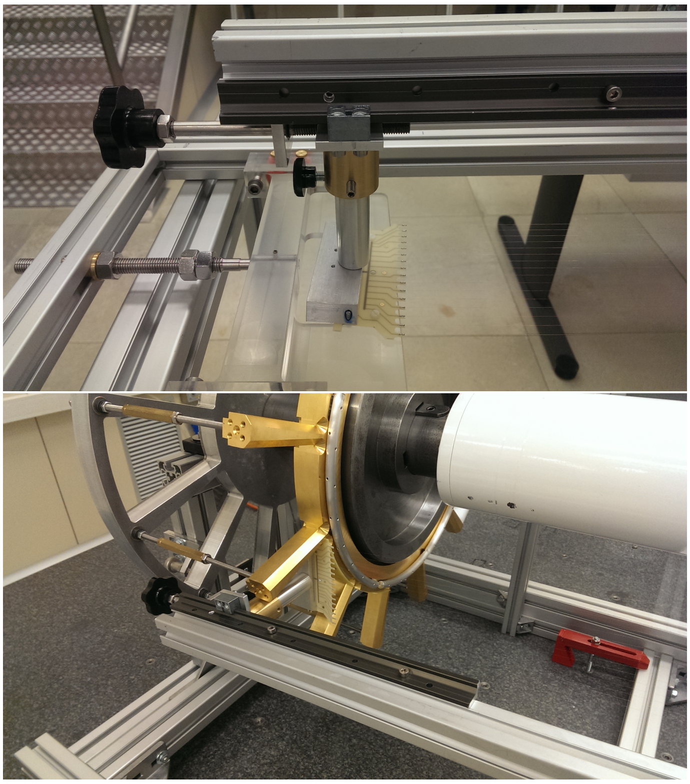

Figure 6.20: Top:A block of the adjustable arm with wire PCB. Bottom: Engagement procedure

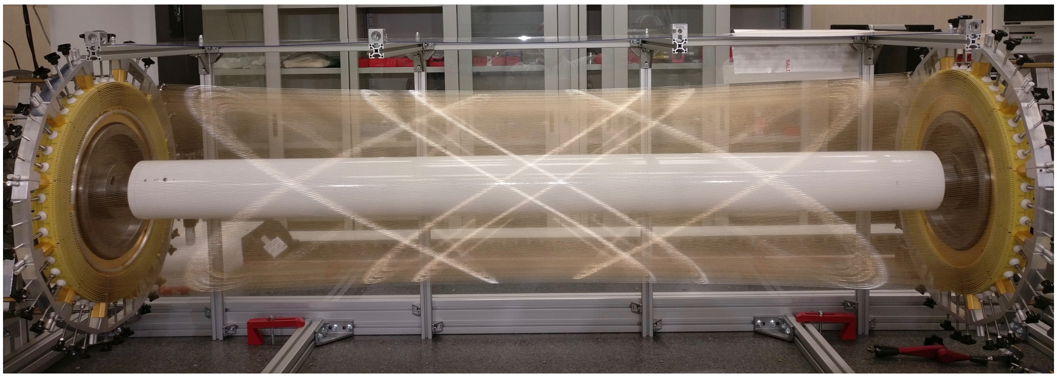

Figure 6.21: CDCH with about 80% of the layers assembled.The hyperbolic shape is visible.

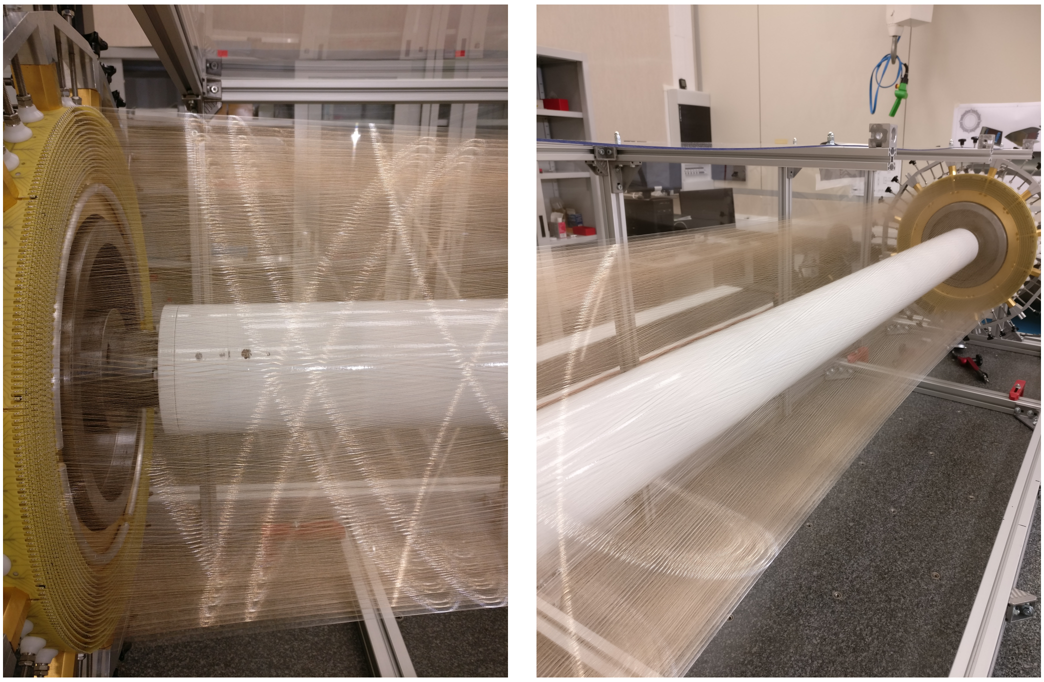

Figure 6.22: Detail of CDCHs with about 80% of the assembled layers

7

Conclusion

The cLFV experiments are considered an excellent probe for the physics beyond the standard model, one of these experiments is MEG, searching for $\mu^+ \to e^+\gamma$ with unprecedentedly high sensitivity. The MEG experiment has established an upper limit $\mathcal{B}.\mathcal{R}.(\mu^+ \to e^+\gamma)$<4.2×$10^{-13}$@90%C.L. [74] with the data collected from year 2009 to year 2013.

In 2013, an upgrade (MEG II), was approved for improving the sensitivity by one order of magnitude, and it is presently under construction. MEG II consists in improving the detectors in order to have better performances. In particular, the MEG II CDCH has been designed to improve the resolutions on the final state positron kinematic variables and to minimize the background sources. The CDCH is a unique volume drift chamber and it is under construction at INFN Lecce and Pisa.

In this thesis, the CDCH has been described, illustrating its the geometry and all the choices made on the materials used for its construction. Subsequently, the new construction technique, in replacement of the classical feed-through technique has been described. To this purpose, a robot has been developed to meet all the constraints imposed by the geometry of CDCH. The robot allowing the construction multi-wires planes and its main functions have been described. Finally, the quality tests carried out on multi-wire planes and their assembly on the final structure have been outlined.

The CDCH construction is currently going on. The end of the wiring phase is planned for July 2017, and the end of the assembly and test phase is scheduled for November 2017. The CDCH will be installed at PSI at the beginning of 2018 and after a first engineering run, it will start data taking in the second half of 2018.

Part IV

Appendices

8

Appendix A: SEM analysis

During the first assembly of CDCH, some aluminum wires were broken after they being mounted on the end-plates. The breakages are due to environmental conditions not favorable inside the clean room in the San Piero a Grado at Pisa (humidity higher than 70% and temperature below 18°C).

To understand the causes of breakage, optical inspection and Scanning Electron Microscope (SEM) analysis were performed. Some wires were exposed voluntarily to H_2O and H_2O with NaCl to accelerate the breaking. The analysis carried out are reported in the following sections.

8.1 SEM analysis on the wires not handled

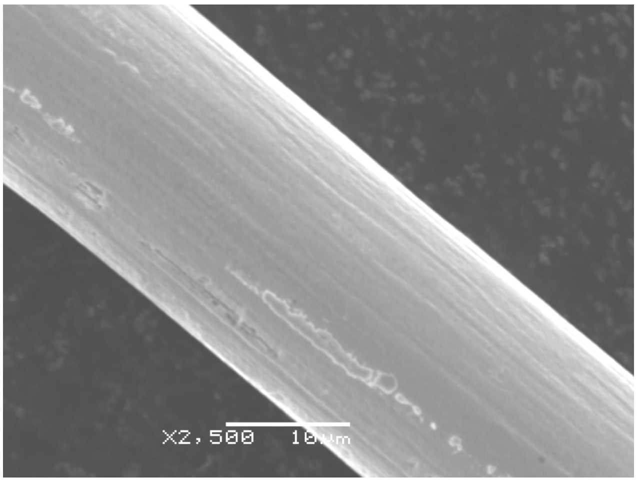

Figure 8.1: Tungsten Wire

The tungsten (Figure 8.1) and aluminum (Figure 8.3) wires are composed of the elements indicated in the datasheet of the production factory (Figure 8.2, Figure 8.4). In the aluminum wire (Figure 8.3) some cracks are visible. These cracks have also been noted during the construction of other drift chambers.

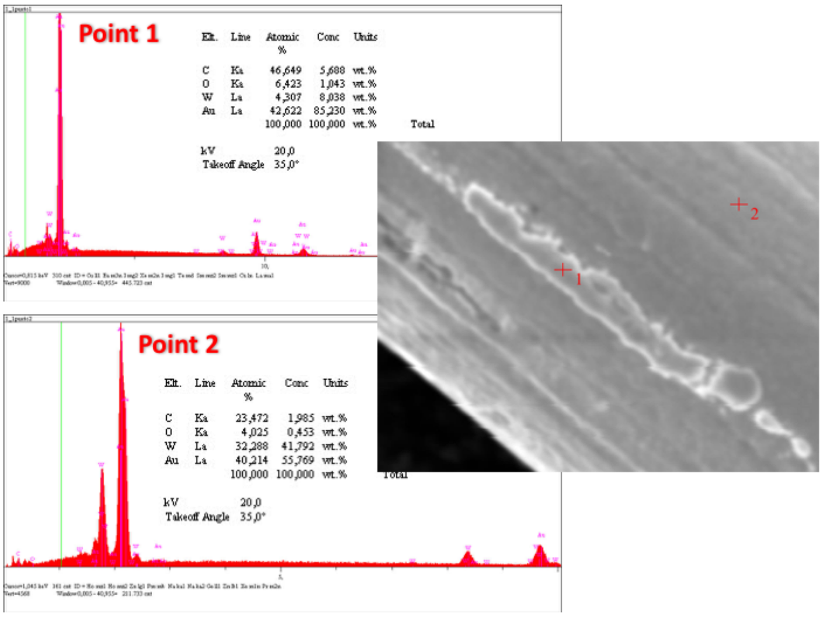

Point 1

Elt.	Line	Atomic %	Conc	Units	
C	Ka	46,649	5,688	wt.%	
O	Ka	6,423	1,043	wt.%	
W	La	4,307	8,038	wt.%	
Au	La	42,622	85,230	wt.%	
		100,000	100,000	wt.%	Total

kV 20,0
Takeoff Angle 35,0°

Point 2

Elt.	Line	Atomic %	Conc	Units	
C	Ka	23,472	1,985	wt.%	
O	Ka	4,025	0,453	wt.%	
W	La	32,288	41,792	wt.%	
Au	La	40,214	55,769	wt.%	
		100,000	100,000	wt.%	Total

kV 20,0
Takeoff Angle 35,0°

Figure 8.2: EDX analysis of tungsten wire

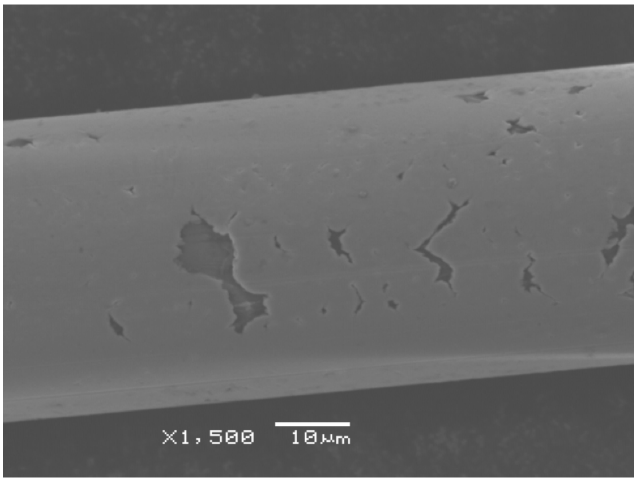

Figure 8.3: Aluminum Wire

8.2 SEM analysis on the wires immersed in H_2O

The aluminim wire (Figure 8.5) immersed in water is extremely fragile; chemical analysis (Figure 8.6) shows the presence of oxygen and aluminum near the break and inside the crack, suggesting the formation of aluminum oxide or hydroxide.

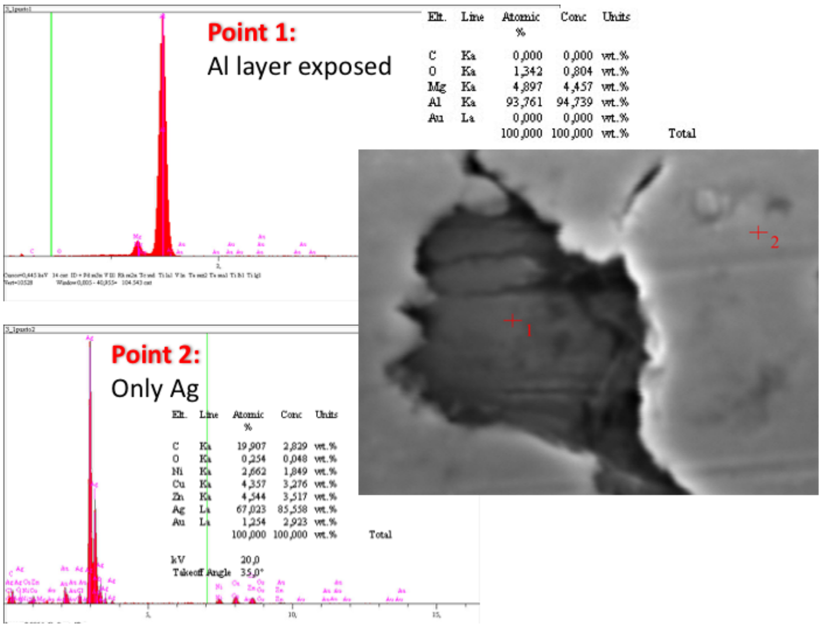

```
Elt.  Line  Atomic   Conc     Units
            %

C     Ka      0,000    0,000  wt.%
O     Ka      1,342    0,804  wt.%
Mg    Ka      4,897    4,457  wt.%
Al    Ka     93,761   94,739  wt.%
Au    La      0,000    0,000  wt.%
            100,000  100,000  wt.%        Total
```

```
Elt.  Line  Atomic   Conc     Units
            %

C     Ka     19,907    2,829  wt.%
O     Ka      0,254    0,048  wt.%
Ni    Ka      2,662    1,849  wt.%
Cu    Ka      4,357    3,276  wt.%
Zn    Ka      4,544    3,517  wt.%
Ag    La     67,023   85,558  wt.%
Au    La      1,254    2,923  wt.%
            100,000  100,000  wt.%        Total

kV           20,0
Takeoff Angle 35,0°
```

Figure 8.4: EDX analysis of aluminum wire

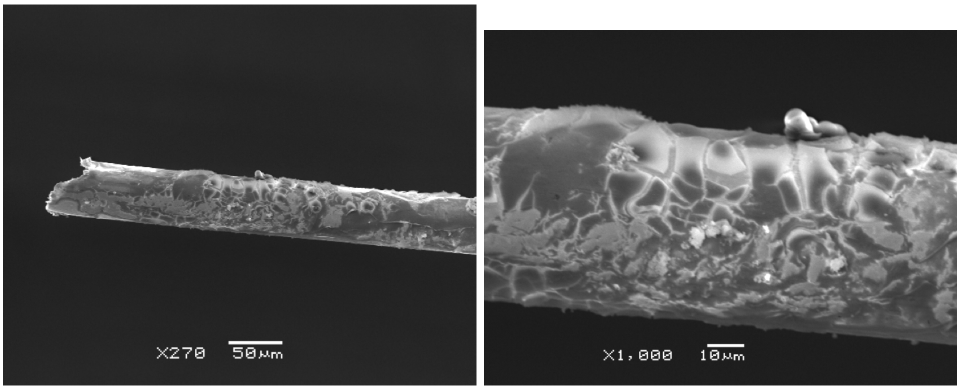

Figure 8.5: Aluminum Wire immersed in H_2O

8.3 SEM analysis on the wires immersed in H_2O with NaCl

The aluminim wire (Figure 8.5) immersed in water and NaCl is extremely fragile, chemical analysis (Figure 8.6) shows the presence of oxygen, aluminum, sodium and chloride. At the center of the wire, away from the rupture, as expected, there is a high concentration of silver. Even in this case it is assumed that the aluminum oxide or hydroxide formation weakens the wire.

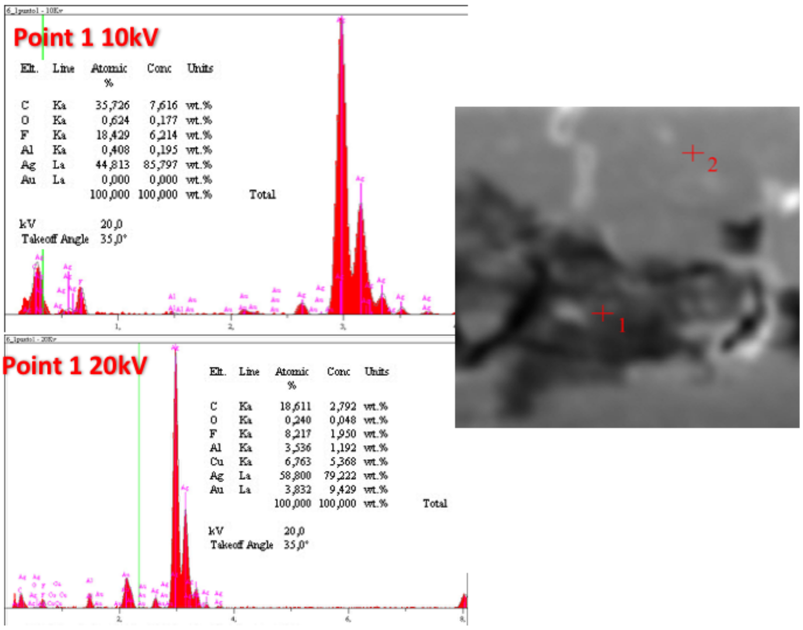

```
Elt.  Line  Atomic     Conc   Units
              %

C     Ka    35,726    7,616   wt.%
O     Ka     0,624    0,177   wt.%
F     Ka    18,429    6,214   wt.%
Al    Ka     0,408    0,195   wt.%
Ag    La    44,813   85,797   wt.%
Au    La     0,000    0,000   wt.%
           100,000  100,000   wt.%        Total

kV                20,0
Takeoff Angle     35,0°
```

```
Elt.  Line  Atomic     Conc   Units
              %

C     Ka    18,611    2,792   wt.%
O     Ka     0,240    0,048   wt.%
F     Ka     8,217    1,950   wt.%
Al    Ka     3,536    1,192   wt.%
Cu    Ka     6,763    5,368   wt.%
Ag    La    58,800   79,222   wt.%
Au    La     3,832    9,429   wt.%
           100,000  100,000   wt.%        Total

kV                20,0
Takeoff Angle     35,0°
```

Figure 8.6: EDX analysis of aluminum wire immersed in H_2O

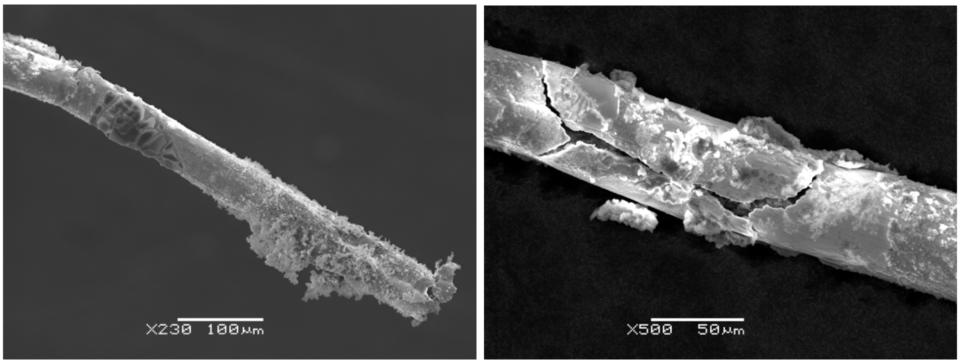

Figure 8.7: Aluminum Wire immersed in H_2O and NaCl

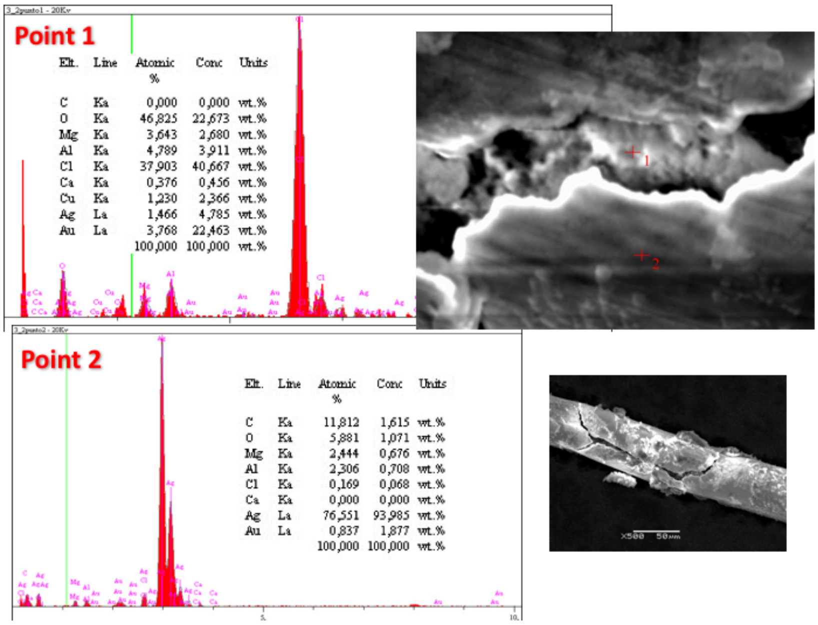

Elt.	Line	Atomic %	Conc	Units
C	Ka	0,000	0,000	wt.%
O	Ka	46,825	22,673	wt.%
Mg	Ka	3,643	2,680	wt.%
Al	Ka	4,789	3,911	wt.%
Cl	Ka	37,903	40,667	wt.%
Ca	Ka	0,376	0,456	wt.%
Cu	Ka	1,230	2,366	wt.%
Ag	La	1,466	4,785	wt.%
Au	La	3,768	22,463	wt.%
		100,000	100,000	wt.%

Elt.	Line	Atomic %	Conc	Units
C	Ka	11,812	1,615	wt.%
O	Ka	5,881	1,071	wt.%
Mg	Ka	2,444	0,676	wt.%
Al	Ka	2,306	0,708	wt.%
Cl	Ka	0,169	0,068	wt.%
Ca	Ka	0,000	0,000	wt.%
Ag	La	76,551	93,985	wt.%
Au	La	0,837	1,877	wt.%
		100,000	100,000	wt.%

Figure 8.8: EDX analysis of aluminum wire immersed in H_2O and NaCl

Acknowledgments

I guess this was a great experience, I could learn a lot about the world of the research. First of all many thanks to my supervisors Dr. Marco Panareo and Dr. Franco Grancagnolo for their support and advises for the realization of this work. Many thanks to Dr. Giovanni Francesco Tassielli for help and advice on building the robot wiring. Many thanks to Dr. Cladio Chiri for all the advises. Many thanks to the technicians of the CAD laboratory (Alessandro Miccoli, Angelo Innocente, Pino Fiore, Matteo Spedicato and Paola Mazzotta) for their fundamental work for the construction of robot wiring and their support in all activities. Many thanks to the technicians Alessandro Corvaglia and Carlo Pinto for helping build DAQ and bureaucracy for different purchases. Many many thanks to all the MEG collaborators who supported us giving useful advises. Many thanks to my family who have never stopped to support me. Finally many thanks to my colleagues who shared this experience with me, Aurora, Maria Paola, Giuseppe, Patrizio and Andrea. Many thanks to all those (which I forgot to mention) that I was close to this beautiful experience.

Bibliography

[1] St. Ritt et al. A. Schoning. “Research Proposal for an Experiment to Search for the Decay $\mu^+ \rightarrow e^+e^-e^+$”. In: *Research Proposal to Paul Scherrer Institut* R-12-03.1 (2013) (cit. on pp. 21, 24).

[2] Georges et al. (ATLAS Collaboration) Aad. “Observation of a new particle in the search for the Standard Model Higgs boson with the ATLAS detector at the LHC”. In: *Phys.Lett. B* 716 (2012), pp. 1–29. DOI: `hep-ex/1207.7214` (cit. on p. 13).

[3] A. Baldini et al. “A new cylindrical drift chamber for the MEG II experiment”. In: *Nucl. Instrum. Meth. A* 824 (2016), pp. 589–591. DOI: `10.1016/j.nima.2015.10.103` (cit. on p. 83).

[4] A. Baldini et al. “An FPGA-based trigger for the phase II of the MEG experiment”. In: *Nucl. Instrum. Meth. A* 824 (2016), pp. 326–328. DOI: `10.1016/j.nima.2015.11.085` (cit. on p. 65).

[5] A. E. Pifer et al. “A high stopping density μ^+ beam”. In: *Nucl. Instrum. and Meth.* 135 (1976), pp. 39–46. DOI: `10.1016/0029-554X(76)90823-5` (cit. on p. 36).

[6] A. Hitachi et al. “Effect of ionization density on the time dependence of luminescence from liquid argon and xenon”. In: *Phys. Rev. B* 27.9 (1983), pp. 5279 –5285. DOI: `10.1103/PhysRevB.27.5279` (cit. on p. 40).

[7] D. F. Anderson et al. “A simple vernier method for improving the accuracy of coordinate read-out in large wire chamber.” In: *Nucl. Instrum. Meth. A* 224 (1984), pp. 315 –317. DOI: `10.1016/0167-5087(84)90482-4` (cit. on p. 47).

[8] D. Green et al. “Accurate 2 dimensional drift tube readout using time division and vernier pads.” In: *Nucl. Instrum. Meth. A* 256.2 (1987), pp. 305 –312. DOI: `10.1016/0168-9002(87)90223-3` (cit. on p. 47).

[9] D. R. Bolton et al. “Search for rare muon decays with the Crystal Box detector”. In: *Phys. Rev. D* 38 (1985), pp. 2077–2101. DOI: `10.1103/PhysRevD.38.2077` (cit. on p. 17).

[10] G. Chiarello et al. “A high performance Front End Electronics for drift chamber readout in MEG experiment upgrade”. In: *Nucl. Instrum. Meth. A* 824 (2016), pp. 589–591. DOI: `10.1016/j.nima.2015.10.103` (cit. on p. 86).

[11] G. Chiarello et al. “A high performance front end for MEG II tracker”. In: *Advances in Sensors and Interfaces (IWASI), 2015 6th IEEE International Workshop on*. IEEE. 2015, pp. 55–57 (cit. on p. 86).

[12] H-W. Reist et al. “Development of a low momentum surface muon beam for LAMPF”. In: *Nucl. Instrum. and Meth. A* 153 (1978), pp. 61–64. DOI: `10.1016/0029-554X(78)90618-3` (cit. on p. 36).

[13] J. Allison et al. “The diamond shaped cathode pads of the OPAL muon barrel drift chambers.” In: *Nucl. Instrum. Meth. A* 310.2 (1991), pp. 527 –534. DOI: `10.1016/0168-9002(91)91094-C` (cit. on p. 47).

[14] K. Bora et al. “Charged lepton flavor violation $\mu \to e\gamma$ in μ-τ symmetric SUSY SO (10) mSUGRA, NUHM, NUGM, and NUSM theories and LHC”. In: *Eur. Phy. Jou. C* 75.9 (2015), pp. 1–14. DOI: `10.1140/epjc/s10052-015-3617-0` (cit. on p. 18).

[15] K. Hayasaka et al. “Search for lepton- flavor-violating τ decays into three leptons with 719 million produced $tau^+\tau^-$ pairs”. In: *Phys. Lett. B* 687 (2010), pp. 139–143. DOI: `10.1016/j.physletb.2010.03.037` (cit. on p. 26).

[16] M. Adinolfi et al. “The tracking detector of the KLOE experiment”. In: *Nucl. Instrum. Meth. A* 488.1 (2002), pp. 51–73. DOI: `10.1016/S0168-9002(02)00514-4` (cit. on p. 72).

[17] M. Ahmed et al. “Search for the lepton family number nonconserving decay $\mu^+ \to e^+\gamma$”. In: *Phys. Rev. D* 65.112002 (2002). DOI: `10.1103/PhysRevD.65.112002` (cit. on p. 23).

[18] M. De Gerone et al. “A high resolution Timing Counter for the MEG II experiment”. In: *Nucl. Instrum. Meth. A* 824 (2016), p. 92. DOI: `10.1016/j.nima.2015.11.022` (cit. on p. 62).

[19] M.D Mestayer et al. “The CLAS drift chamber system”. In: *Nucl. Instrum. Meth. A* 449 (2000), pp. 81–11. DOI: `10.1016/S0168-9002(00)00151-0` (cit. on p. 75).

[20] M.De Gerone et al. “Development and commissioning of the timing counter for the MEG experiment.” In: *IEEE Transactions on Nuclear Science* 59 (2012), pp. 379 –388. DOI: `10.1109/TNS.2012.2187311` (cit. on p. 44).

[21] R. Assiro et al. “Ultra-low mass drift chambers”. In: *Nucl. Instrum. Meth. A* 718 (2013), pp. 443–445. DOI: `10.1016/j.nima.2012.10.047` (cit. on p. 90).

[22] R. R. Crittenden et al. “Radiative Decay Modes of the Muon”. In: *Phys. Rev.* 121 (1961), pp. 1823–1832. DOI: `10.1103/PhysRev.121.1823` (cit. on p. 17).

[23] S. Freedman et al. “Limits on neutrino oscillations from ν e appearance”. In: *Phys. Rev. D* 47 (1993), pp. 811–829. DOI: `10.1016/0920-5632(94)00752-H` (cit. on p. 17).

[24] S. Uno et al. “Study of a drift chamber filled with a helium-ethane mixture.” In: *Nucl. Instrum. Meth. A* 623 (1993), pp. 111 –113. DOI: `10.1016/0168-9002(93)91304-6` (cit. on p. 46).

[25] S. Weinberg et al. “Conceptual foundations of the unified theory of weak and electromagnetic interactions”. In: *Rev. Mod. Phys.* 515 (1980), p. 52. DOI: `10.1103/RevModPhys.52.515` (cit. on p. 12).

[26] U. Bellgardt et al. “A search for $\mu^- - e^-$ conversion in muonic gold”. In: *Eur. Phys. J. C* 47 (2006), pp. 337–346. DOI: `10.1140/epjc/s2006-02582-x` (cit. on pp. 21, 25).

[27] U. Bellgardt et al. “Search for the decay $\mu^+ \to e^+e^-e^+$”. In: *Nucl. Phys. B* 299 (1988), pp. 1–6. DOI: `10.1016/0550-3213(88)90462-2` (cit. on p. 17).

[28] U. Bellgardt et al. "Search for the decay $\mu^+ \to e^+e^-e^+$". In: *Nucl.Phys.Proc.Suppl.B* 299 (1988), pp. 1–6. DOI: `10.1016/0550-3213(88)90462-2` (cit. on pp. 21, 24).

[29] W. Bertl et al. "Search for the decay $\mu^+ \to e^+e^-e^+$". In: *Nucl. Phys. B* 260 (1985), pp. 1–31. DOI: `10.1016/0550-3213(85)90308-6` (cit. on p. 17).

[30] W. Ootani et al. "Development of a Thin-wall Superconducting Magnet for the Positron Spectrometer in the MEG Experiment". In: *IEEE Trans. on Applied Super-conductivity* 14 (2004), pp. 568 –571. DOI: `10.1109/TASC.2004.829721` (cit. on p. 42).

[31] W. Ootani et al. "Development of deep-UV sensitive MPPC for liquid xenon scintillation detector". In: *Nucl. Instrum. Meth. A* 787 (2015), p. 220. DOI: `10.1016/j.nima.2014.12.007` (cit. on p. 61).

[32] W. Wagner et al. "PSI status 2008 - Developments at the 590 MeV proton accelerator facility". In: *Nucl. Instr. Meth. A* 600 (2009), pp. 5–7. DOI: `10.1016/j.nima.2008.11.018` (cit. on p. 35).

[33] Amphenol. *Amphenol Spectra Strip*. URL: `www.spectra-strip.com` (cit. on p. 88).

[34] B. Aubert et al. (BABAR Collaboration). "Searches for Lepton Flavor Violation in the decays $\tau \to e\gamma$ and $\tau \to \mu\gamma$". In: *Phys. Rev. Lett.* 104.021802 (2010), p. 104. DOI: `10.1103/PhysRevLett.104.021802` (cit. on p. 26).

[35] A Baldini, C Bemporad, F Cei, et al. "Absorption of scintillation light in a 100l liquid xenon γ-ray detector and expected detector performance". In: *Nucl. Instrum. and Meth. A* 545.3 (2005), pp. 753–764. DOI: `10.1016/j.nima.2005.02.029` (cit. on p. 40).

[36] R. H. Bernstein and P.S. Cooper. "Charged lepton flavor violation: An experimenter's guide". In: *Physics Reports* 532 (2013), pp. 27–64. DOI: `10.1016/j.physrep.2013.07.002` (cit. on p. 20).

[37] Serguei et al. (CMS Collaboration) Chatrchyan. "Observation of a new boson at a mass of 125 GeV with the CMS experiment at the LHC". In: *Phys.Lett. B* 716 (2012), pp. 30–61. DOI: `hep-ex/1207.7235` (cit. on p. 13).

[38] M. Chiappini. "The new drift chamber of the MEG-II experiment, in search for lepton flavor violations." MA thesis. University of Pisa, 2016. URL: `https://etd.adm.unipi.it/t/etd-06202016-113900` (cit. on pp. 85, 92).

[39] G. Chiarello. "The full stereo drift chamber for the MEG II experiment". In: *JINST* 12 C03062 (2017). DOI: `10.1088/1748-0221/12/03/C03062` (cit. on p. 83).

[40] COMET Collaboration. "Experimental Proposal for Phase-I of the COMET Experiment at J-PARC". In: *KEK/J-PARC-PAC 2012-10* (2012). URL: `http://j-parc.jp/researcher/Hadron/en/pac1207/pdf/E212012-10.pdf` (cit. on pp. 21, 25).

[41] A. Czarnecki. "Muon decay in orbit: spectrum of high-energy electrons". In: *Phys. Rev. D* 84.013006 (2011). DOI: `10.1103/PhysRevD.84.013006` (cit. on p. 24).

[42] Analog Device. *ADA4927-1 Datasheet and Product Info*. URL: `www.analog.com/en/products/amplifiers/differential-amplifiers/fully-differential-amplifiers/ada4927-1.html` (cit. on p. 86).

[43] A. D'Onofrio. "Improving single hit reconstruction of the MEG II drift chamber by using cluster timing information." Master thesis. University of Pisa, 2014 (cit. on p. 77).

[44]F.Cei and F.Nicolò. “Lepton Flavour Violation Experiments”. In: *Advances in High Energy Physics* (2014), pp. 1–31. DOI: `10.1155/2014/28291` (cit. on pp. 15, 18).

[45]G. J. Feldman and Y. Okada. “Unified Approach to the Classical Statistical Analysis of Small Signals.” In: *Physical Review D* 57 (1998). DOI: `10.1103/PhysRevD.57.3873` (cit. on pp. 31, 56).

[46]H. Fritzsch and P. Minkowski. “Unified interactions of leptons and hadrons”. In: *Annals Phys.* 93 (1975), p. 193. DOI: `10.1016/0003-4916(75)90211-0` (cit. on p. 16).

[47]L. Galli. “A real time glance at the Lepton Flavor Violating decay $\mu \to e\gamma$ in the MEG experiment.” PhD thesis. University of Pisa, 2010. URL: `https://meg.web.psi.ch/docs/theses/GalliThesis.pdf` (cit. on p. 49).

[48]L. Galli. “An FPGA-based trigger for the search of $\mu^+ \to e^+\gamma$ decay in the MEG experiment”. In: *IEEE Nuclear Science Symposium Conference Record* 08 (2008). DOI: `10.1109/NSSMIC.2008.4774897` (cit. on p. 49).

[49]L. Galli. “An FPGA-based trigger for the search of $\mu^+ \to e^+\gamma$ decay in the MEG experiment”. In: *IEEE Nuclear Science Symposium Conference Record* 09 (2009). DOI: `10.1109/NSSMIC.2009.5401801` (cit. on p. 49).

[50]H. Georgi and D. V. Nanopoulos. “Ordinary predictions from grand principles: t-quark mass in O(10)”. In: *Nucl. Phys. B* 155 (1975), p. 52. DOI: `10.1016/0550-3213(79)90355-9` (cit. on p. 16).

[51]A. de Gouvêa and P. Vogel. “Lepton flavor and number conservation, and physics beyond the standard model”. In: *Progress in Particle and Nuclear Physics* 71 (2013), pp. 75–92. DOI: `10.1016/j.ppnp.2013.03.006` (cit. on p. 20).

[52]M. Gupta. “Calculation of radiation length in materials”. In: *PH-EP-Tech-Note-2010-013* (2010). URL: `cds.cern.ch/record/1279627/files/PH-EP-Tech-Note-2010-013.pdf` (cit. on p. 75).

[53]F. Halzen and A. D. Martin. *Quarks and Leptons: An Introductory Course In Modern Particle Physics*. Ed. by Wiley and Sons. 1984 (cit. on pp. 12, 13).

[54]Hamamatsu. *Hamamatsu Photonics PMT*. URL: `http://www.hamamatsu.com` (cit. on pp. 41, 45).

[55]M. Hildebrandt. “The drift chamber system of the MEG experiment.” In: *Nucl. Instrum. Meth. A* 623 (2010), pp. 111 –113. DOI: `10.1016/j.nima.2010.02.165` (cit. on p. 46).

[56]National Instrument. *NI C Series Module Compatibility Chart*. URL: `http://www.ni.com/product-documentation/8136/en/` (cit. on p. 109).

[57]National Instruments. *LabVIEW System Design Software*. URL: `http://www.ni.com/labview/` (cit. on pp. 106, 111).

[58]National Instruments. *Platform CompactRIO*. URL: `http://www.ni.com/compactrio` (cit. on p. 99).

[59]Texas Instruments. *THS4509 High-Speed Op Amps*. URL: `http://www.ti.com/product/THS4509` (cit. on p. 86).

[60] R. Iwai. “Development and commissioning of MEG II Radiative Decay Counter.” Master thesis. University of Tokyo, 2017. URL: `https://meg.web.psi.ch/docs/theses/Iwai_master_final.pdf` (cit. on p. 65).

[61] Julabo. *FL1201 Recirculating Cooler*. URL: `www.julabo.com/en/products/recirculating-coolers/fl1201-recirculating-cooler` (cit. on p. 88).

[62] D. Kaneko. “The final result of $\mu^+ \to e^+\gamma$ search with the MEG experiment.” PhD thesis. University of Tokyo, 2016. URL: `https://meg.web.psi.ch/docs/theses/kaneko_phd_final.pdf` (cit. on p. 48).

[63] Dr. Mergenthaler GmbH & Co. KG. *LASCON Hybrid: Laser*. URL: `http://www.ma-info.de/en/lascon-hybrid.html` (cit. on p. 106).

[64] Y. Kuno and Y. Okada. “Muon decay and physics beyond the standard model”. In: *Rev.Mod.Phys* 72 (2001), pp. 151–202. DOI: `hep-ph/9909265` (cit. on pp. 28–30).

[65] L. Galli et al. M. Francesconi. “A new generation of integrated trigger and read out system for the MEG II experiment”. In: *IEEE Conference Publications MOCAST* (2016), p. 4. DOI: `10.1109/MOCAST.2016.7495118` (cit. on p. 65).

[66] MAGTROL. *Hysteresis Clutches*. URL: `http://www.magtrol.com/brakesandclutches/hysteresis_clutches.html` (cit. on p. 100).

[67] MAGTROL. *MAGTROL Torque traducer TM Series*. URL: `http://www.magtrol.com/torque/torquemeter_transducers.html` (cit. on p. 99).

[68] MAGTROL. *Power supplies*. URL: `http://www.magtrol.com/brakesandclutches/power_supplies.html` (cit. on p. 101).

[69] V. Martinelli. “Ottimizzazione e realizzazione di una camera per il monitoraggio del gas della camera a deriva dell’esperimento MEG-II”. Master thesis. University of Sapienza Roma, 2015 (cit. on p. 89).

[70] Adam et al. (MEG Collaboration). “A limit for the $\mu \to e\gamma$ decay from the MEG experiment”. In: *Nuclear Physics B* 834.1 (2010), pp. 1–12. DOI: `10.1016/j.nuclphysb.2010.03.030` (cit. on p. 51).

[71] Adam et al. (MEG Collaboration). “New constraint on the existence of the $\mu^+ \to e^+\gamma$ decay”. In: *Physical review letters* 110.20 (2013). DOI: `arXiv:1303.0754[hep-ex]` (cit. on p. 52).

[72] A.M. Baldini et al. (MEG Collaboration). “MEG Upgrade Proposal”. In: *arXiv* (2013), pp. 1–131. URL: `1301.7225v2[physics.ins-det]` (cit. on pp. 57, 58, 60–64, 71).

[73] A.M. Baldini et al. (MEG Collaboration). “Muon polarization in the MEG experiment:predictions and measurements”. In: *The European Physical Journal C* 76.3 (2016), pp. 1–8. DOI: `10.1140/epjc/s10052-016-4047-3` (cit. on pp. 38, 53).

[74] A.M. Baldini et al. (MEG Collaboration). “Search for the Lepton Flavour Violating Decay $\mu^+ \to e^+\gamma$ with the Full Dataset of the MEG Experiment”. In: *The European Physical Journal C* 76.434 (2016), pp. 1–30. DOI: `10.1140/epjc/s10052-016-4271-x` (cit. on pp. 17, 21, 51, 52, 56, 130).

[75] J. Adam et al. MEG collaboration. “The MEG detector for $\mu^+ \to e^+\gamma$ search.” In: *Eur. Phys. J. C* 73.4 (2013), pp. 1–59. DOI: `10.1140/epjc/s10052-013-2365-2` (cit. on pp. 34, 39, 89).

[76] ETH messtechnik. *ETH messtechnik DRFL rotating torque sensor*. URL: `http://www.eth-messtechnik.de/en/01_products/01_torque-sensor/r_drfl.html` (cit. on p. 100).

[77] M.D. Mestayer. “Choosing the correct combination of sense field, and guard wire voltage”. In: *CLAS-Note 92-005* (1992) (cit. on p. 75).

[78] Satoshi Mihara. “MEG liquid xenon detector”. In: *J.Phys.Conf.Ser.* 308 (2011). DOI: `10.1088/1742-6596/308/1/012009` (cit. on p. 41).

[79] T. Mori and W. Ootani. “Flavour Violating Muon Decays, Progress in Particle and Nuclear Physics”. In: *Progress in Particle and Nuclear Physics* 79 (2014), pp. 57–94. DOI: `10.1016/j.ppnp.2014.09.001` (cit. on p. 18).

[80] R.M. Carey et al. (Mu2e Collaboration). “Proposal to search for $\mu N - eN$ with a single event sensitivity below 10^{-16}”. In: *FERMILAB-PROPOSAL-0973* (). DOI: `http://inspirehep.net/record/809087` (cit. on pp. 21, 25).

[81] S. Nakura. “Development of Radiative Decay Counter for ultimate sensitivity of MEG II experiment.” Master thesis. University of Tokyo, 2016. URL: `https://meg.web.psi.ch/docs/theses/nakaura_master.pdf` (cit. on p. 65).

[82] H. Nishiguchi. “An Innovative Positron Spectrometer to Search for the Lepton Flavour Violating Muon Decay with a Sensitivity of 10^{-13}”. PhD thesis. University of Tokyo, 2008. URL: `http://meg.web.psi.ch/docs/theses/nishiguchi_phd.pdf` (cit. on pp. 46, 70).

[83] S. Ogawa. “Liquid xenon calorimeter for MEG II experiment with VUV-sensitive MPPCs”. In: *Nucl. Instrum. Meth. A* (2016). DOI: `10.1016/j.nima.2016.06.085` (cit. on p. 61).

[84] A. Papa. “Search for the lepton flavour violation in $\mu^+ \to e^+\gamma$. The calibration methods for the MEG experiment.” PhD thesis. University of Pisa, 2009. URL: `https://meg.web.psi.ch/docs/theses/Angela.pdf` (cit. on p. 50).

[85] Donald H. Perkins. *Introduction to high energy physics*. Ed. by Cambridge University Press. 2000 (cit. on pp. 12, 13).

[86] M. E. Peskin. “Beyond the Standard Model”. In: *SLAC-PUB* 7479 (1997), pp. 1–95. DOI: `hep-ph/9705479` (cit. on p. 14).

[87] PHIDGETS. *Micro Load Cell (0-100g)-CZL639HD*. URL: `http://www.phidgets.com/products.php?product_id=3139` (cit. on p. 102).

[88] PHIDGETS. *PHIDGETS bridges*. URL: `http://www.phidgets.com/products.php?product_id=1046` (cit. on p. 102).

[89] PI. *Rotation Stages*. URL: `https://www.physikinstrumente.com/en/products/rotation-stages/` (cit. on p. 107).

[90] PIXELINK. *PIXELINK PL-B776 datasheet*. URL: `https://pixelink.com/wp-content/uploads/2015/05/Datasheet_PL-B776.pdf` (cit. on p. 102).

[91] PSI. *The 590 MeV Ring Cyclotron of PSI*. URL: `http://abe.web.psi.ch/accelerators/ringcyc.php` (cit. on p. 36).

[92] M.J. Herrero S. Antusch E. Arganda and A.M. Teixeira. “LFV in tau and muon decays within SUSY seesaw”. In: *Nucl.Phys.Proc.Suppl.B* 169 (2007), pp. 155–165. DOI: `10.1016/j.nuclphysbps.2007.02.102` (cit. on p. 20).

[93] R. Dinapoli S. Ritt and U. Hartmann. “Application of the DRS chip for fast waveform digitizing”. In: *Nucl. Instrm. and Meth. A* 623 (2010), pp. 486 –488. DOI: `10.1016/j.nima.2010.03` (cit. on p. 50).

[94] Ryu Sawada. “Performance of liquid xenon gamma ray detector for MEG”. In: *Nucl. Instrum. and Meth. A* 623.1 (2010), pp. 258–260. DOI: `10.1016/j.nima.2010.02.214` (cit. on p. 40).

[95] A. Sharma. “Study of a drift chamber filled with a helium-ethane mixture.” In: *SLAC-JOURNAL-ICFA-16-3* (1993), pp. 1 –19. DOI: `http://inspirehep.net/record/474076` (cit. on p. 46).

[96] SMC. *Vacuum unit series ZK2*. URL: `http://www.smcworld.com/newproducts/en/zk2/` (cit. on p. 107).

[97] Giovanni Francesco Tassielli. “A gas tracking device based on Cluster Counting for future colliders”. PhD thesis. University of Lecce, 2006 (cit. on pp. 77, 79).

[98] R. Valle. “Development of the Timing Counter”. PhD thesis. Università degli Studi di Genova, 2006. URL: `http://meg.web.psi.ch/docs/theses/valle_phd.pdf` (cit. on p. 44).

[99] M. Venturini. “Ageing and performance studies of drift chamber prototypes for the MEG experiment upgrade”. Master thesis. University of Pisa, 2014 (cit. on p. 70).

[100] W. Riegler W. Blum and L. Rolandi. *PARTICLE DETECTION WITH DRIFT CHAMBERS*. Ed. by SPRINGER VERLAG. 2009 (cit. on p. 79).

[101] T. Mori W.Marciano and J. M. Roney. “Charged lepton flavor violation experiments”. In: *Annual Review of Nuclear and Particle Science* 58.1 (2008), p. 315. DOI: `10.1146/annurev.nucl.58.110707.171126` (cit. on p. 21).

[102] Feng Xiao. “Measurement of the Radiative Muon Decay Branching Fraction in the MEG Experiment”. PhD thesis. University of California Irvine, 2010 (cit. on p. 28).

[103] Zaber. *ZABER T-LA60*. URL: `https://www.zaber.com/products/product_detail.php?detail=T-LA60A&tab=Series%20Features` (cit. on p. 107).